minerals MDPI

*Article*

# Magmatic-Hydrothermal Fluid Processes of the Sn-W Granites in the Maniema Province of the Kibara Belt (KIB), Democratic Republic of Congo

**Douxdoux Kumakele Makutu [1], Jung Hun Seo [2,*], Insung Lee [2], Jihye Oh [3], Pilmo Kang [4], Albert Tienge Ongendangenda [5] and Frederic Mwanza Makoka [5]**

[1] Department of Energy Resources Engineering, Inha University, Incheon 22212, Republic of Korea
[2] School of Earth and Environmental Sciences, Seoul National University, Seoul 08826, Republic of Korea
[3] Korea Institute of Oceanic Science and Technology (KIOST), Busan 49111, Republic of Korea
[4] Korea Polar Research Institute (KOPRI), Incheon 21990, Republic of Korea
[5] Department of Geosciences, Kinshasa University, Kinshasa 012, Democratic Republic of the Congo
* Correspondence: seo28@snu.ac.kr; Tel.: +82-10-4457-4877

**Abstract:** The Kibara belt (KIB) in the Maniema province hosts orebodies bearing cassiterite-wolframite, which are associated with equigranular to pegmatitic late Mesoproterozoic (1094–755 Ma) granites and Sn-W bearing quartz veins that cut through metasedimentary country rocks. Alteration assemblages of muscovite-quartz (±topaz-fluorite-tourmaline) occur in the granites, and muscovite-sericite-quartz occurs in Sn-W quartz veins. Petrographic analyses, including cathodoluminescence (SEM-CL) on cassiterite grains, reveal two types of cassiterite: yellow transparent cassiterite (lighter under SEM-CL: type I) and dark translucent cassiterite (darker under SEM-CL: type II). These types are organized in micro-textures as oscillatory (growth) zones and replacement zones (type II replaces type I). Unlike cassiterite, wolframite is texturally homogenous. LA-ICP-MS results reveal that type II cassiterite is relatively enriched in Fe, Al, Ga, In, As, Pb, Zn, and U, whereas type I is enriched in V, Ti, Zr, Ta, Hf, and Nb. Contrasting Ce anomaly values in the cassiterite types suggest a transition of redox potentials during the Sn precipitation. Fluid inclusion assemblages (FIAs) in quartz, fluorite, and cassiterite are dominantly aqueous, liquid- or vapor-rich, and rarely carbonic-bearing aqueous inclusions. These often texturally coexist in a single "boiling" assemblage in granites. Raman spectroscopy on the bubble part of fluid inclusions in quartz and cassiterite shows various gas species, including $CO_2$, $CH_4$, $N_2$, and $H_2$. Boiling assemblages in the granites suggest that fluid phase separation occurred at about 380–610 bars, which is about 1–2 km (lithostatic) or 3–5 km (hydrostatic) in apparent paleodepth. FIAs in the granites show ranges of salinities of 4–23 wt.% (NaCl equivalent) and homogenization temperatures ($T_h$) of 190–550 °C. FIAs hosted in cassiterite displayed distinctively lower and narrower ranges of salinities of 2–10 wt.% and $T_h$ of 220–340 °C compared to the FIAs hosted in quartz in the granites (salinity of 4–23 wt.%, $T_h$ of 190–550 °C) and the quartz veins (salinity of 1–23 wt.%, $T_h$ of 130–350 °C). This suggests a less salinized and cooler fluid during the cassiterite precipitation. We suggest that magmatic-derived Sn-W bearing fluids be mixed with less saline and cooler aqueous fluids, possibly meteoric water, during the major cassiterite and possibly wolframite depositions in the KIB. This is based on (1) temperature and salinities, (2) hydrothermal alterations, (3) cassiterite micro-textures, and (4) trace element distributions.

**Keywords:** kibara belt; cassiterite; wolframite; ore micro-textures; CL; LA-ICP-MS; trace elements; fluid inclusions

check for updates

**Citation:** Makutu, D.K.; Seo, J.H.; Lee, I.; Oh, J.; Kang, P.; Ongendangenda, A.T.; Makoka, F.M. Magmatic-Hydrothermal Fluid Processes of the Sn-W Granites in the Maniema Province of the Kibara Belt (KIB), Democratic Republic of Congo. *Minerals* **2023**, *13*, 458. https://doi.org/10.3390/min13040458

Academic Editor: Huan Li

Received: 3 March 2023
Revised: 16 March 2023
Accepted: 21 March 2023
Published: 24 March 2023

## 1. Introduction

Granites and related (intra-) perigranitic fluid processes create critical metal deposits such as Sn, Nb, Ta, W, and REE [1–8]. The Kibara belt (KIB) leucogranites originated from crustal partial melting processes called "anatexis" [9–12] during the Kibaran collisional event [12,13]. Sn-W mineralization occurrences are typically associated with differentiated leucogranites [14]. Incipient post-magmatic processes such as fluid exsolution, fluid-rock interactions including alteration [15], metasomatic reactions, and fluid-fluid mixings (magmatic-meteoric) [16] significantly contribute to critical metal mobility and enrichment [4,17]. These syn- and post-granitic fluid processes govern the chemistry of granite (associated pegmatites) and country rocks [14,18]. The evidence of these magmatic-hydrothermal fluid processes can be found in secondary mineral phases through alterations and fluid inclusions [12,19].

Cassiterite and wolframite contain substantial amounts of trace elements, including In, Ga, and REE [20–23]. SEM cathodoluminescence (CL) techniques offer micro-textural information on minerals such as cassiterite [24] and their geochemistry [25]. Nespolo and Souvignier (2015) and Wille (2018) described micro-textural features in cassiterites, including cracks, elbow twinning, and oscillatory zonation, by SEM-CL. This reveals the presence of alternating darker and brighter CL zones. These cassiterite textures can be linked to the incorporation of trace elements such as Ti, Fe, Nb, Ta, and W in the cassiterite [20,25–28].

Research on fluid inclusions provides data on the pressure-temperature-composition of mineralizing fluids using microthermometry [16,29–32], Raman spectroscopy for gas species content [33] and their quantities [34–36], and LA-ICP-MS microanalyses [16,32,37–43]. Sn precipitation processes in granite-related Sn-W deposits have been modeled [15], which shows that multistage and progressive fluid-rock interactions offer efficient control over massive cassiterite precipitation. A fluid inclusion study of the Yankee Lode Sn deposit [16] revealed that cassiterite precipitation was associated with fluids of varying salinities (+trace elements) and temperatures. These findings suggest that the mixing of magmatic and meteoric origin fluids is one of the primary factors controlling the massive precipitation of high-grade Sn.

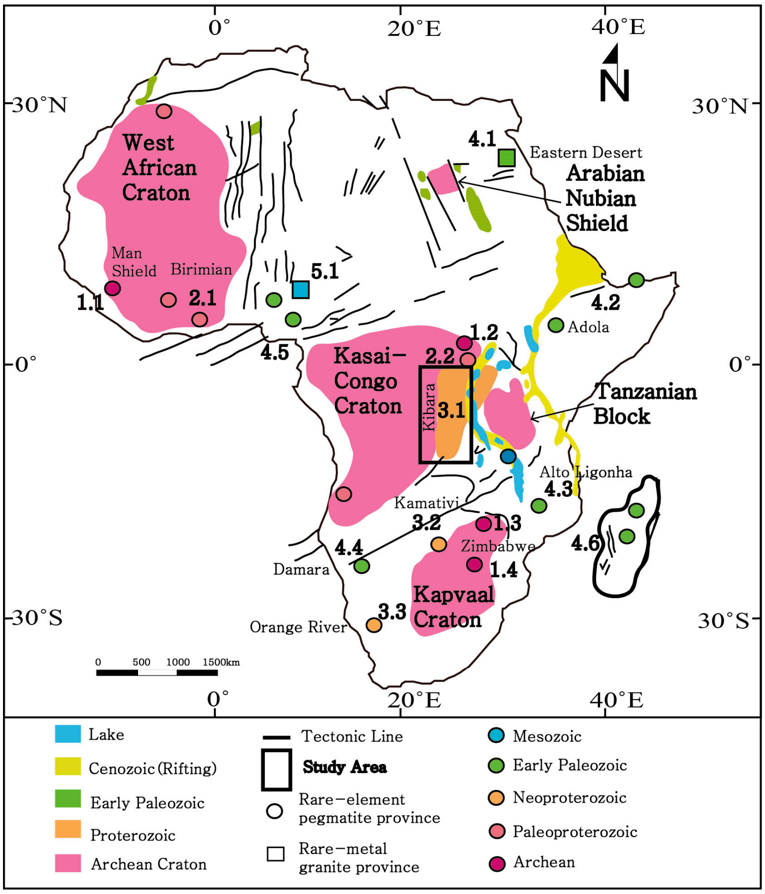

**Figure 1.** A simplified tectono-magmatic map of African rare-element pegmatite and rare-metal

granite provinces. Colors are related to age provinces. The black rectangle refers to the study area. The metallogenic provinces in Africa are as follows: 1.1 Man Shield, 1.2 Congo Craton, 1.3 Zimbabwe Craton, 1.4 Kaapvaal Craton; 2.1 Birimian Province, 2.2 Kibalian in north-eastern DRC; 3.1 Kibara Belt, 3.2 Kamativi Schist Belt, 3.3 Orange River Belt; 4.1 Eastern Desert, 4.2 Adola Belt, 4.3 Alto Ligonha Province, 4.4 Damara Belt, 4.5 Older Granites (Nigeria), 4.6 Madagascar; and 5.1 Younger Granites (Nigeria) [44].

The Kibara Belt (KIB) in the Democratic Republic of the Congo (DRC) contains massive Sn-W and other mineral-bearing granites as well as associated peri-granitic quartz veins [45–52]. A report up until 2010 for the KIB in the DRC stated an overall cumulative production of 800,000 tons of cassiterite, 30,000 tons of columbo-tantalite, 30,000 tons of wolframite, 600 tons of gold, and byproducts of bismuth, molybdenum, beryl, and amblygonite [51,53]. In the KIB, while petro-geochemical and tectono-structural characterizations of granitic intrusions and quartz veins have been studied [10,45–50], few investigations have combined cassiterite internal micro-textures, ore chemistry, and fluid inclusions to constrain the contribution of alteration and magmatic-hydrothermal fluid processes during Sn-W deposition. In this study, we provide combined results of fluid and ore chemistry to demonstrate the role of alteration and fluid processes in precipitating high-grade cassiterite and wolframite in the KIB in the DRC.

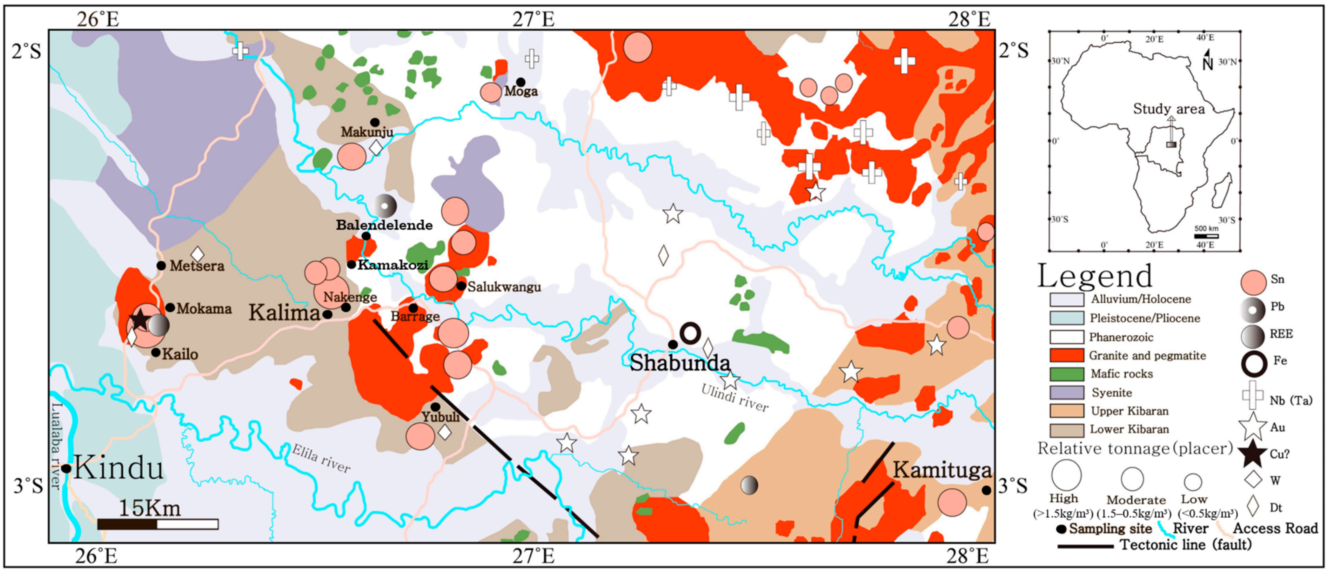

**Figure 2.** A map unit showing regional and local geology of the north-western Kibara belt (KIB) in the Maniema province in the Democratic Republic of the Congo [54,55]. The map includes the mineral resources and prospects of this part of the KIB, and sampling sites and localities are indicated by black spots.

## 2. Background Geology

### *2.1. Geological Settings of the KIB*

Africa comprises numerous Archean cratonic nuclei that are stitched together by several orogenic events [56–58], leading to break-up and accretion [48,59–63]. Geochronology based on Rb-Sr and zircon U-Pb indicates that the sub-Saharan region of Africa consists of Archean shields (e.g., Congo-Kasai craton and Tanzanian block, Figure 1) sutured by episodic orogens from the Archean to the Phanerozoic (Figures 1–3) [57,60,63]. The Mesoproterozoic Kibaran orogen in the DRC produced a belt named “Kibara Belt (KIB),” which is part of the extensive Central African Metallogenic Province (Figure 1) and hosts numerous high-grade Sn and W-Nb-Ta deposits associated with granites (Figures 2 and 3) [10,45,49–52,61,64–66].

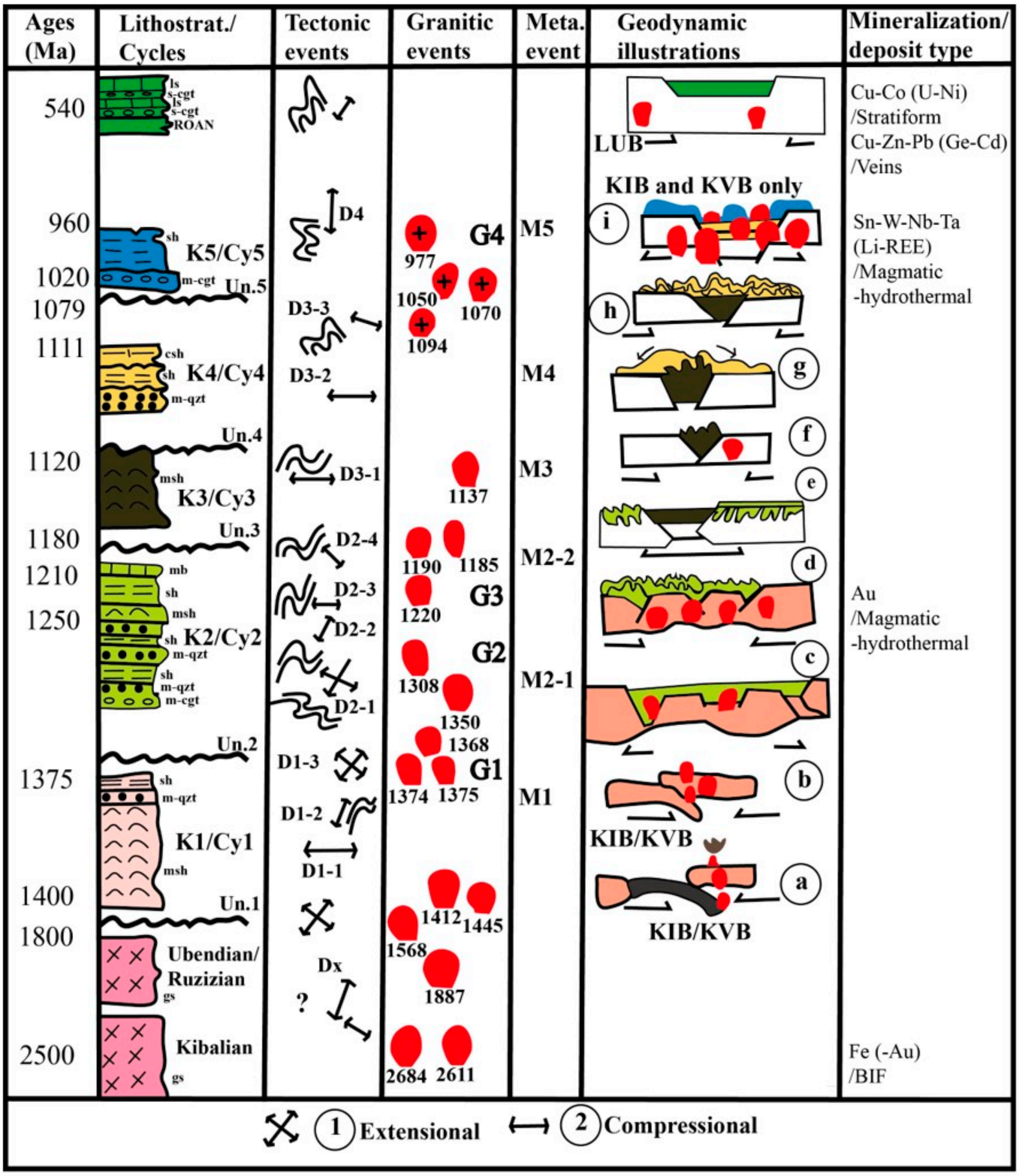

**Figure 3.** A synthesis of the KIB tectono-magmatic and stratigraphic units. Granitic intrusions in the Mesoproterozoic are subdivided into four clustering groups, designated G1 to G4. Only the latest G4 and its associated quartz veins and pegmatites are mineralized in the Sn oxide group and columbite group minerals. (K/Cy = tectonostratigraphic cycles; Un = major unconformities; D = tectonic events; G = main granitic events; M = main metamorphic events; a–i = main stages of the geodynamic evolution; 1—Extensional tectonic regime; 2—Compressional tectonic regime; Lithology: ls = limestone, s-cgt = sedimentary-conglomerate, sh = shale, m-cgt = metamorphic-conglomerate, csh = calc-schist, m-qtz = meta-quartzite, msh = micaschist, mb = marble, gs = gneiss; Orogens: KIB = Kibara belt, KIV = Kivu belt, LUB = Lufilian belt) [67].

The KIB's basement consists of metasediments, including metapelite-schist and granitic gneiss (Figure 3) [57,68–73]. The metamorphic rocks' foliation orientations in the belt are NE-SW in the southern part (in the provinces of Lualaba, Haut-Lomami, western Haut-Katanga, and Tanganyika), NW-SE in the northern part (Maniema province), and N-S in the central part (in the provinces of Maniema and South Kivu) [56,62,63,74]. The central and northern parts of the belt are covered by a siliciclastic sedimentary sequence of the Congo Basin with a thickness of about 10 km [62,63,75]. The Kibara metasedimentary basement was intruded by a series of barren and mineralized granites [8,14,44,49,70,76,77] and subordinate mafic bodies during the Mesoproterozoic orogeny [71,78] (Figure 3). Sn-W mineralized and barren quartz vein sets associated with the granitic intrusions crosscut both the granites and the metasedimentary basement [8,14,47,50,66,77,79–82]. The Mesoproterozoic KIB overrides the Paleoproterozoic belt "Ubende belt" [45] in the northern part, hosting Fe-Au mineralization [59], and in the southern part, it is partly overlapped by the Neoproterozoic belt "Lufilian belt or Zambian belt" known for Cu-Co deposits [57,58,60,83–94].

The KIB hosts valuable minerals, including cassiterite, wolframite, and columbite, which are the major primary ores associated with granites and peri-granitic quartz veins [44,49,50,95]. The KIB has secondary placer mineralization in alluvial and eluvial deposits in nearby rivers and valleys, about 1–2 km away from the primary mineralized granites and associated quartz veins (Figure 2) [47]. The eluvial gravel layer hosting the placers is less than 2 m thick, and the cassiterite (Sn) grade of the gravel ranges from 0.2 to 5 kg/m$^3$ (average cutoff grade: 0.5–1.5 kg/m$^3$) [47,51]. The Sn-W ores in the belt contain non-negligible amounts of by-products such as Nb, Ta, As, Hg, Pb, U, REE [53], and Au [52,96]. The geological settings of the KIB, including chronostratigraphic units, tectono-metamorphic events, and associated mineralization, are summarized in Figure 3 [67].

### 2.2. *The Tectono-Magmatism, Rock and Ore Classifications and Chronology*

The granitic intrusions in the KIB are peraluminous, S-type [12,82], and leucocratic granite [6,56,62,74,95,97], formed by crustal melting [9] of Al-rich metasedimentary rocks during the Kibaran orogeny [14,60]. The KIB granites are classified into three main phases based on ages, textures, and ore mineral contents (Figure 3) [48,67]. The first phase consists of pre- to syn-tectonic "barren" granitic intrusions (G1–G3, Figure 3) of 1100–1500 Ma [6,44,49,76], which are coarse-to-fine-grained and contain quartz, plagioclase, K-feldspar, and biotite. The second phase (this study) comprises Kibaran post-orogenic "Sn-(W) mineralized" granites (G4, Figure 3) of 950–1094 Ma [48,49,51,61]. These granites are equigranular and contain quartz, biotite-muscovite, albite, and accessory minerals such as hornblende, apatite, and ore minerals such as cassiterite, pyrite, chalcopyrite, and sphalerite. The third phase includes granitic pegmatites (G4 or G5, depending on their location in the DRC and Rwanda, respectively) of 755–950 Ma [48,82], which exhibit enrichment in Nb-Ta-Sn [81,95,98,99].

Two types of pegmatites are distinguished in the Kibara Belt: Li-Cs-Ta-rich (LCT-type) and Nb-Y-F-rich (NYF-type) [2,3,5,47,81,95,100]. These LCT (abundant) and NYF (rare) pegmatites consist of quartz and micas (biotite, muscovite, lepidolite, and spodumene) and accessory minerals such as plagioclases (albite-oligoclase), beryl, tourmaline, cassiterite, apatite, columbo-tantalite, phosphates, and rare sulfate minerals [6,44,61,76,95,97,101].

### 2.3. *The Petrography of the Sn(-W) Mineralized Granites*

The "second-phase G4" Sn-bearing granites in the KIB are composed of (1) equigranular granitic cupola (mineralized), (2) greisenized granites (mineralized), (3) pegmatites (mineralized), and (4) lenticularly injected and pipe-like granites of aplite (less mineralized) [6,10,48,49,77]. In this study, we focused on the mineralized granites (1-3) of the KIB in the Maniema province (Kalima and Mokama sites, Figure 2). The contact between granitic intrusions and the metasedimentary basement is generally tilted (at an angle greater than 60°). The contact between the mineralized granites and pegmatites (Kailo site, Figures 2 and 4i) often displays a lateral gradation of decreasing mineral sizes of mica flakes and aggregated quartz grains from pegmatite towards granites. Equigranular granitic intrusions often occur in large batholith bodies, approximately 4 to 7 km long and 1 to 2 km wide.

The mineralized granites consist of K-feldspar, quartz, albite, biotite, muscovite, and hornblende (Figures 4c,d and 5a,b). Some quartz grains contain inclusions of muscovite, sericite, and albite (Figure 4c). Orbicular textures and miarolitic cavities are observed in the granites. The cavities forming the miarolitic textures are up to 1–5 cm in diameter (Figure 5c). Greisenization is characterized by abundant muscovite (Figure 4c,d). These greisenized rocks (Salukwangu and Nakenge of Kalima sites; Figure 2) consist of quartz aggregates and muscovite flakes associated with minor black tourmaline (schorl), albite, lepidolite, topaz, and fluorite. In these rocks, the central parts primarily consist of quartz bordered with a dark rim of black tourmaline, and the outer parts contain mainly quartz and muscovite, with minor disseminations of black tourmaline, topaz, fluorite, and lepidolite. Cassiterite is found in the greisenized granites (abundant in the central, subsidiary in the outer parts) at the cupola or at the contact zone with the metasedimentary basement. Some equigranular granites, such as those in the Mokama site (MOKA-2-6 and MOKA-2-9; Figure 2), display sulfide minerals including chalcopyrite, bornite, sphalerite, pyrite, and supergene minerals such as chalcocite, covellite, and malachite.

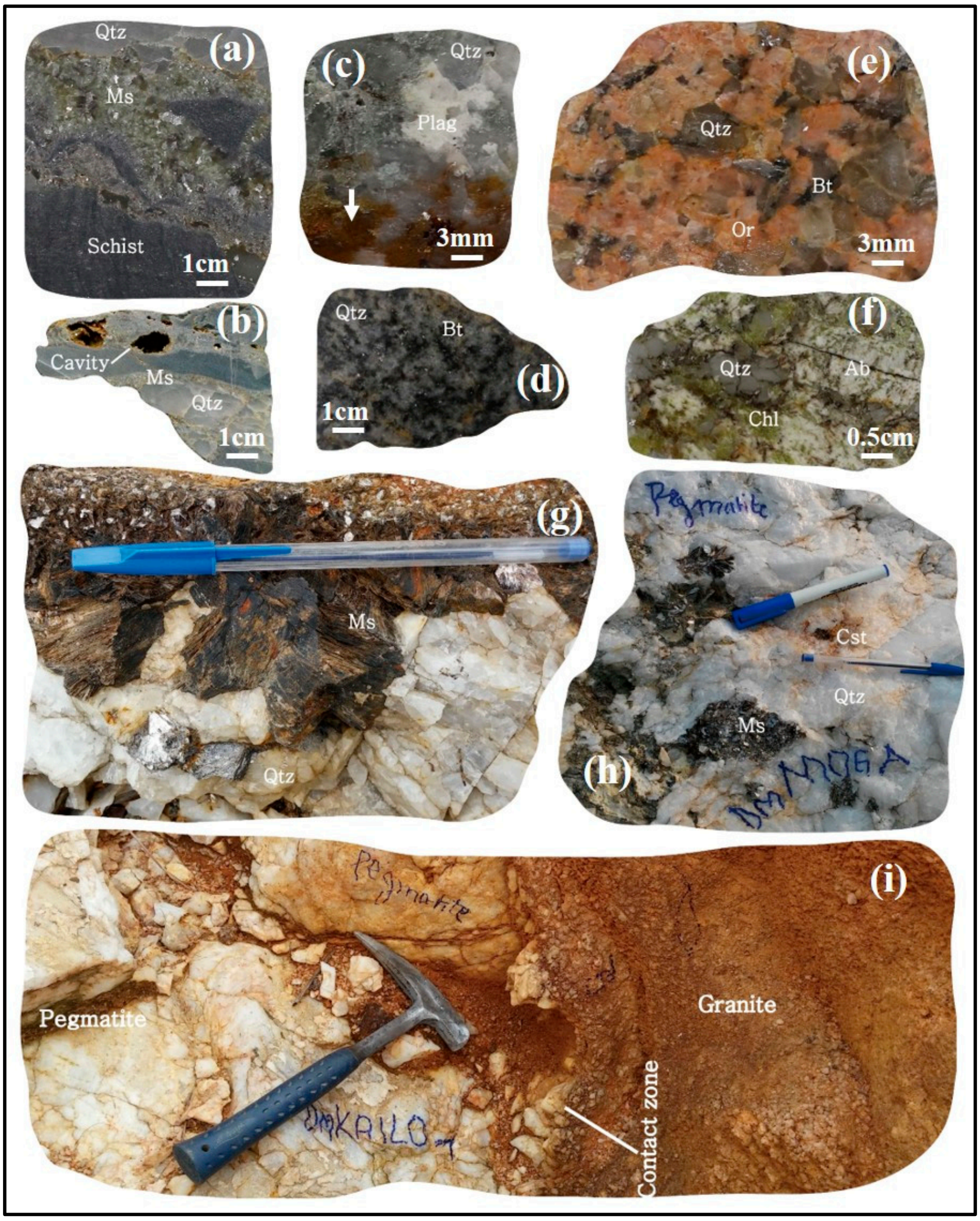

**Figure 4.** Representative field and rock sample photo macrographs from the KIB in the Maniema

province in the DRC [51,77]: (**a**,**b**) Mineralized quartz veins crosscutting schist and showing muscovite alterations and cavities from the Yubuli site; (**c**,**d**) Mineralized granites from the Mokama site displaying alteration features such as red selvage (white arrow) and miarolitic cavities; (**e**) A relatively fresh barren granite from the Barrage site displaying abundant k-feldspar (pinkish orthoclase); (**f**) Altered barren granite from the Balendelende site showing chloritization (green mass of chlorite) and albitization (giant laths of plagioclases, including albite); (**g**,**h**) mineralized pegmatites from the Moga site showing giant quartz crystals and big flakes of muscovite; (**i**) A contact zone between pegmatite and granite from the Kailo site showing shifting of mineral sizes. (Legend: *Qtz = quartz*, *Bt = biotite*, *Ms = muscovite*, *Chl = chlorite*, *Ab = albite*, *Plag = plagioclase*, *Cst = cassiterite*, *Or = orthoclase*).

**Figure 5.** Macrophotographs of representative quartz vein samples: (**a**,**b**) Barren quartz veins crosscutting

granites from the Mokama site; (**c**) Mineralized quartz veins from the Kalima (and Nakenge) site; (**d**) Mineralized quartz veins from the Batamba site showing recrystallized quartz that fills out cavities; (**e**,**f**) Mineralized quartz veins from the Batamba site showing schistosity, micro-folds, and micro-faults; (**g**) Mineralized quartz vein from the Yubuli site showing muscovite alteration; (**h**) A mineralized quartz vein from the Batamba site showing a micro-fault with displacement. (Legend: *Qtz = quartz*, *Ms = muscovite*, *Cst = cassiterite*, *Wft = wolframite*, *Py = pyrite*, *Fl = fluorite*).

The Sn (-W) mineralized pegmatites occur as lenticular or pipe-like bodies with diameters of less than 50 m. These pegmatites are in contact with the granite at the Kailo site (Figures 2 and 4i) or crosscut metasedimentary rocks in the Moga area (Figures 2 and 4g,h).

### *2.4. The Petrography of the Sn-W Quartz Veins*

Two types of quartz veins occur in the studied area: (1) Sn-W mineralized veins that crosscut the metasedimentary basement [14,45,47,50,66], and (2) barren veins that crosscut mainly granites and, less frequently, metasediments [63,69,72,73].

The Sn-W mineralized quartz veins have ages of 820–905 Ma (Ar-Ar on muscovite) [50]. The veins, with thicknesses of up to 15 cm (Figure 5f), consist of early euhedral quartz followed by later ores [45–49]. The paragenetic sequence among the ores is: (1) cassiterite, (2) cassiterite-wolframite, and (3) sulfides including arsenopyrite, pyrite, and molybdenite (Figures 4a,b and 5d,g) [47,48,50,66,79,80,102,103]. In the Yubuli and Mokama sites (Figure 2), a few mineralized quartz veins (Figures 4b,c and 5d) that crosscut the metasedimentary basement host sulfide minerals including arsenopyrite, chalcopyrite, sphalerite, pyrite, and rarely bornite. The Sn-W mineralized quartz veins are generally straight (Figures 4a,b and 5d,f–h), but often curved (Figure 5e), folded, or faulted (Figure 5e).

The barren quartz veins, with thicknesses of 1–5 cm (Figure 5a,b), consisting of pyrite, fluorite, and minor Fe oxides. They are straight and feature early pyrite followed by the intergrowth of euhedral quartz and fluorite (Figure 5a,b). These barren veins are thinner than the Sn-W mineralized veins.

### *2.5. Alteration Features*

The Sn-W bearing granites and quartz veins in the KIB display various alteration features. Halos of these alterations are characterized by the presence of minerals such as muscovite, sericite, albite, chlorite, and hematite (Figures 4a–i and 5a–d). We observed and classified the hypogene alteration assemblages into five groups: (1) quartz-chlorite-muscovite-sericite; (2) tourmaline-albite-topaz-muscovite-quartz; (3) tourmaline-muscovite; (4) hematite-pyrite; and (5) muscovite-quartz. Alteration assemblages 1–3 are dominant in the Sn-mineralized granites, while assemblage 4 is dominant in the barren quartz veins cutting the granite, and assemblage 5 is dominant in the Sn-W mineralized quartz veins cutting metasedimentary rocks. Among the mineralized granites, alteration (3) is dominant in the highest grade of Sn.

## 3. Materials and Methods

### *3.1. Sample Preparation for Mineral Geochemistry and Fluid Inclusions*

More than 15 polished sections of cassiterite and wolframite grains were prepared for petrography and mineral geochemistry. Minerals such as quartz, fluorite, and cassiterite hosting fluid inclusions were selected based on their alteration, lithology, and ore type (e.g., Sn, Sn-W, and barren), as well as cross-cutting relationships. The mineral grains or chips were doubly polished until they reached the required transparency under a polarized microscope (Nikon, Nikon Instruments Inc., New York, NY, USA) [104]. Approximately hundreds of mineral chips were prepared for the subsequent fluid inclusion study.

### *3.2. Microanalyses of Ore Minerals (SEM-CL, EPMA, EDS, and LA-ICP-MS)*

Cassiterite and wolframite compositions were determined by energy-dispersive spectroscopy (EDS; HR-SEM SU8010 series, Hi-Tech Instruments, Nanjing, China) at Inha University and an electron probe microanalyzer (EPMA) CAMECA SX100 series (CAMECA, Paris, France) at the Korean Basic Science Institute (KBSI) and Pusan National University in Korea (Table 1). The electron probe microscope consisted of a JEOL-JXA-8530F PLUS model and used an acceleration voltage of 15 kV, an acceleration current of 40 nA, and an electron beam of 3 mm. The analysis was conducted with a peak duration of 10 s and a background time of 5 s for Ti, Fe, and Mn, and both peak and background times of 40 s for the remained elements. Elements were measured on cassiterite (Sn, PET (2d = 8.7 Å), L$\alpha$), rutile (Ti, PET, K$\alpha$), hematite (Fe, LIF (2d = 4.0 Å), K$\alpha$), spessartine garnet (Mn, LIF, K$\alpha$), corundum (Al, TAP (2d = 25.8 Å), K$\alpha$), columbite (Nb, LIF, L$\alpha$), tantalite (Ta, TAP, M$\beta$), and wolframite (Mn, TAP, L$\alpha$). For the calibrations, standards are natural minerals: cassiterite for Sn, synthetic oxides: $MnTiO_3$ for Ti and $Fe_2O_3$ for Fe, and pure metals (Nb, Ta, and W), whose results were used as an internal standard for subsequent laser ablation (LA) ICP-MS. SEM-CL images were obtained from 15 representative grains of cassiterite and wolframite.

LA-ICP-MS microanalysis of trace elements (Tables 1–3) was performed on 67 spots for cassiterite, 7 for quartz, and 13 for wolframite. Micro-zonation obtained from the SEM-CL images was used for the LA-ICP-MS spot selection. We analyzed isotopes of 60 elements ($^{7}$Li, $^{9}$Be, $^{11}$B, $^{23}$Na, $^{25}$Mg, $^{27}$Al, $^{29}$Si, $^{31}$P, $^{39}$K, $^{42}$Ca, $^{45}$Sc, $^{49}$Ti, $^{51}$V, $^{53}$Cr, $^{55}$Mn, $^{57}$Fe, $^{59}$Co, $^{61}$Ni, $^{65}$Cu, $^{66}$Zn, $^{71}$Ga, $^{73}$Ge, $^{75}$As, $^{85}$Rb, $^{88}$Sr, $^{89}$Y, $^{90}$Zr, $^{93}$Nb, $^{95}$Mo, $^{107}$Ag, $^{111}$Cd, $^{113}$In, $^{118}$Sn, $^{121}$Sb, $^{133}$Cs, $^{137}$Ba, $^{139}$La, $^{140}$Ce, $^{141}$Pr, $^{146}$Nd, $^{147}$Sm, $^{151}$Eu, $^{157}$Gd, $^{159}$Tb, $^{163}$Dy, $^{165}$Ho, $^{167}$Er, $^{169}$Tm, $^{173}$Yb, $^{175}$Lu, $^{178}$Hf, $^{181}$Ta, $^{182}$W, $^{185}$Re, $^{197}$Au, $^{205}$Tl, $^{208}$Pb, $^{209}$Bi, $^{232}$Th, and $^{238}$U).

The LA-ICP-MS microanalyses were performed at the Korea Institute of Ocean Science and Technology (KIOST). The system consists of a 193 nm Argon-Excimer laser (LA-NWR 193) coupled with a quadrupole ICP-MS Agilent 7700x (Agilent Technologies, Santa Clara, CA, USA). The 10–12 spot laser ablations were bracketed with unknowns and standard reference materials (SRM; NIST-612 and BCR-2), with a repetition rate of 5 Hz and a laser energy of about 4–6 J/cm$^2$. The beam diameter of the ablations was 50 µm for both cassiterite and wolframite. A comparison of chemistry was established between cassiterite types and wolframite (Table 4).

**Table 1.** LA-ICP-MS and EPMA analytical results of major and trace elements in cassiterite (cross-section 1 in cassiterite DMYUB) hosted in the Yubuli quartz vein.

| **Major and Trace Element Distributions in Textured Cassiterite for Cross-Section 1** | | | | | | | | | | | |
|---|---|---|---|---|---|---|---|---|---|---|---|
| Orogen/Age: | Kibara belt (KIB)/Mesoproterozoic | | | | | | | | | | |
| Locality: | Yubuli (DMYUB) | | | | | | | | | | |
| Rock type: | Quartz vein | | | | | | | | | | |
| Mineral: | Cassiterite | | | | | | | | | | |
| Textures: | Oscillatory and Replacement | | | | | | | | | | |
| Ore type: | Type I | Type I | Type II | Type I | Type I | Type I | Type I | Type II | Type I | Type II | Type I |
| Samples | DMYUB 1_9_1 | DMYUB 1_9_2 | DMYUB 1_9_3 | DMYUB 1_9_4 | DMYUB 1_9_5 | DMYUB 1_9_6 | DMYUB 1_9_7 | DMYUB 1_9_8 | DMYUB 1_9_9 | DMYUB 1_9_10 | DMYUB 1_9_11 |
| Major elements | | | | | | | | | | | |
| $SnO_2$ (wt.%) | 99.1 | 98.9 | 98.3 | 97.9 | 98.5 | 99.0 | 98.7 | 97.6 | 98.3 | 99.6 | 98.8 |
| Total (wt.%) | 99.1 | 98.9 | 98.3 | 97.9 | 98.5 | 99.0 | 98.7 | 97.6 | 98.3 | 99.6 | 98.8 |
| Minor elements | | | | | | | | | | | |
| Li (ppm) | 11.79 | 8.70 | bdl | 1.97 | 2.50 | 1.03 | 1.18 | 2.61 | bdl | 1.83 | 0.62 |
| B (ppm) | 15.74 | 13.53 | 13.49 | 13.63 | 14.48 | 14.12 | 12.44 | 12.17 | 12.06 | 11.44 | 13.19 |
| Na (ppm) | 49.53 | 28.89 | bdl | 15.33 | 32.27 | bdl | bdl | 38.83 | bdl | 47.41 | bdl |
| Mg (ppm) | 1.00 | 0.03 | bdl | bdl | 0.05 | bdl | bdl | 1.00 | bdl | bdl | 1.00 |
| Al (ppm) | 12.55 | 9.56 | 101.34 | 19.12 | 15.48 | 7.71 | 8.54 | 71.50 | 11.84 | 80.78 | 8.37 |
| Si (ppm) | 1353.59 | 1167.90 | 1224.77 | 1424.93 | 1132.53 | 1243.20 | 1153.29 | 1130.62 | 1284.81 | 1045.29 | 1063.83 |
| P (ppm) | 5.00 | bdl | 19.79 | 23.97 | bdl | bdl | 3.00 | 11.00 | 3.00 | 9.00 | bdl |
| K (ppm) | 13.39 | 15.53 | bdl | bdl | 6.98 | bdl | bdl | 18.81 | bdl | 20.00 | bdl |
| Ca (ppm) | 2.00 | bdl | 1.00 | bdl | bdl | 3.00 | bdl | bdl | bdl | 5.00 | 4.00 |
| Sc (ppm) | 1.67 | 2.58 | 4.53 | 3.69 | 4.67 | 2.85 | 2.52 | 4.15 | 2.84 | 3.48 | 2.45 |
| Ti (ppm) | 310.61 | 161.93 | 65.72 | 462.91 | 503.36 | 638.53 | 856.18 | 396.39 | 595.92 | 740.65 | 832.54 |
| V (ppm) | 9.49 | 8.09 | 2.00 | 17.35 | 22.66 | 20.77 | 29.95 | 18.16 | 16.41 | 35.30 | 12.89 |
| Mn (ppm) | 3.00 | 3.13 | 1.39 | 8.54 | 0.83 | 0.71 | 0.62 | 3.68 | 0.86 | 5.69 | 1.27 |
| Fe (ppm) | 91.51 | 145.37 | 1456.51 | 182.58 | 222.50 | 109.42 | 142.63 | 601.87 | 161.67 | 490.51 | 203.06 |
| Co (ppm) | 13.52 | 13.77 | 13.67 | 14.17 | 13.39 | 14.18 | 14.14 | 14.06 | 12.45 | 13.80 | 13.58 |
| Ni (ppm) | 242.73 | 248.12 | 222.86 | 246.34 | 230.96 | 229.10 | 238.69 | 220.71 | 210.97 | 236.77 | 224.47 |
| Cu (ppm) | 0.50 | bdl | 1.00 | bdl | 0.30 | bdl | bdl | 2.06 | bdl | 6.15 | bdl |
| Zn (ppm) | 3.95 | 3.68 | 11.81 | 3.77 | 3.79 | 4.22 | 3.99 | 11.95 | 3.90 | 8.75 | 3.56 |
| Ga (ppm) | 0.31 | 0.43 | 3.99 | 0.43 | 0.67 | 0.32 | 0.31 | 1.57 | 0.45 | 0.43 | 0.31 |
| Ge (ppm) | bdl | bdl | 1.81 | bdl | 0.03 | bdl | bdl | 2.30 | bdl | 2.40 | bdl |
| As (ppm) | 4.70 | 1.53 | 11.52 | 1.47 | 1.51 | 1.66 | 1.52 | 9.29 | 1.64 | 29.47 | 1.52 |
| Rb (ppm) | 0.67 | 1.82 | bdl | bdl | 1.00 | bdl | 0.50 | bdl | 0.40 | bdl | 1.50 |
| Sr (ppm) | 2.06 | 0.76 | 0.21 | 0.80 | 0.70 | 2.18 | bdl | 0.73 | bdl | 0.69 | 0.34 |
| Y (ppm) | bdl | bdl | 0.15 | bdl | bdl | 0.01 | bdl | 0.04 | bdl | 0.14 | bdl |
| Zr (ppm) | 8.23 | 3.51 | 2.07 | 9.01 | 9.86 | 17.98 | 20.61 | 7.01 | 19.40 | 12.61 | 25.80 |
| Nb (ppm) | 2.08 | 0.35 | 0.25 | 0.33 | 0.82 | 1.76 | 0.73 | 1.19 | 0.17 | 2.38 | 107.36 |
| Ag (ppm) | 0.13 | bdl | 1.67 | bdl | 42.00 | bdl | 0.33 | 1.30 | bdl | 1.20 | bdl |
| In (ppm) | 2.12 | 2.76 | 28.19 | 4.60 | 5.89 | 2.95 | 2.85 | 13.98 | 4.06 | 4.31 | 2.33 |

**Table 1.** *Cont.*

| Major and Trace Element Distributions in Textured Cassiterite for Cross-Section 1 | | | | | | | | | | | |
|---|---|---|---|---|---|---|---|---|---|---|---|
| Minor elements | | | | | | | | | | | |
| Sb (ppm) | 0.76 | 0.41 | 1.43 | 0.44 | 0.61 | 0.42 | 0.50 | 0.62 | bdl | 0.39 | 0.45 |
| Cs (ppm) | 2.91 | 2.38 | 0.46 | 0.88 | 0.80 | 0.37 | 0.76 | 1.09 | 0.18 | 0.71 | 0.27 |
| Ba (ppm) | 4.11 | 3.78 | 2.89 | 2.99 | 3.30 | 3.04 | 2.93 | 3.13 | 3.50 | 3.44 | 3.54 |
| La (ppm) | 0.00 | bdl | bdl | bdl | bdl | bdl | bdl | 0.18 | bdl | 0.22 | bdl |
| Ce (ppm) | 0.50 | bdl | bdl | bdl | bdl | bdl | bdl | 0.77 | bdl | 1.72 | bdl |
| Pr (ppm) | 0.06 | 0.06 | 0.06 | 0.06 | bdl | bdl | bdl | 0.09 | 0.07 | 0.11 | 0.05 |
| Nd (ppm) | bdl | bdl | bdl | bdl | bdl | bdl | bdl | bdl | bdl | bdl | bdl |
| Sm (ppm) | bdl | bdl | bdl | bdl | bdl | bdl | bdl | bdl | bdl | bdl | bdl |
| Eu (ppm) | bdl | bdl | bdl | bdl | bdl | bdl | bdl | bdl | bdl | bdl | bdl |
| Gd (ppm) | bdl | bdl | bdl | bdl | bdl | bdl | bdl | bdl | bdl | bdl | bdl |
| Tb (ppm) | bdl | bdl | bdl | bdl | bdl | bdl | bdl | bdl | bdl | bdl | bdl |
| Dy (ppm) | bdl | bdl | bdl | bdl | bdl | bdl | bdl | bdl | bdl | bdl | bdl |
| Ho (ppm) | bdl | bdl | bdl | bdl | bdl | bdl | bdl | bdl | bdl | bdl | bdl |
| Er (ppm) | bdl | bdl | bdl | bdl | bdl | 0.58 | bdl | bdl | bdl | bdl | bdl |
| Tm (ppm) | bdl | bdl | bdl | bdl | bdl | bdl | bdl | bdl | bdl | bdl | bdl |
| Yb (ppm) | bdl | bdl | bdl | bdl | bdl | bdl | bdl | bdl | bdl | bdl | bdl |
| Lu (ppm) | bdl | bdl | bdl | bdl | bdl | bdl | bdl | bdl | bdl | bdl | bdl |
| Hf (ppm) | 0.16 | bdl | bdl | 0.17 | 0.15 | 0.53 | 0.56 | bdl | 0.49 | 0.20 | 0.70 |
| Ta (ppm) | 0.34 | 0.14 | 0.05 | 0.05 | 0.05 | 0.05 | 0.05 | 0.02 | 0.05 | 0.05 | 0.65 |
| W (ppm) | 25.79 | 5.94 | 67.44 | 20.16 | 22.56 | 5.88 | 4.77 | 88.34 | 7.56 | 152.52 | 4503.61 |
| Au (ppm) | bdl | bdl | 1.90 | bdl | 0.02 | bdl | bdl | 2.00 | bdl | 3.00 | bdl |
| Tl (ppm) | bdl | bdl | bdl | bdl | bdl | 0.40 | bdl | bdl | bdl | bdl | bdl |
| Pb (ppm) | 1.06 | 1.64 | 0.32 | 0.13 | 0.11 | 0.13 | 0.15 | 0.94 | 0.12 | 2.15 | 0.14 |
| Bi (ppm) | 0.89 | 0.07 | 0.07 | 0.07 | 0.06 | 0.07 | 0.07 | 1.05 | 0.07 | 3.86 | 0.06 |
| Th (ppm) | 0.07 | 0.05 | 0.05 | 0.05 | 0.05 | bdl | 0.05 | 0.06 | 0.05 | 0.26 | bdl |
| U (ppm) | 0.12 | 0.11 | 2.82 | 0.25 | 0.24 | 0.10 | 0.13 | 0.64 | 0.13 | 0.21 | 2.46 |
| ∑REE (ppm) | 0.6 | 0.1 | 0.1 | 0.1 | bdl | 0.6 | bdl | 1.0 | 0.1 | 2.1 | 0.1 |
| Ti/Fe | 3.39 | 1.11 | 0.05 | 2.54 | 2.26 | 5.84 | 6.00 | 0.66 | 3.69 | 1.51 | 4.10 |
| In/Ta | 6.24 | 19.75 | 563.78 | 91.98 | 117.84 | 58.96 | 57.10 | 698.79 | 81.27 | 86.29 | 3.58 |
| Al/Nb | 6.04 | 27.18 | 403.96 | 57.34 | 18.81 | 4.38 | 11.78 | 60.29 | 68.46 | 33.94 | 0.08 |
| V/Fe | 0.10 | 0.06 | n.a. | 0.10 | 0.10 | 0.19 | 0.21 | 0.03 | 0.10 | 0.07 | 0.06 |

Footnote: bdl = below the detection limit.

### 3.3. Fluid Inclusion Study (Microthermometry and Laser Raman Spectroscopy)

For the fluid inclusion study, 300 doubly-polished chips of quartz (180), fluorite (30), and cassiterite (90) from 100 doubly polished sections were used. Petrographic descriptions of fluid inclusion (FI) types and their assemblages (FIAs) were performed under a transmitted light microscope and are reported in the following result section. Laser Raman spectroscopy on bubble parts of more than 40 aqueous fluid inclusions was performed at Inha University. We used the Raman confocal laser (Horiba, LabRam HR Evolution model, Horiba Ltd., Kyoto, Japan) to detect trapped gas species such as $CO_2$, $CH_4$, $N_2$, and $H_2$ in the inclusions [34,105]. The laser was equipped with alternating 532 and 785 nm edge filters, an adjustable spot size of 1–5 μm, and an integration laser timing of 10–40 s.

For fluid inclusion microthermometry, we used a heating-cooling stage of Linkam-FTIR 600 to determine ice melting and total homogenization ($T_h$) of FIs [106,107]. The stage calibration was performed using synthetic fluid inclusions (aqueous $CO_2$–$CH_4$ bearing inclusion and pure water inclusion) to obtain the triple point (−57.1 °C) of the $CO_2$–$CH_4$ mixed aqueous inclusion and ice melting (0.0 °C) and the critical homogenization temperature (374 °C) of the pure water inclusion. We analyzed about 3–6 aqueous liquid-rich inclusions in a single assemblage (FIA), and the result of each assemblage was reported as an average ± standard deviation (1σ) for its salinity and homogenization temperature (Table 5) [19,108–111]. The obtained microthermometric results were processed by the SOWAT software (a NaCl-$H_2O$ model system) to obtain an isochoric curve in the P-T-X system (Table 5).

**Table 2.** LA-ICP-MS and EPMA microanalyses on cassiterite in Nakenge granites and wolframite in Yubuli quartz veins.

| **LA ICPMS Major and Trace Element Data for Cassiterite Hosted in Granite, and Wolframite in Quartz Vein** | | | | | | | | | | | | | | | |
|---|---|---|---|---|---|---|---|---|---|---|---|---|---|---|---|
| Orogen/Age: | Kibara belt (KIB)/Mesoproterozoic | | | | | | | | | | | | | | |
| Locality: | Nakenge (DMNAKE) | | | | Yubuli (DMYUB) | | | | | | | | | | |
| Rock type: | Granite (greisen) | | | | Quartz vein | | | | | | | | | | |
| Mineral: | Cst | Cst | Cst | Cst | Wft | Wft | Wft | Wft | Wft | Wft | Wft | Wft | Wft | Wft | Wft |
| Textures: | Oscillatory and Replacement | | | | Homogenous (No internal texture observed). | | | | | | | | | | |
| Ore type: | Type II | Type II | Type I | Type II | | | | | | | | | | | |
| Samples | DMNAKE 117_12 | DMNAKE 117_10 | DMNAKE 117_5 | DMNAKE 118_2 | DMYUB 1_14_1 | DMYUB 1_14_2 | DMYUB 1_14_3 | DMYUB 1_14_4 | DMYUB 1_14_5 | DMYUB 1_11_1 | DMYUB 1_11_2 | DMYUB 1_11_9 | DMYUB 1_11_10 | DMYUB 1_11_11 | DMYUB 1_11_12 |
| Major elements | | | | | | | | | | | | | | | |
| $SnO_2$ (wt.%) | 98.5 | 97.6 | 98.3 | 97.9 | t.e. | t.e. | t.e. | t.e. | t.e. | t.e. | t.e. | t.e. | t.e. | t.e. | t.e. |
| $WO_3$ (wt.%) | t.e. | t.e. | t.e. | t.e. | 74.8 | 75.2 | 73.9 | 74.2 | 74.1 | 75.8 | 74.5 | 75.5 | 74.1 | 73.6 | 74.2 |
| FeO (wt.%) | t.e. | t.e. | t.e. | t.e. | 17.6 | 18.4 | 17.9 | 17.6 | 17.6 | 16.7 | 17.8 | 17.2 | 18.5 | 18.4 | 17.0 |
| MnO (wt.%) | t.e. | t.e. | t.e. | t.e. | 6.6 | 5.9 | 6.9 | 6.8 | 6.4 | 6.7 | 6.2 | 6.1 | 6.5 | 6.3 | 6.9 |
| Total (wt.%) | 98.5 | 97.6 | 98.3 | 97.9 | 99.0 | 99.5 | 98.7 | 98.6 | 98.1 | 99.2 | 98.5 | 98.8 | 99.1 | 98.3 | 98.1 |
| Minor elements | | | | | | | | | | | | | | | |
| Li (ppm) | 4686.1 | bdl | 19.3 | bdl | 14.1 | 1.2 | 7.9 | 5.7 | 0.0 | bdl | bdl | bdl | bdl | bdl | bdl |
| B (ppm) | 15.3 | 10.7 | 8.0 | 15.91 | 4.7 | 7.3 | 0.0 | 6.6 | 8.8 | bdl | bdl | bdl | bdl | bdl | bdl |
| Na (ppm) | 58.4 | 0.0 | 20.1 | 0.00 | 224.7 | 0.0 | 51.8 | 81.5 | 30.6 | bdl | bdl | bdl | bdl | bdl | bdl |
| Mg (ppm) | 2123.6 | 0.0 | 12.9 | 10.64 | 180.2 | 190.8 | 191.7 | 206.0 | 280.6 | bdl | bdl | 204.0 | bdl | bdl | bdl |
| Al (ppm) | 2140.3 | 10.6 | 23.2 | 14.38 | 10.0 | 11.0 | 9.3 | 10.9 | 13.8 | bdl | bdl | bdl | bdl | bdl | bdl |
| Si (ppm) | 5950.7 | 2331.3 | 3671.1 | 2017.06 | 0.0 | 783.5 | 1241.0 | 975.7 | 796.7 | bdl | bdl | bdl | bdl | bdl | bdl |
| P (ppm) | 0.0 | 0.0 | 242.4 | 0.00 | 0.0 | 0.0 | 0.0 | 0.0 | 0.0 | bdl | bdl | bdl | bdl | bdl | bdl |
| K (ppm) | 3636.0 | 0.0 | 33.7 | 0.0 | 38.4 | 0.0 | 0.0 | 21.4 | 0.0 | bdl | bdl | bdl | bdl | bdl | bdl |
| Ca (ppm) | 0.0 | 0.0 | 0.0 | 0.0 | 0.0 | 0.0 | 0.0 | 0.0 | 0.0 | bdl | bdl | bdl | bdl | bdl | bdl |
| Sc (ppm) | 4.8 | 2.5 | 1.9 | 2.9 | 12.8 | 12.3 | 14.8 | 21.0 | 15.6 | bdl | bdl | bdl | bdl | bdl | bdl |
| Ti (ppm) | 1540.0 | 1634.3 | 2031.4 | 1709.6 | 0.0 | 0.0 | 0.0 | 16.9 | 20.6 | bdl | bdl | bdl | bdl | bdl | bdl |
| V (ppm) | 9.0 | 6.0 | 6.4 | 6.1 | 0.0 | 0.0 | 0.0 | 0.5 | 1.2 | bdl | bdl | bdl | bdl | bdl | bdl |
| Mn (ppm) | 126.0 | 6.8 | 11.8 | 10.3 | m.e. | m.e. | m.e. | m.e. | m.e. | m.e. | m.e. | m.e. | m.e. | m.e. | m.e. |
| Fe (ppm) | 842.7 | 87.4 | 69.3 | 153.2 | m.e. | m.e. | m.e. | m.e. | m.e. | m.e. | m.e. | m.e. | m.e. | m.e. | m.e. |
| Co (ppm) | 13.0 | 11.9 | 12.8 | 13.4 | bdl | bdl | bdl | bdl | bdl | bdl | bdl | bdl | bdl | bdl | bdl |
| Ni (ppm) | 176.6 | 173.7 | 180.5 | 210.4 | bdl | bdl | bdl | bdl | bdl | bdl | bdl | bdl | bdl | bdl | bdl |
| Cu (ppm) | 2.2 | 0.0 | 0.0 | 0.0 | bdl | bdl | bdl | bdl | bdl | bdl | bdl | bdl | bdl | bdl | bdl |
| Zn (ppm) | 24.5 | 9.2 | 15.1 | 12.1 | 37.1 | 38.1 | 44.3 | 40.0 | 45.9 | bdl | bdl | bdl | bdl | bdl | bdl |
| Ga (ppm) | 6.6 | bdl | 0.7 | 0.6 | 0.5 | bdl | bdl | bdl | bdl | bdl | bdl | bdl | bdl | bdl | bdl |
| Ge (ppm) | bdl | bdl | bdl | bdl | bdl | bdl | bdl | bdl | bdl | bdl | bdl | bdl | bdl | bdl | bdl |
| As (ppm) | bdl | bdl | bdl | 4.6 | bdl | bdl | bdl | 2.5 | bdl | bdl | bdl | bdl | bdl | bdl | bdl |
| Rb (ppm) | 452.4 | bdl | bdl | bdl | 0.6 | bdl | bdl | 0.5 | bdl | bdl | bdl | bdl | bdl | bdl | bdl |
| Sr (ppm) | 0.3 | bdl | 0.1 | 0.1 | 2.3 | bdl | 1.0 | 1.7 | 0.6 | 1.2 | bdl | bdl | bdl | 1.2 | bdl |
| Y (ppm) | 0.0 | 2.8 | 1.1 | 0.0 | 2.1 | 3.4 | 1.1 | 2.3 | 3.9 | bdl | 7.9 | bdl | 2.1 | 3.6 | 9.3 |
| Zr (ppm) | 157.7 | 169.5 | 188.7 | 167.9 | bdl | bdl | bdl | 0.5 | 4.8 | 1.0 | bdl | 1.3 | bdl | bdl | bdl |
| Nb (ppm) | 1085.3 | 1197.7 | 278.6 | 587.1 | 31.1 | 36.5 | 12.0 | 180.1 | 160.9 | 188.8 | 121.5 | 133.5 | 95.8 | 365.1 | 246.9 |
| Ag (ppm) | bdl | bdl | bdl | bdl | bdl | bdl | 1.9 | 1.0 | bdl | 3.2 | bdl | bdl | bdl | 3.6 | 6.9 |
| In (ppm) | bdl | bdl | bdl | bdl | 4.1 | 3.7 | 3.9 | 5.9 | 5.6 | bdl | bdl | bdl | bdl | bdl | bdl |
| Sn (ppm) | m.e. | m.e. | m.e. | m.e. | bdl | bdl | 7.0 | bdl | 26.5 | bdl | bdl | bdl | bdl | bdl | bdl |
| Sb (ppm) | 1.1 | bdl | 1.7 | 0.9 | bdl | bdl | bdl | bdl | bdl | bdl | bdl | bdl | bdl | bdl | bdl |
| Cs (ppm) | 73.4 | 0.5 | 0.5 | 0.4 | 2.2 | bdl | 0.5 | 1.3 | 0.3 | bdl | bdl | bdl | bdl | bdl | bdl |
| Ba (ppm) | 26.8 | 10.3 | 9.0 | 5.7 | 1.7 | bdl | 2.0 | 1.8 | 1.1 | bdl | bdl | bdl | bdl | bdl | 23.3 |
| La (ppm) | 0.22 | 0.16 | 0.17 | 0.15 | bdl | bdl | 0.20 | 0.22 | bdl | 0.85 | bdl | bdl | bdl | bdl | 3.79 |
| Ce (ppm) | 0.12 | 0.24 | 0.09 | 0.12 | bdl | bdl | 0.29 | 1.07 | 0.27 | 4.43 | bdl | 1.25 | bdl | bdl | 9.19 |
| Pr (ppm) | 0.18 | 0.21 | 0.15 | 0.12 | bdl | bdl | bdl | 0.09 | 0.49 | 0.37 | bdl | 0.14 | bdl | bdl | 1.43 |
| Nd (ppm) | bdl | bdl | bdl | bdl | bdl | bdl | bdl | 0.51 | bdl | 2.01 | bdl | bdl | bdl | bdl | 7.21 |
| Sm (ppm) | bdl | bdl | bdl | bdl | 0.89 | bdl | bdl | bdl | bdl | bdl | bdl | bdl | bdl | bdl | 3.00 |
| Eu (ppm) | bdl | bdl | bdl | bdl | bdl | bdl | bdl | bdl | bdl | bdl | bdl | bdl | bdl | bdl | 1.13 |
| Gd (ppm) | bdl | bdl | bdl | bdl | bdl | bdl | bdl | bdl | bdl | bdl | bdl | bdl | bdl | bdl | bdl |

**Table 2.** *Cont.*

| **LA ICPMS Major and Trace Element Data for Cassiterite Hosted in Granite, and Wolframite in Quartz Vein** | | | | | | | | | | | | | | | |
|---|---|---|---|---|---|---|---|---|---|---|---|---|---|---|---|
| Minor elements | | | | | | | | | | | | | | | |
| Tb (ppm) | bdl | bdl | bdl | bdl | bdl | bdl | bdl | 0.08 | 0.12 | bdl | bdl | bdl | bdl | bdl | bdl |
| Dy (ppm) | bdl | bdl | bdl | bdl | 0.53 | 0.46 | 0.52 | 0.74 | 1.29 | 1.28 | bdl | bdl | bdl | bdl | 4.17 |
| Ho (ppm) | bdl | 0.09 | bdl | bdl | 0.18 | 0.21 | 0.16 | 0.25 | 0.48 | bdl | 1.07 | 0.23 | bdl | bdl | bdl |
| Er (ppm) | bdl | 0.50 | bdl | bdl | 1.34 | 1.48 | 0.74 | 1.68 | 2.68 | bdl | bdl | 1.28 | 1.33 | bdl | 4.17 |
| Tm (ppm) | bdl | 0.13 | bdl | bdl | 0.45 | 0.47 | 0.31 | 0.49 | 0.76 | bdl | 1.87 | bdl | 0.36 | bdl | 1.04 |
| Yb (ppm) | bdl | 0.61 | 0.45 | bdl | 5.29 | 5.60 | 3.52 | 6.32 | 9.14 | 8.28 | 21.64 | bdl | 4.76 | 8.63 | 12.08 |
| Lu (ppm) | 0.11 | 0.19 | 0.11 | 0.07 | 1.06 | 1.14 | 1.01 | 1.32 | 1.95 | 1.68 | bdl | 1.28 | 1.02 | bdl | 2.39 |
| Hf (ppm) | 16.9 | 15.4 | 20.1 | 19.4 | bdl | bdl | bdl | bdl | bdl | bdl | bdl | bdl | bdl | bdl | bdl |
| Ta (ppm) | 3578.0 | 2822.3 | 1528.2 | 4177.9 | 0.9 | 0.9 | 0.9 | 1.2 | 3.9 | 4.7 | bdl | 1.2 | 1.0 | 7.4 | 8.6 |
| W (ppm) | 2.8 | 6.4 | 121.5 | 27.5 | m.e. | m.e. | m.e. | m.e. | m.e. | m.e. | m.e. | m.e. | m.e. | m.e. | m.e. |
| Au (ppm) | 5.4 | 4.2 | 1.8 | 3.1 | 1.8 | 0.6 | 0.6 | 0.6 | 0.5 | bdl | bdl | 0.5 | bdl | bdl | bdl |
| Tl (ppm) | 2.5 | bdl | bdl | bdl | 0.1 | bdl | bdl | bdl | bdl | bdl | bdl | bdl | bdl | bdl | bdl |
| Pb (ppm) | 0.3 | bdl | bdl | bdl | bdl | bdl | 9.6 | 33.6 | 3.6 | 93.3 | 49.9 | 63.9 | bdl | bdl | 75.5 |
| Bi (ppm) | bdl | 1.1 | 0.3 | bdl | bdl | bdl | 2.0 | 25.3 | 3.9 | 48.9 | bdl | 13.2 | bdl | bdl | 9.7 |
| Th (ppm) | bdl | 0.7 | 0.1 | bdl | bdl | bdl | bdl | 0.1 | 0.1 | bdl | bdl | bdl | bdl | bdl | bdl |
| U (ppm) | 0.4 | 2.7 | 1.0 | 0.5 | bdl | bdl | 0.2 | 0.1 | 0.3 | bdl | bdl | 0.3 | bdl | bdl | bdl |
| ∑REE (ppm) | 0.6 | 2.1 | 1.0 | 0.5 | 9.7 | 9.4 | 6.7 | 12.7 | 17.2 | 18.9 | 24.6 | 4.2 | 7.5 | 8.6 | 49.6 |
| Ti/Fe | 1.83 | 18.70 | 29.30 | 11.16 | n.a | n.a | n.a | n.a | n.a | n.a | n.a | n.a | n.a | n.a | n.a |
| In/Ta | n.a | n.a | n.a | n.a | 4.47 | 3.97 | 4.30 | 4.70 | 1.42 | n.a | n.a | n.a | n.a | n.a | n.a |
| Al/Nb | 1.97 | 0.01 | 0.08 | 0.02 | 0.32 | 0.30 | 0.78 | 0.06 | 0.09 | n.a | n.a | n.a | n.a | n.a | n.a |
| V/Fe | 0.01 | 0.07 | 0.09 | 0.04 | n.a | n.a | n.a | n.a | n.a | n.a | n.a | n.a | n.a | n.a | n.a |

Footnotes: t.e. = trace element excluded, m.e. = major element excluded, bdl = below the detection limit, n.a. = not analyzed, Cst = cassiterite, and Wft = wolframite.

## 4. Results

### 4.1. Sn-W Minerals and Their Micro-Textures

The cassiterite hosted in the granites and quartz veins can be subdivided into Type I (yellow and transparent) and Type II (dark-red and translucent) under macroscopic observation (Figures 6a,b and 7c). The co-occurrences of Type I and II cassiterite, as well as their spatial relationships, display various textural features, such as oscillatory (or growth) zoning (Figure 6a–d) and replacement (Figure 6b,d). These micro-textures are unambiguously observed under SEM-CL images and petrographic microscopes (Figures 6, 7 and 8a). Type I is relatively highly luminescent and displays lighter bands compared to Type II, which shows lower luminescence and darker bands (Figures 6c,d and 7a,b). These two cassiterites occur as alternating or interchanging bands of "oscillatory or growth zones" (Figures 6a–d and 7a–c). Type II replaces Type I as a "replacement texture" (Figures 6d and 7c).

The oscillatory zoning texture (or growth zone) consists of concentric bands of interchanging relative brightness and colors or kink fold-like alternating CL bands of Type I and Type II (Figures 6a–d, 7a–c and 8a). The replacement texture exhibits a zone of substitution of one cassiterite type by another type or by wolframite in the W-bearing ores (Figures 6d and 7c). Type I is replaced by Type II through micro-fractures such as cracks and elbow zones (Figure 7b,c). Cassiterites in the quartz veins and granites display relatively thicker oscillating bands compared to cassiterites in the pegmatites, which show thinner bands of less than 50 μm in width.

In the quartz veins, wolframite replaces cassiterite (especially Type II) (Figure 6d). Wolframite does not display a zonal feature; it is homogeneously dark under CL (Figures 6b,d and 7c). Spots for LA-ICP-MS microanalyses on cassiterite and wolframite were selected based on micro-textural information (Figure 8a–c).

### 4.2. Compositions of Cassiterite and Wolframite

Two types of cassiterite and wolframite (darker and brighter SEM-CL) (Figures 6c,d, 7a,b and 8a) were analyzed by LA-ICP-MS (Tables 1–3). Cross-sections of compositions of cassiterite and wolframite crystals were obtained (Yubuli site; Figure 8a and Table 1). LA-ICP-MS transient signals of the two types show contrasting concentrations of trace elements (Figure 8b,c).

Trace elements in cassiterite (Figures 8b,c and 9a–d; Tables 1–3) indicate that Fe, Al, In, and Ga are relatively enriched in Type II, whereas Ti, Zr, Hf, Nb, Ta, and V show relative enrichment in Type I (Figure 9a–d; Tables 1–3). Si, Cu, Ni, Sc, and Co show no preference in the cassiterites (Figure 9a). Cassiterite crystals displayed both Ce-positive (Figure 10d; Yubuli quartz veins) and negative (Figure 10c; Nakenge granite and greisen) anomaly values (Chondrite normalized Ce/Ce* = 2Ce/(La + Pr)). Wolframite also displayed both Ce positive and negative anomalies (Figure 10a,b). The Ce anomaly values range from 0.8–7.1 for Type II cassiterite, 0.7–2.8 for Type I cassiterite, and 0.8–2.5 for wolframite. In wolframite, compared to cassiterite, trace elements including Pb, Bi, Ba, and HREE (Figure 10a,b) show relatively higher concentrations, whereas Ti, V, Ga, As, Zr, Ta, and U are lower (Figure 10c,d; Tables 1–4).

Atomic ratios, including V/Fe (<0.07) and Ti/Fe (0.03–1.5), are relatively lower in Type II cassiterite compared to Type I (V/Fe and Ti/Fe are respectively 0.03–0.2 and 0.1–2.3). In/Ta ratios (86.3–698.8) in Type II cassiterite are higher than in Type I (0.2–92.0). In wolframite, ratios of In/Ta (1.4–4.7) and Al/Nb (<0.8) are relatively lower compared to cassiterites.

### *4.3. The Petrographic Descriptions of the KIB Fluid Inclusions*

Fluid inclusions (FIs) are found in various minerals in the KIB, including quartz, cassiterite, and fluorite. We selected host minerals based on three criteria: (1) petrography (barren granites, Sn-bearing granites, and Sn-W quartz veins); (2) crosscutting relationships (quartz veins intersecting either granite or metasediments); and (3) alteration features. We chose host minerals and their FIs as follows: (a) quartz in barren granites (DMBAR-1, DMKAILO-1, and BALE-1; Figure 2); (b) quartz in Sn-bearing granites (DMMOKA-2, DMMOKA-2-6, DMMOKA-2-4, DMMOKA-2-7, DMMOKA-2-8, DMMOGA-1, and DMNAKE-1; Figure 2); (c) quartz in barren quartz veins crosscutting Sn granite (DMMOKA-2-7 and DMMOKA-2-8; Figure 2); (d) quartz in Sn-W quartz veins crosscutting metasedimentary rocks (e.g., Schist, DMYUB-1, DMMET-1, DMBAT-1, and DMNAKE-1; Figures 2 and 5c–g); (e) fluorite in barren quartz veins crosscutting Sn mineralized granite (DMMOKA-2-8; Figures 2 and 5a,b); and (f) cassiterite in mineralized quartz veins and granites (DMYUB-1, DMMAKU-1, DMBAT-1, and DMNAKE-1; Figures 4g,h and 5c–g; Table 5).

After detailed petrographic observations, we identified texturally co-genetic fluid inclusion assemblages (FIAs) (Figure 11a,e,j), randomly clustered (Figure 11b,f,k) or aligned (Figure 11h,j,l) along a healing fracture or growth zone. Primary FIAs are rare in quartz and fluorite, while secondary and pseudo-secondary FIAs are common. In cassiterite, we observed primary (Figure 11a,h), secondary, and pseudo-secondary assemblages (Figure 11a,b,g). We used pseudo-secondary and primary FIAs hosted in cassiterite and pseudo-secondary FIAs for quartz and fluorite.

In quartz and cassiterite, we distinguished four types of inclusions based on their phase proportion: (1) aqueous liquid-rich inclusions (liquid-rich: Figure 11a,b,f,l,m); (2) aqueous vapor-rich inclusions (vapor-rich: Figure 11e,j); (3) aqueous intermediate-density inclusions (ID: Figure 11b,g,i,k,l); and (4) aqueous carbonic-bearing inclusions (carbonic-bearing; Figure 11c). Salt-bearing brine inclusions were not observed. The bubble sizes (estimated vol.%) in the liquid-rich, vapor-rich, ID, and carbonic-bearing inclusions are 10–30, 70–100, 50, and 70–90, respectively. A few liquid-rich and carbonic-bearing inclusions contain dark daughter minerals, possibly metal oxides or sulfides (Figure 11j). Some fluid inclusion assemblages (FIAs) in quartz in the Sn-bearing granites (e.g., the Mokama site, Figure 2) show co-occurrence of liquid- and vapor-rich inclusions, possibly a "boiling assemblage" (Figure 11j). Fluorite predominantly hosts relatively small-sized (<20 µm in diameter) liquid-rich inclusions (Figure 11d).

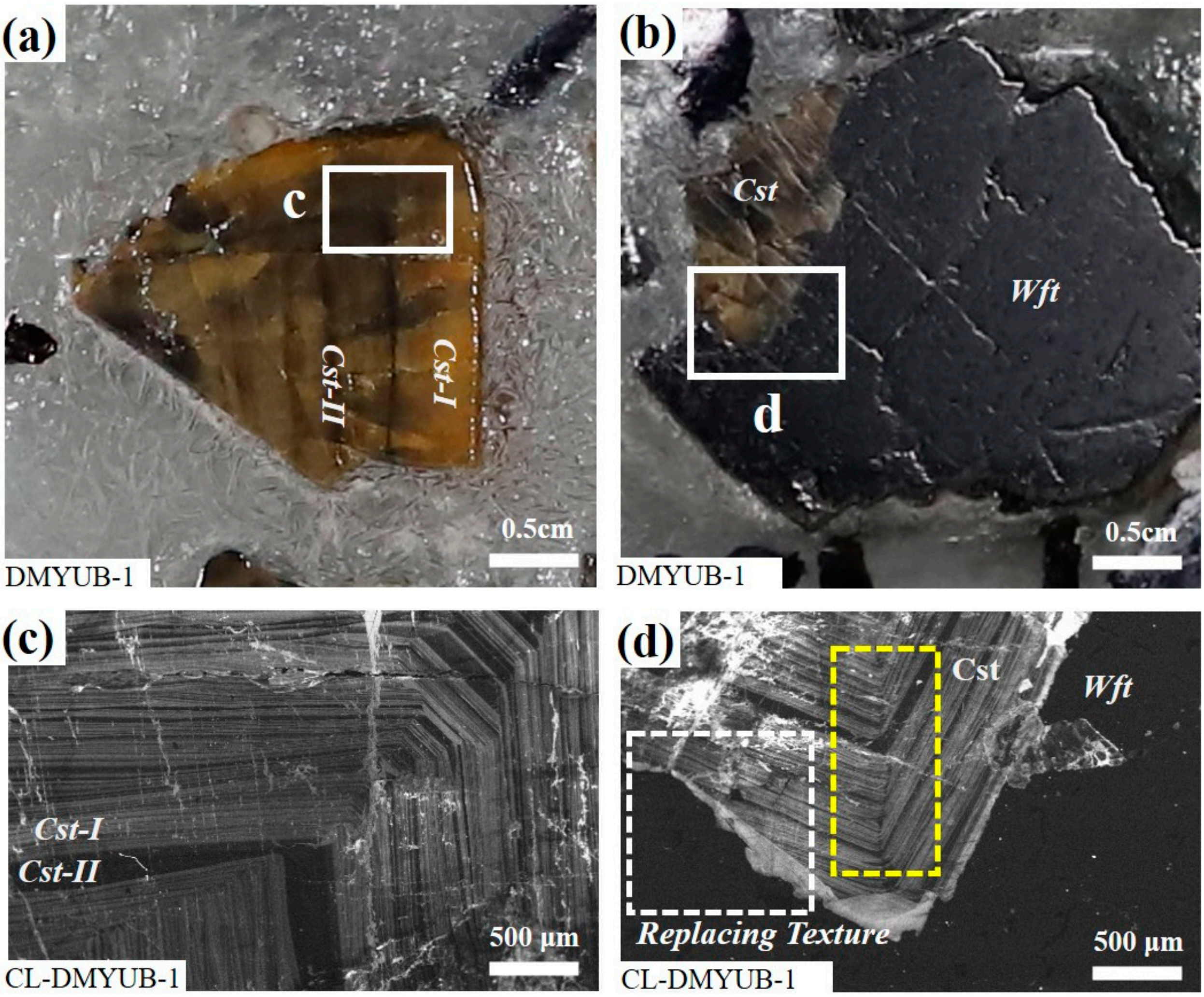

**Figure 6.** Representative photographs of KIB cassiterite and wolframite ore samples from Yubuli quartz veins [26,28]: (**a**,**b**) Macrophotographs of cassiterite and wolframite; (**c**,**d**) The corresponding views under SEM-CL for selected areas. The dotted white rectangle shows a replacement of cassiterite by wolframite (irregular boundary), and the dotted yellow rectangle shows a growth zone of alternating yellow transparent (a lighter CL) and dark translucent (a darker CL) cassiterite. (Legend: *Wft = wolframite*, *Cst I = yellow transparent cassiterite*, *Cst II = dark translucent cassiterite*).

**Table 3.** Summarized results of LA-ICP-MS and EPMA microanalyses (including all cross-sections) on cassiterite and wolframite concentrates from the KIB.

| **Summarized Data of LA ICP MS Analyses of Cassiterite and Wolframite** | | | | | | | | | | | | |
|---|---|---|---|---|---|---|---|---|---|---|---|---|
| Country: | Democratic Republic of Congo (DRC) | | | | | | | | | | | |
| Orogenic belt/Age: | Kibara belt (KIB)/Mesoproterozoic | | | | | | | | | | | |
| Rock type: | Granites and quartz veins | | | | | | | | Quartz veins | | | |
| Mineral: | Cassiterite | | | | | | | | Wolframite | | | |
| Ore texture: | Oscillatory and replacement | | | | | | | | Homogenous | | | |
| Ore type: | Type I (*n* = 68 spots) | | | | Type II (*n* = 40 spots) | | | | (*n* = 13 spots) | | | |
| Statistics: | Min. | Max. | Avg. | Std. | Min. | Max. | Avg. | Std. | Min. | Max. | Avg. | Std. |
| Major Oxides | | | | | | | | | | | | |
| $SO_2$ (wt.%) | 97.4 | 99.6 | 98.5 | 1.1 | 97.4 | 99.6 | 98.5 | 1.1 | t.e. | t.e. | t.e. | t.e. |
| $WO_3$ (wt.%) | t.e. | t.e. | t.e. | t.e. | t.e. | t.e. | t.e. | t.e. | 72.4 | 76.0 | 74.2 | 1.8 |
| FeOt (wt.%) | t.e. | t.e. | t.e. | t.e. | t.e. | t.e. | t.e. | t.e. | 16.7 | 18.5 | 17.6 | 0.9 |
| MnO (wt.%) | t.e. | t.e. | t.e. | t.e. | t.e. | t.e. | t.e. | t.e. | 5.9 | 6.9 | 6.4 | 0.5 |
| Total | 97.4 | 99.6 | 98.5 | 1.1 | 97.4 | 99.6 | 98.5 | 1.1 | 95.0 | 101.4 | 98.2 | 3.2 |
| Trace elements | | | | | | | | | | | | |
| Li (ppm) | 8.5 | 67.9 | 2.7 | 8.5 | 15.5 | 686.1 | 22.4 | 109.0 | 1.1 | 14.1 | 2.2 | 4.2 |

**Table 3.** *Cont.*

| **Summarized Data of LA ICP MS Analyses of Cassiterite and Wolframite** | | | | | | | | | | | | |
|---|---|---|---|---|---|---|---|---|---|---|---|---|
| Trace elements | | | | | | | | | | | | |
| Be (ppm) | bdl | bdl | bdl | bdl | 0.0 | 3.6 | 0.1 | 0.7 | 0.0 | 5.6 | 0.4 | 1.5 |
| B (ppm) | 6.5 | 19.1 | 11.7 | 3.7 | 6.5 | 16.3 | 12.2 | 2.0 | 0.9 | 8.8 | 2.1 | 3.3 |
| Na (ppm) | 9.9 | 94.2 | 9.9 | 16.7 | bdl | 88.1 | 17.3 | 21.9 | 0.5 | 224.7 | 29.9 | 61.5 |
| Mg (ppm) | 0.1 | 20.8 | 0.9 | 3.7 | bdl | 2123.6 | 64.2 | 331.4 | 1.1 | 280.6 | 96.4 | 106.6 |
| Al (ppm) | 1.5 | 487.8 | 51.3 | 109.9 | 5.5 | 2140.3 | 207.0 | 468.0 | 0.9 | 13.8 | 2.6 | 4.9 |
| Si (ppm) | 500.0 | 10,563.4 | 1432.1 | 1266.8 | 850.4 | 6105.8 | 1711.3 | 1223.9 | 108.0 | 1241.0 | 292.1 | 449.9 |
| P (ppm) | 3.8 | 242.4 | 6.7 | 30.1 | 5.1 | 65.5 | 9.8 | 17.2 | bdl | bdl | bdl | bdl |
| K (ppm) | 4.4 | 618.7 | 12.5 | 74.4 | 5.6 | 3636.0 | 160.3 | 655.0 | 1.1 | 38.4 | 4.6 | 11.3 |
| Ca (ppm) | 3.2 | 814.5 | 31.0 | 147.0 | 4.3 | 2233.7 | 73.0 | 356.9 | bdl | bdl | bdl | bdl |
| Sc (ppm) | 0.3 | 14.3 | 3.0 | 3.0 | 1.8 | 15.0 | 3.9 | 3.4 | 3.2 | 21.0 | 5.9 | 7.7 |
| Ti (ppm) | 238.4 | 3077.3 | 1037.5 | 833.4 | 65.7 | 2951.8 | 883.6 | 767.8 | 1.7 | 20.6 | 2.9 | 6.8 |
| V (ppm) | 10.2 | 91.6 | 14.4 | 15.6 | 5.4 | 88.1 | 12.0 | 17.0 | 0.0 | 1.2 | 0.1 | 0.3 |
| Cr (ppm) | 0.2 | 12.0 | 0.4 | 1.7 | 0.5 | 5.5 | 0.2 | 1.0 | bdl | bdl | bdl | bdl |
| Mn (ppm) | 103.8 | 4876.9 | 206.9 | 840.9 | 542.3 | 4692.9 | 281.5 | 979.6 | m.e. | m.e. | m.e. | m.e. |
| Fe (ppm) | 28.2 | 294.0 | 118.5 | 67.5 | 87.4 | 2565.9 | 444.6 | 439.7 | m.e. | m.e. | m.e. | m.e. |
| Co (ppm) | 8.5 | 15.8 | 13.3 | 2.5 | 11.9 | 15.5 | 13.7 | 0.9 | bdl | bdl | bdl | bdl |
| Ni (ppm) | 138.5 | 381.7 | 222.8 | 70.8 | 143.9 | 355.4 | 241.7 | 49.4 | bdl | bdl | bdl | bdl |
| Cu (ppm) | 0.4 | 3.4 | 0.2 | 0.7 | 1.1 | 8.8 | 1.8 | 2.3 | bdl | bdl | bdl | bdl |
| Zn (ppm) | 2.1 | 35.9 | 3.3 | 5.9 | 7.4 | 57.3 | 8.9 | 11.9 | 8.9 | 45.9 | 15.8 | 20.1 |
| Ga (ppm) | 1.8 | 33.2 | 2.3 | 7.0 | 2.0 | 37.4 | 2.9 | 7.1 | bdl | 0.5 | 0.0 | 0.1 |
| Ge (ppm) | bdl | bdl | bdl | bdl | 0.0 | 1.8 | 0.1 | 0.4 | bdl | bdl | bdl | bdl |
| As (ppm) | 1.9 | 30.2 | 2.3 | 4.9 | 8.7 | 63.6 | 11.9 | 15.1 | bdl | 2.5 | 0.2 | 0.7 |
| Rb (ppm) | 0.5 | 8.6 | 0.2 | 1.1 | 9.9 | 452.4 | 12.0 | 70.6 | bdl | 0.6 | 0.1 | 0.2 |
| Sr (ppm) | 0.1 | 6.9 | 0.5 | 0.9 | 0.0 | 2.0 | 0.5 | 0.6 | bdl | 2.3 | 0.6 | 0.7 |
| Y (ppm) | 0.0 | 1.6 | 0.1 | 0.3 | 0.5 | 20.0 | 1.0 | 3.3 | bdl | 9.3 | 2.9 | 2.8 |
| Zr (ppm) | 1.0 | 1324.5 | 137.1 | 283.4 | 2.1 | 1319.2 | 152.5 | 321.0 | bdl | 4.8 | 0.6 | 1.3 |
| Nb (ppm) | 720.2 | 9060.7 | 993.2 | 1551.9 | 425.3 | 7320.2 | 809.9 | 1621.1 | 12.0 | 365.1 | 133.7 | 94.5 |
| Mo (ppm) | 0.1 | 4.7 | 0.2 | 0.7 | bdl | bdl | bdl | bdl | bdl | bdl | bdl | bdl |
| Ag (ppm) | 0.0 | 1.7 | 0.1 | 0.3 | 0.0 | 2.7 | 0.1 | 0.5 | 1.1 | 6.9 | 1.3 | 2.0 |
| In (ppm) | 1.3 | 7.1 | 1.6 | 1.9 | 3.8 | 48.5 | 4.4 | 8.9 | 1.5 | 5.9 | 1.8 | 2.3 |
| Sn (ppm) | m.e. | m.e. | m.e. | m.e. | m.e. | m.e. | m.e. | m.e. | 2.1 | 26.5 | 2.6 | 7.1 |
| Sb (ppm) | 0.2 | 1.7 | 0.7 | 0.4 | 0.1 | 1.8 | 0.7 | 0.4 | bdl | bdl | bdl | bdl |
| Cs (ppm) | 0.1 | 2.9 | 0.6 | 0.5 | 1.8 | 73.4 | 2.5 | 11.4 | 0.1 | 2.2 | 0.3 | 0.6 |
| Ba (ppm) | 1.4 | 10.5 | 4.2 | 2.4 | 2.3 | 26.8 | 4.9 | 4.0 | 2.0 | 23.3 | 2.3 | 6.1 |
| La (ppm) | 0.1 | 0.6 | 0.1 | 0.1 | 0.3 | 1.6 | 0.1 | 0.3 | 0.5 | 3.8 | 0.4 | 1.0 |
| Ce (ppm) | 0.5 | 2.4 | 0.2 | 0.4 | 0.8 | 13.8 | 1.5 | 2.7 | 0.1 | 9.2 | 1.3 | 2.6 |
| Pr (ppm) | 0.0 | 0.3 | 0.1 | 0.1 | 0.0 | 0.6 | 0.1 | 0.1 | 0.1 | 1.4 | 0.2 | 0.4 |
| Nd (ppm) | 0.0 | 0.4 | 0.0 | 0.0 | 0.1 | 2.1 | 0.2 | 0.4 | 0.4 | 7.2 | 0.7 | 1.9 |
| Sm (ppm) | bdl | bdl | bdl | bdl | 0.1 | 0.5 | 0.2 | 0.1 | 0.1 | 3.0 | 0.3 | 0.8 |
| Eu (ppm) | 0.0 | 0.1 | 0.0 | 0.0 | 0.2 | 0.2 | 0.2 | 0.0 | 0.5 | 2.2 | 0.3 | 0.6 |
| Gd (ppm) | bdl | bdl | bdl | bdl | 0.3 | 1.0 | 0.5 | 0.2 | bdl | bdl | bdl | bdl |
| Tb (ppm) | bdl | bdl | bdl | bdl | 0.3 | 0.3 | 0.3 | 0.0 | 0.1 | 0.1 | 0.1 | 0.0 |
| Dy (ppm) | bdl | bdl | bdl | bdl | 2.0 | 2.3 | 0.1 | 0.4 | 2.2 | 4.2 | 2.7 | 1.1 |
| Ho (ppm) | 0.1 | 0.1 | 0.1 | 0.0 | 0.1 | 0.6 | 0.2 | 0.1 | 0.1 | 1.1 | 0.2 | 0.3 |
| Er (ppm) | 0.1 | 0.7 | 0.3 | 0.1 | 1.7 | 2.0 | 1.8 | 0.4 | 0.8 | 4.2 | 1.2 | 1.2 |
| Tm (ppm) | 0.0 | 0.3 | 0.1 | 0.1 | 0.1 | 0.3 | 0.2 | 0.1 | 0.3 | 1.9 | 0.4 | 0.5 |
| Yb (ppm) | 1.6 | 7.3 | 2.3 | 1.4 | 2.0 | 7.0 | 2.5 | 1.6 | 3.5 | 21.6 | 6.6 | 5.7 |
| Lu (ppm) | 0.5 | 1.5 | 0.8 | 0.3 | 1.2 | 1.6 | 1.3 | 0.3 | bdl | 2.4 | 1.1 | 0.7 |
| Hf (ppm) | 12.4 | 261.0 | 21.7 | 57.2 | 15.4 | 286.5 | 23.5 | 63.6 | bdl | bdl | bdl | bdl |
| Ta (ppm) | 0.1 | 35,161.3 | 1781.7 | 5941.2 | 1.0 | 34,131.8 | 3201.4 | 7741.0 | 1.0 | 8.6 | 2.8 | 2.6 |
| W (ppm) | 4.8 | 4503.6 | 299.1 | 776.3 | 0.9 | 3210.4 | 342.1 | 726.6 | m.e. | m.e. | m.e. | m.e. |
| Re (ppm) | 0.1 | 0.5 | 0.3 | 0.2 | bdl | bdl | bdl | bdl | 1.0 | 4.3 | 1.6 | 2.0 |
| Au (ppm) | 0.5 | 29.5 | 1.5 | 5.0 | 1.1 | 33.3 | 2.6 | 5.8 | 0.1 | 1.8 | 0.4 | 0.5 |
| Tl (ppm) | 0.0 | 0.9 | 0.5 | 0.1 | 0.0 | 2.5 | 0.1 | 0.4 | bdl | bdl | bdl | bdl |
| Pb (ppm) | 0.1 | 3.8 | 0.3 | 0.7 | 1.1 | 15.3 | 1.6 | 2.7 | 3.6 | 93.3 | 25.3 | 32.7 |
| Bi (ppm) | 0.1 | 102.8 | 1.7 | 12.4 | 0.2 | 13.3 | 1.8 | 2.9 | 2.0 | 48.9 | 8.9 | 13.7 |
| Th (ppm) | 0.1 | 0.5 | 0.3 | 0.1 | bdl | 0.9 | 0.1 | 0.2 | 0.1 | 0.1 | 0.1 | 0.0 |
| U (ppm) | 0.1 | 12.2 | 1.4 | 2.7 | 0.1 | 18.5 | 3.6 | 2.4 | 0.1 | 0.3 | 0.2 | 0.1 |

Notes: bdl = below the detection limit, m.e. = major element excluded, t.e. = trace element excluded.

FIs hosted in quartz, fluorite, and cassiterite exhibit various shapes, including circular, elongated, acicular, lenticular, tabular, polygonal, ameboid, and botryoidal (Figure 11a–m). A few primary FIAs occur along the growth zone of cassiterite (Figure 11a,h). Some FIs in quartz and cassiterite display "necking-down" features (Figure 11b,f), which were not included in this study.

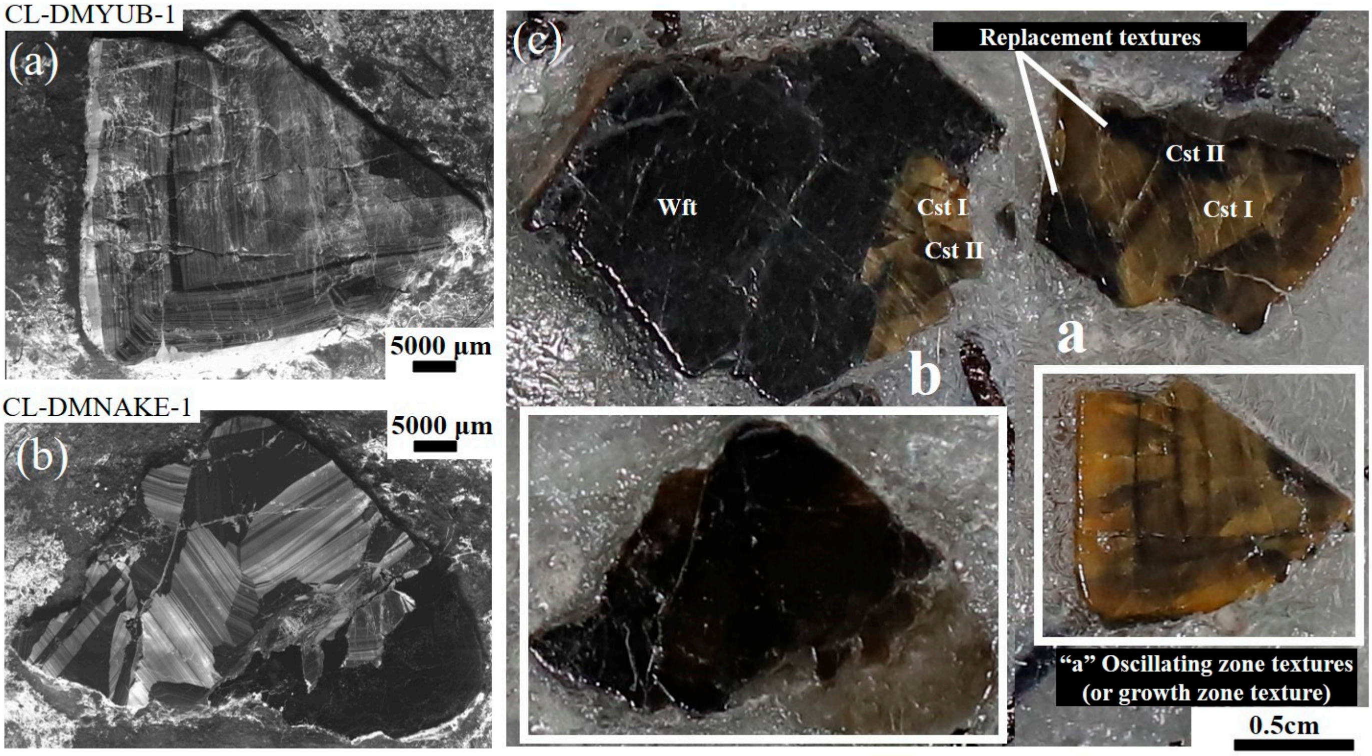

**Figure 7.** Representative photographs of KIB cassiterite and wolframite ore samples and textures: (**a**,**b**) CL-images of cassiterite from Yubuli quartz veins and Nakenge greisen, respectively, showing oscillating (or growth) zones and replacement textures; (**c**) The corresponding macrophotographs in white show selected rectangles of cassiterite (from Yubuli quartz vein and Nakenge greisen) and wolframite (from Nakenge quartz vein), showing oscillating (growth zone) and replacement textures. (Legend: *Wft = wolframite*, *Cst I = yellow transparent cassiterite*, *Cst II = dark translucent cassiterite*).

### *4.4. FI Microthermometry and Calculation of Fluid Density-Pressure-Paleodepths*

The fluid inclusion (FI) microthermometry was performed on liquid-rich inclusions hosted in quartz, cassiterite, and fluorite in the granites and the quartz veins (Figure 11a–m; Table 5). We report apparent salinity (wt.% NaCl equivalent), homogenization temperature (Th, °C), calculated apparent depths (primarily from boiling assemblages) (Figure 11j), pressure (bar), and density (g/cm$^3$) of the liquid-rich fluid inclusion assemblages (FIAs) (Figure 12a–d).

In the barren granites, FIAs hosted in quartz show a range of salinities from 3–23 wt.% and $T_h$ of 120–370 °C (averaging 280 °C). The Sn-bearing equigranular granites display a similar range of salinity (4–23 wt.%) but a somewhat broader range of $T_h$ (190–550 °C) (Figure 12a,b). Quartz-hosted FIAs of the Sn-W veins cutting metasedimentary rocks show a range of salinity (7–20 wt.%) and $T_h$ (170–350 °C). FIAs in the barren veins crosscutting the mineralized granites display a similar range of salinity (1–23 wt.%) but lower $T_h$ (130–270 °C) compared to the mineralized veins (Figure 12b,c). FIAs in the Sn-bearing greisenized granites exhibit salinity (11–19 wt.%) and $T_h$ (260–500 °C) (Figure 12b), and in the Sn-bearing pegmatites, a salinity range of 7–18 wt.% and $T_h$ of 180–330 °C (Figure 12b). In summary, quartz-hosted FIAs in the Sn-bearing granites show relatively higher $T_h$ (averaging 310 °C) compared to the barren granites (averaging 280 °C). Quartz-hosted FIAs in the Sn-W mineralized quartz veins in the metasedimentary rocks show relatively higher $T_h$ (averaging 260 °C) compared to the barren quartz veins (averaging 200 °C) in the mineralized granites (Figure 12b,c). FIAs in fluorite in the barren veins (Figure 12c) show salinities of 15–22 wt.% and lower $T_h$ (averaging 140 °C) compared to quartz (averaging 260 °C, Figure 12b,c) and cassiterite (averaging 270 °C, Figure 12a,b) hosted in the Sn-W mineralized veins.

In general, we observe a positive correlation between salinities and $T_h$ in the FIAs hosted in quartz and cassiterite in the Sn mineralized granites and the Sn-W mineralized veins (Figure 12a,b). No such positive correlation was observed between the Sn-W mineralized and barren veins (Figure 12c) and barren granites (Figure 12d). The range of salinities (7–20 wt.%) and $T_h$ (174–350 °C) is generally broader in quartz in the mineralized granites and mineralized veins compared to cassiterite (salinities of 2–10 wt.% and $T_h$ of 216–339 °C) in the same granites and veins. Salinities and $T_h$ are generally lower in cassiterite compared to quartz in the mineralized granites and veins.

Apparent depths were calculated by using pressures obtained from microthermometric measurements of the boiling assemblages hosted in the cassiterite and the quartz in the veins. Calculated pressures are 120–600 bars in the quartz and cassiterite, and apparent depths are calculated to be about 0.5–1 km (lithostatic pressure) and 1–2 km (hydrostatic pressure). Calculated pressures are higher in the granite compared to the veins. Apparent depths calculated from the FIAs of the mineralized granites are approximately 3–5 km (hydrostatic) and 2–3 km (lithostatic). FIAs hosted in fluorite in the barren veins show relatively higher densities (1.07–1.09) compared to the FIAs in the quartz hosted in the same veins (0.80–0.97).

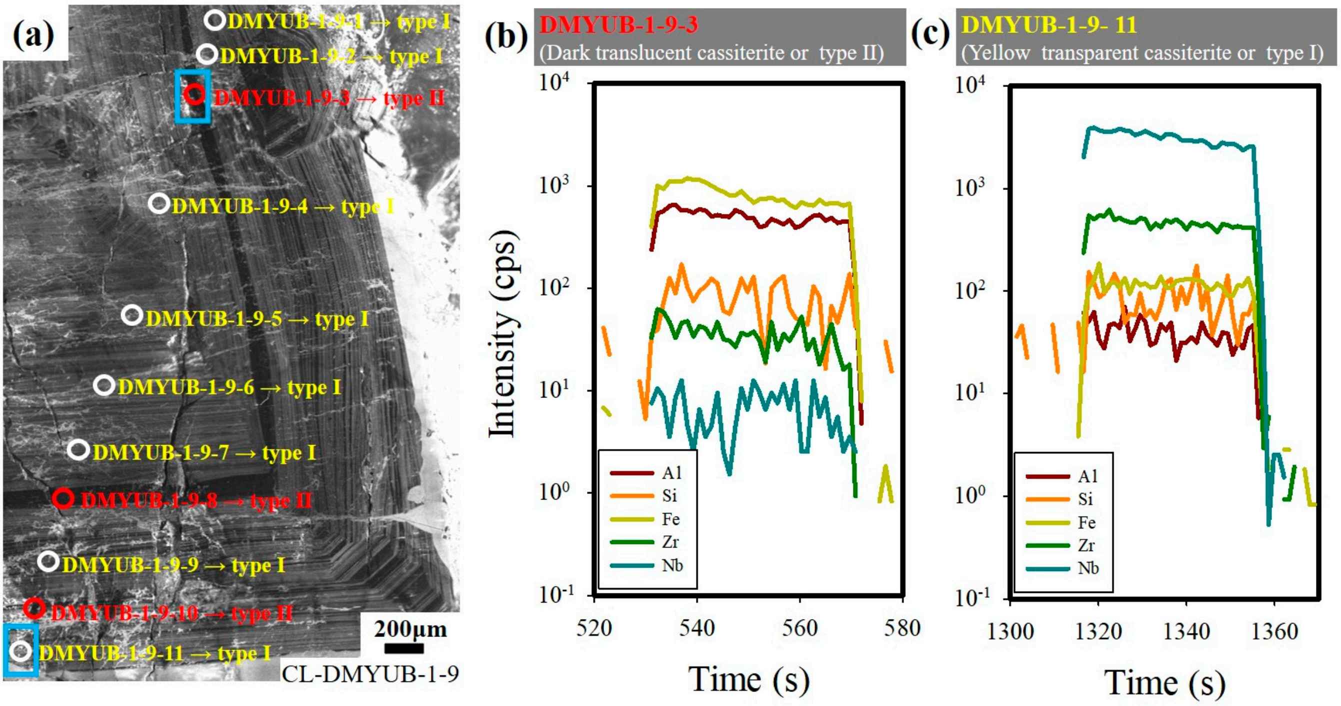

**Figure 8.** Cassiterite micro-zonation and LA-ICP-MS microanalysis: (**a**) A SEM-CL image showing a cross-section in cassiterite for subsequent LA-ICP-MS microanalysis; (**b**) A LA-ICP-MS transient signal showing a few detected trace elements (Fe-Al-Si-Zr-Nb) in dark translucent cassiterite (darker CL: Type II) from the Yubuli quartz vein; (**c**) A signal in yellow transparent cassiterite (lighter CL: Type I) from the Yubuli quartz vein. (Legend: *white circles are used for cassiterite type I, while red circles are for cassiterite type II; Blues squares are used for illustrated spots*).

### 4.5. Raman Spectroscopy on FIs

Raman spectroscopic analysis on bubble parts of the liquid- and vapor-rich inclusions was performed to identify gas species in the fluid inclusions (FIs). Quartz-hosted FIs in the mineralized granites and mineralized veins (Mokama and Nakenge, Figure 2) show the presence of $CH_4$, $CO_2$, $N_2$, and $H_2$ (Figure 13a,b). Cassiterite-hosted FIs contain species including $CH_4$, $CO_2$, $N_2$, and $H_2$ (Figure 13c).

The Raman intensity ratios of $CO_2/CH_4$, calculated from the relative maximum peak heights from the background for quartz-hosting inclusions, are 0.4–3.0 in the mineralized veins and 0.4–7.2 in the mineralized granites; 0.5–2.1 from cassiterite in the mineralized veins; and 0.7–1.0 from fluorite in the barren vein (Figure 13d). In general, the $CO_2/CH_4$ ratios in the quartz-hosted FIs in the mineralized granites are higher compared to the quartz and cassiterite-hosted FIs in the mineralized veins (Figure 13d).

## 5. Discussions

### *5.1. Ore Texture and Geochemistry*

Cassiterite displaying brighter (higher luminescence) and darker (lower luminescence) zones under SEM-CL can be caused by unequal distributions of trace elements [21,24] and crystallographic orientation [24]. The SEM-CL images of cassiterite grains in the KIB show micro-textures, including oscillatory (growth) zones and replacements. The yellow transparent cassiterite (type I: bright zone SEM-CL) formed earlier than the dark translucent cassiterite (type II: dark zone SEM-CL) [112]. Petrographic studies of cassiterite could not clearly elucidate the relationship between cassiterite zonation and trace element distributions [21,24,27,113–119], while a few studies showed that higher-Fe cassiterite induces lower luminescence compared to high-Ti cassiterite [24,28]. Dark translucent cassiterite (type II) hosts higher Fe-W-U contents than the light transparent cassiterite (type I), which is enriched in Nb-Ta-Ti [120], while wolframite is poor in Nb-Ta, reflecting that cassiterite forms at a relatively high temperature compared to cassiterite [121].

In the KIB cassiterite, the internal oscillatory texture of alternating type I and type II correlates with the distribution of some trace elements; Fe-Al-Ga-In-W are relatively enriched in type II, whereas Ti-V-Zr-Nb-Ta are enriched in type I (Figure 9a–d; Table 4). The KIB cassiterite contains traces including Fe, W, and V, representing a redox state; W, Ti, Al, In, and Ga are sensitive to hydrothermal temperature; and Ti, Nb, and Ta might indicate a fractionation process of causative magma [26]. Ratios of V/Fe and Ti/Fe being relatively lower in type II compared to type I can be interpreted as a change in hydrothermal redox state during alteration or fluid-fluid interactions. Ratios of In/Ta and Al/Nb are higher in cassiterite compared to those in wolframite, which can be interpreted as an earlier high-temperature precipitation of cassiterite compared to the later wolframite formation condition, which was relatively cooler.

The alteration may affect the mobility of trace elements such as Fe (redox-sensitive), In (high in high-temperature magmatic-like fluids), and Ga (high in low to moderate hydrothermal fluids) in hydrothermal fluids [19,38,122]. High Ti and V in cassiterite suggest relatively reducing hydrothermal conditions and high W suggests high-temperature fluids [6,21]. High Zr is generally associated with peralkaline granite systems, whereas high Ta is often associated with peraluminous pegmatites. High Al is associated with peraluminous granites [26,123]. Cassiterite from VMS deposits shows lower concentrations of Ta, Nb, and Zr compared to granite-related deposits [21].

Regarding ore chemistry, wolframite is relatively enriched in HREE (10–100 ppm) compared to cassiterite (0.1–10 ppm) (Figure 10a,b). Ce anomaly values in minerals indicate ore-forming conditions such as their redox state [117,124–131]. Cassiterites from the Nakenge and Mokama sites (the mineralized granites; Figure 2) show contrasting Ce anomaly values with cassiterite from the Yubuli site (the mineralized veins; Figure 2), suggesting relatively different redox state conditions at each site of the KIB during cassiterite and wolframite depositions (Figure 10a–d; Tables 3 and 4). The cassiterite ore textures displaying alternating cassiterite types (types I and II) correlate with an oscillatory behavior of selective trace elements (Figures 8b,c and 9a–d) and the fluctuation of Ce anomaly values and ratios of $CO_2/CH_4$. These results suggest fluid mixings of possibly reduced magmatic fluids with oxidized meteoric water during cassiterite precipitation, which will be discussed further with the following FIs results.

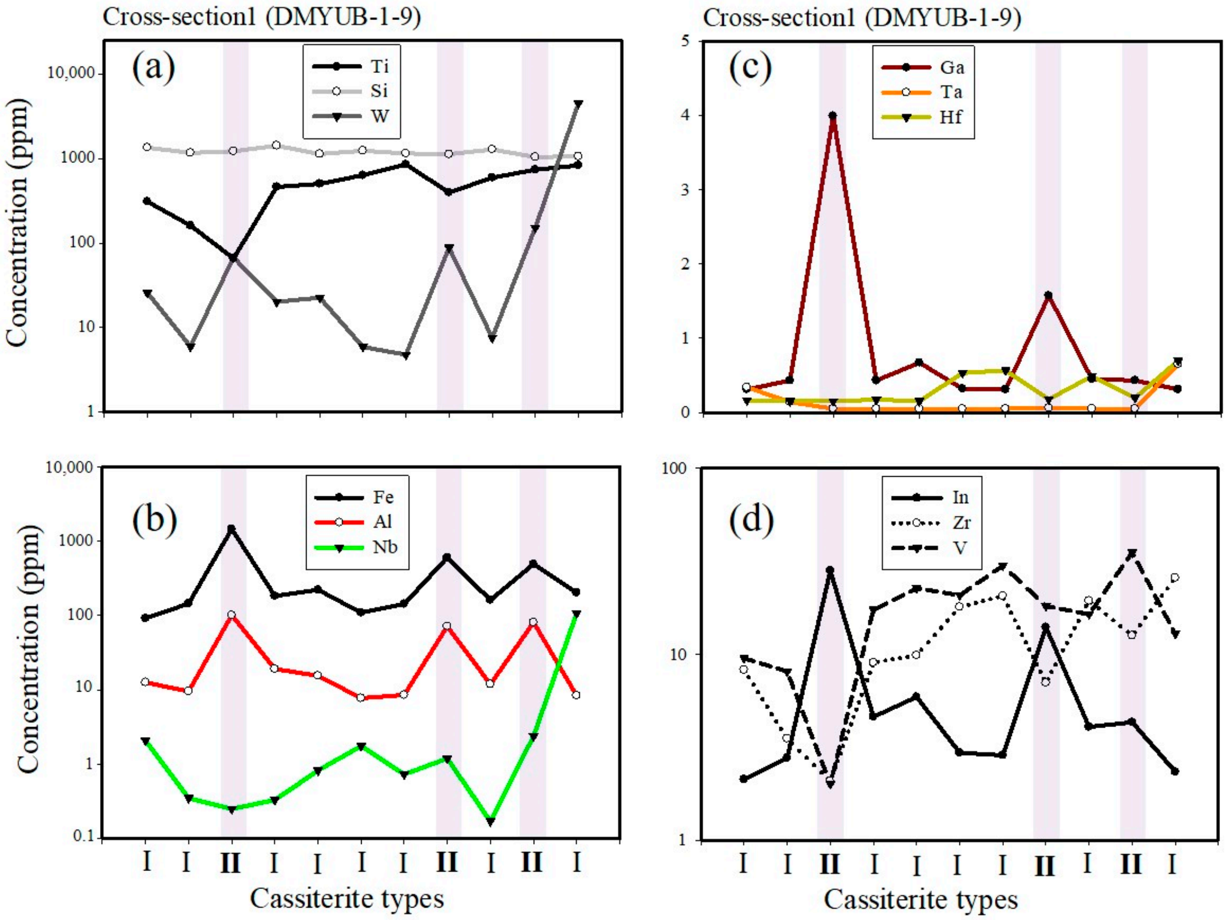

**Figure 9.** Trace element distributions and cassiterite types in the cross-section 1 of cassiterites from the Yubuli quartz veins. (**a**) Ti-Si-W concentrations versus CL; (**b**) Fe-Al-Nb concentrations; (**c**) Ga-Ta-Hf concentrations; and (**d**) In-Zr-V concentrations. (Legend: *II = Type II (darker CL) or dark translucent cassiterite, I = Type I (brighter CL) or yellow transparent cassiterite*).

**Table 4.** A summary of ore petrography and geochemistry.

| **Kibara Belt Cassiterite and Wolframite Summarized Textures, Trace Element Distributions, and Other Properties** | | | |
|---|---|---|---|
| Properties | Cassiterite | | Wolframite |
| | Cassiterite type I | Cassiterite type II | |
| Colors under naked eyes and microscope | Yellow transparent | Dark (to dark-reddish) translucent | Homogenous dark |
| Textures under microscope | Growth zone (oscillatory zoning), and replacement | Oscillatory zoning, replacement, and massive | Massive |
| Cathodoluminescence (CL) | Relatively higher luminescent (lighter) | Relatively low luminescent (darker) | Relatively low luminescent (darker) |
| Textures under CL | Growth zone (oscillatory zoning) | Oscillatory zoning and massive | Massive |
| Relative chronology | Earlier (old) | Later (young) | Very later (youngest) |
| Geochemistry (traces) | High Ti, V, Zr, Nb, Ta, Hf, and low Ce anomaly | High Fe, Al, Ga, In, As, U, Pb, Au, total REE, and high Ce anomaly | Al, Zn, Pb, Bi, Nb, high HREE |
| Mineral alteration evolution | Replaced by darker translucent cassiterite (type II) | Replaced by wolframite | No scheelite observed. |

### *5.2. Hydrothermal Alterations*

Alteration halos of muscovite-quartz (±topaz-fluorite-tourmaline) occurred in the Sn-bearing granites, while muscovite-quartz assemblages dominated along the Sn-W mineralized quartz veins. The alteration in barren granites (quartz-chlorite-muscovite-sericite) and quartz veins (hematite-pyrite) was not fully described in this study.

The hydrothermal alteration that affected mineralized granites and quartz veins contributed to metal remobilization and enrichments. The presence of muscovite in the mineralized granites in the KIB indicates an acidic condition favorable for W deposition [13,14,77,132,133]. In the mineralized quartz veins, the presence of muscovite indicates an acidic environment, and this mica is interpreted as a result of interactions between rising hydrothermal fluids and metasedimentary Al-rich host rocks, as shown in the reaction below [45,47,50]:

$$3Al_2Si_4O_{10}(OH)_2\ (s) + 2KCl\ (aq) + 2H_2O\ (aq) \rightarrow 2KAl_3Si_3O_{10}(OH)_2\ (s) + 6SiO_2\ (s) + 2HCl\ (aq) + H_2\ (gas)\ (\textbf{\textit{Rx. 1}}) \quad (1)$$

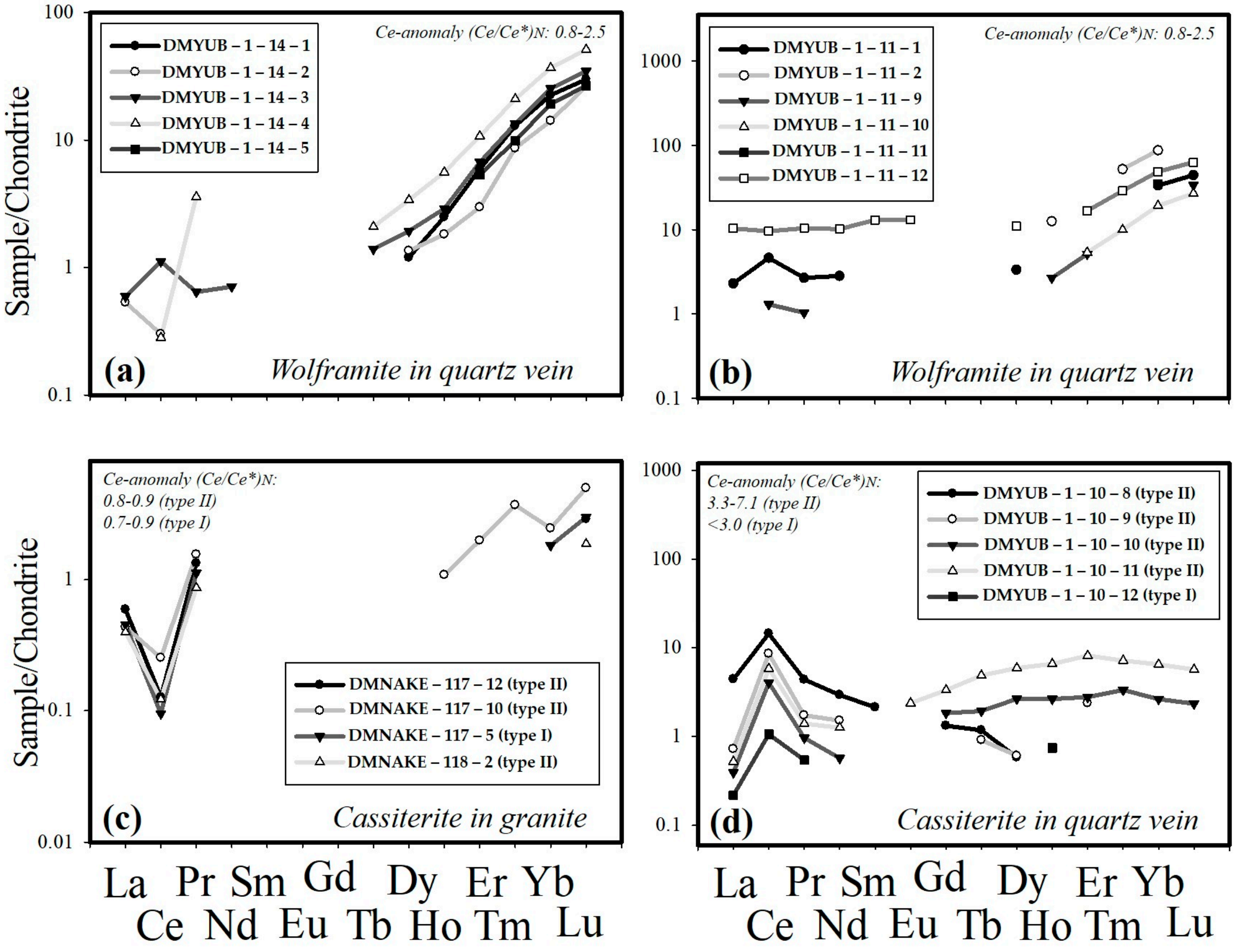

**Figure 10.** REE patterns in the Sn-W ore minerals. (**a**,**b**) Wolframite from the Yubuli quartz vein shows a relative HREE compared to cassiterite; (**c**) Cassiterite from the Nakenge greisenized granites shows a negative Ce anomaly (Chondrite normalized Ce/Ce* = 2Ce/(La + Pr)); (**d**) Cassiterite from the Yubuli quartz vein displays a positive Ce anomaly. REE values are normalized by chondrite [134,135].

In greisenized rocks, the presence of micas such as lepidolite in outer parts can be interpreted as a result of fluid-rock interactions that involve Li-rich fluids [47]:

$$\begin{aligned}&\mathrm{NaAlSi_3O_8}\ (s) + 2\mathrm{KF}\ (aq) + 2\mathrm{HF}\ (aq) + 2\mathrm{LiF}\ (aq) + 6\mathrm{HCl}\ (aq) + 6\mathrm{H_2O}\ (aq) \rightarrow \mathrm{KLi_2AlSi_4O_2(OH, F)_2}\ (s) + 10\mathrm{SiO_2}\\ &(s) + \mathrm{Al_2SiO_4(F, OH)_2}\ (s) + 2\mathrm{KAl_3Si_3O_{10}(F, OH)_2}\ (s) + 6\mathrm{NaCl}\ (aq) + 10\mathrm{H_2}\ (gas)\ (\boldsymbol{Rx.\ 2})\end{aligned} \tag{2}$$

These widespread fluid-rock interactions (hydrothermal alteration) in the KIB could remobilize metals into the hydrothermal fluids, which are essential for wolframite precipitation [14,102,103]. The possible remobilization of Fe and Mn from proximal metasedimentary country rocks suggests a lithological control of W mineralization in the veins of the KIB [5,45,49,66,79,80]. This highlights the importance of alteration in characterizing and exploring the Sn granites and the Sn-W quartz veins in the KIB [136].

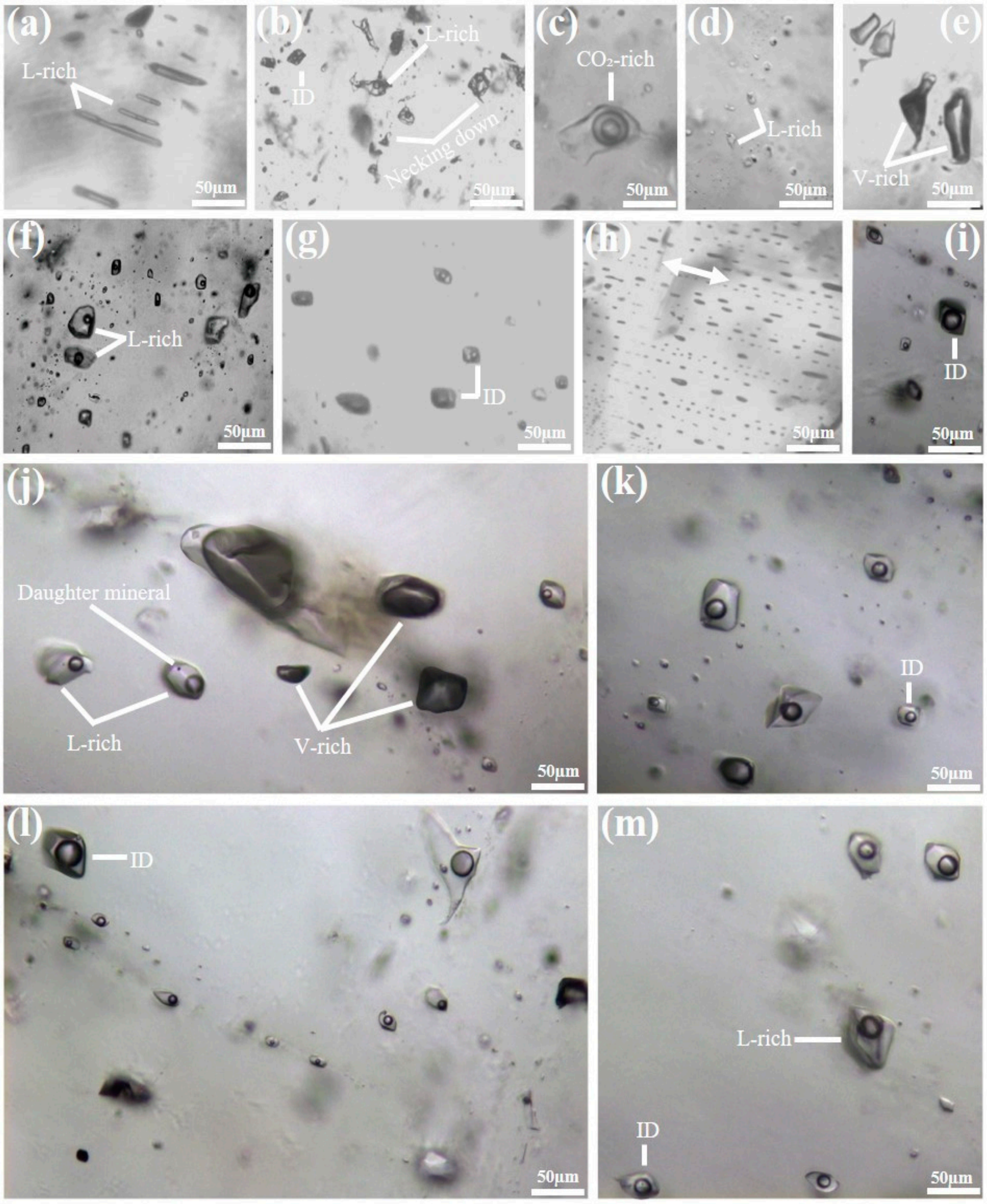

**Figure 11.** P Photomicrographs of representative fluid inclusions in the KIB [107]: (**a**) Primary aqueous liquid- and vapor-rich inclusions hosted in cassiterite from the Makunju site quartz veins;

(**b**) Pseudo-secondary aqueous, intermediate density (ID), liquid- and vapor-rich inclusions hosted in cassiterite from the Nakenge greisen; (**c**) Aqueous carbonic-bearing inclusions hosted in quartz in granite from the Mokama site; (**d**) Aqueous liquid-rich inclusions hosted in fluorite in the barren quartz veins from the Mokama site; (**e**) Vapor-rich inclusions hosted in quartz in the mineralized quartz veins from the Batamba site; (**f**) Pseudo-secondary aqueous liquid-rich dominant inclusions hosted in quartz in mineralized granite from the Mokama site; (**g**) Aqueous ID-type inclusions hosted in cassiterite in quartz veins from the Yubuli site; (**h**) Coexisting aqueous liquid- and vapor-rich inclusions hosted in cassiterite in mineralized quartz veins from the Makunju site, showing fluid inclusion trails aligned along the growth zone; (**i**) Aqueous ID, liquid-, and vapor-rich inclusions hosted in quartz in the mineralized veins from the Yubuli site; (**j**) Coexisting aqueous liquid- and vapor-rich inclusions (a boiling assemblage) hosted in quartz in the mineralized granite from the Mokama site; (**k**–**m**) Pseudo-secondary aqueous ID-type, liquid- and vapor-rich inclusions hosted in quartz in the granite from the Mokama site. Cassiterite hosts primary and pseudo-secondary fluid inclusions as well. Bubble sizes of most aqueous liquid-rich inclusions hosted in cassiterite and quartz are estimated to be 10–40 vol.%; bubble sizes of most aqueous liquid-rich inclusions hosted in fluorite are approximately 5–20 vol.%. The white arrow in (**h**) shows the growth zone direction. Few inclusions in cassiterite and quartz displayed necking-down features. (Legend: *L-rich = Liquid-rich inclusion, V-rich = Vapor-rich inclusion, ID = Intermediate Density inclusion where the aqueous and bubbles are relatively equivalent in volume*).

### *5.3. Fluid Inclusion Constraints*

The apparent paleo-depth calculated from the FIAs of the granites (3–5 km in hydrostatic pressure) is significantly lower than the values from geo-thermo-barometers using garnet-biotite and chlorite mineral pairs (9–15 km) from the same Sn-mineralized granites [51,77]. We do not know the reason for the discrepancy in depth estimations, but this could be partly due to disequilibrium in the mineral pairs used for geo-thermometry calculations.

FIs hosted in quartz contain the gas phases $CO_2$, $CH_4$, and rarely $N_2$, whereas FIs hosted in cassiterite contain $CO_2$, $CH_4$, $N_2$, and $H_2$ (Figure 13). Similar aged Sn-bearing granites in Rwanda contain aqueous inclusions with low to moderate salinities (6–15 wt% NaCl equiv.), $T_h$ of 240–320 °C, and calculated paleodepths of 3–4 km [66,79]. Detected gas species in the FIs are $CO_2$ (50–78 vol.%), $N_2$ (11–40 vol.%), and $CH_4$ (10–15 vol.%) [51,52,79], similar to the similar-aged KIB granites in this study.

Sn is transported as a chlorine complex in high-temperature magmatic-derived fluids [15]. Sn generally precipitates earlier in relatively high-temperature conditions, whereas W precipitates temporally later during cooling [6,97,137,138]. Hydrothermal geochemistry, including fluid inclusions and thermodynamic modeling, provides insights into magmatic-hydrothermal Sn-W formation [19,23,38,139–141]. Depressurization of magmatic-hydrothermal fluid, which causes phase separation and increases the fluid's pH, as well as mixing of magmatic-derived fluids with meteoric water, which could increase $fO_2$ and decrease the temperature of the fluid, could enhance the massive precipitation of wolframite [142–147]. The solubility of W in a hydrothermal fluid is favorable under variable oxygen fugacity [148,149] and acidic pH [45,49,145,150–152].

It has been demonstrated that fluid-rock interactions [15] and the mixing of fluids between magmatic and meteoric waters [16] are the major Sn-forming processes. The KIB FIAs results, showing variable and wide ranges of $T_h$ and apparent salinities, can be evidence of fluid mixing [15,16,40,153–158]. High $T_h$ (190–550 °C) in the Sn-bearing granites suggests that cassiterite precipitation was driven by magmatic-dominant fluids, while Sn-W bearing quartz veins show a wider and lower $T_h$ (130–350 °C), suggesting a mixing between magmatic and cooler water [159]. These could play a selective role in the precipitation of early Sn (>200 °C in granite-related Sn deposits) and later Sn-W (>160 °C in Sn-W quartz vein) (Figure 12a,b).

FIs hosted in cassiterite contain $CO_2$, $CH_4$, $N_2$, and $H_2$ (Figure 13a–c). These Raman results, which show an abundance of $CO_2$ and $CH_4$, indicate that mineralizing fluids have either magmatic origins or mixed sources of magmatic and meteoric origins since the Sn-W mineralization system is associated with Kibaran post-orogenic magmatism. The potential source of the $N_2$ detected in the KIB cassiterite-hosted FIs could be meteoric water or metamorphic-derived fluids, with a few studies of stable isotopes (O and H) on quartz from granite and quartz veins reporting fluids of metamorphic origin [14]. $N_2$, together with $CO_2$ or $CH_4$ in the fluids, could be derived from organic C-bearing (meta-)sedimentary rocks [96] or magmatic fluids of $CO_2$-$CH_4$ mixed with $N_2$-rich meteoric water.

The $CO_2/CH_4$ ratios, calculated from the Raman peak heights in FIs hosted in quartz from mineralized granites, are relatively higher compared to those in quartz and cassiterite hosted in mineralized quartz veins. As $CO_2/CH_4$ ratios represent relative redox states, the fluctuations of the ratios might indicate changing redox states in the Sn-W-forming hydrothermal fluids (Figure 13d) [128,160–162]. This result is consistent with the changing Ce anomaly values in cassiterite (Figure 10c,d).

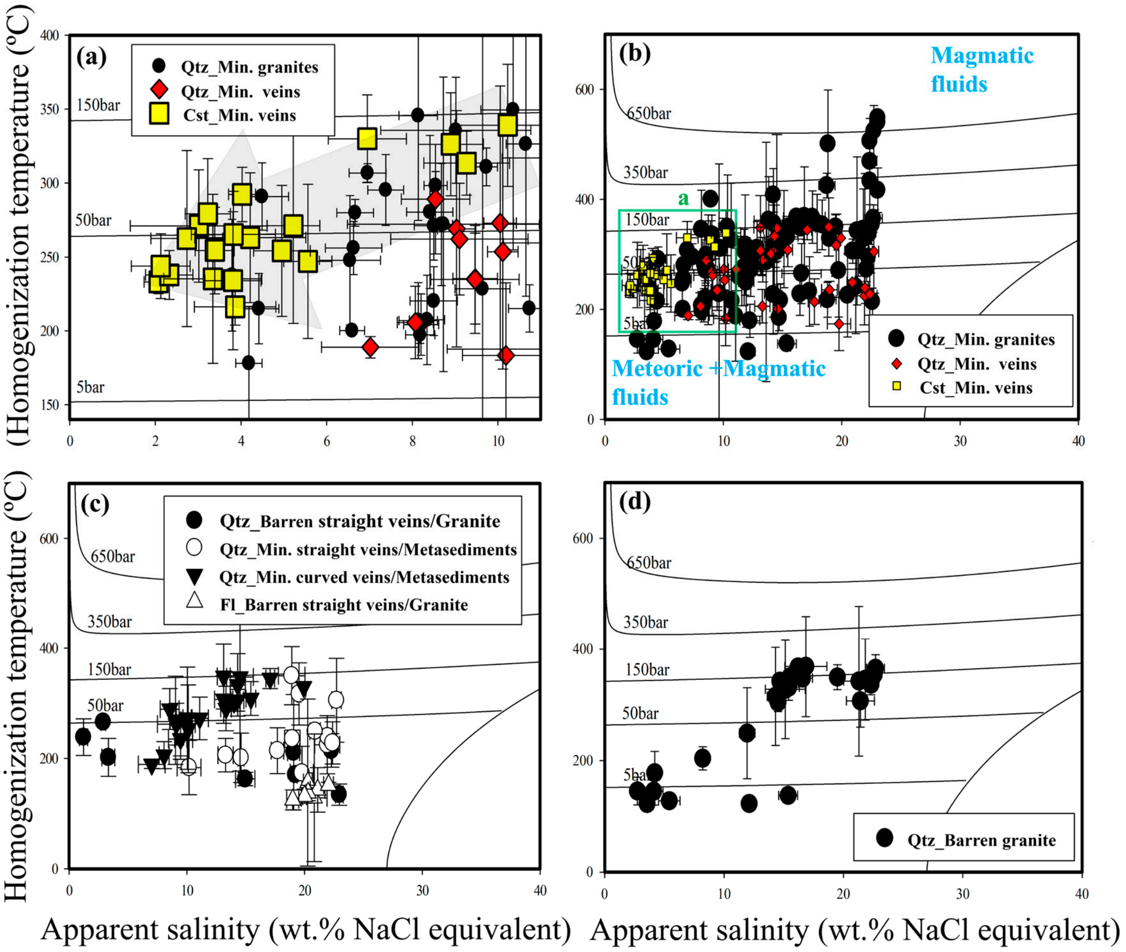

**Figure 12.** Microthermometric results of the KIB FIAs: (**a**,**b**) Apparent salinities and homogenization temperatures measured from FIAs hosted in cassiterite and quartz in the veins and the granites. The gray arrow in (**a**) is a hypothetical trend of magmatic fluids mixing with low-T and low-saline water; (**c**) Salinities and homogenization temperatures in FIAs hosted in fluorite and quartz from straight and curved veins crosscutting metasediments and granites; (**d**) Salinities and homogenization temperatures in FIAs hosted in quartz from the barren granites. The isobaric curves and salinities were obtained using an $H_2O$-NaCl system [108,159,163]. Results are reported as averages and standard deviations (Avg ± 1σ), calculated from about 3–5 separately measured single inclusions within each FIAs [32,106,107].

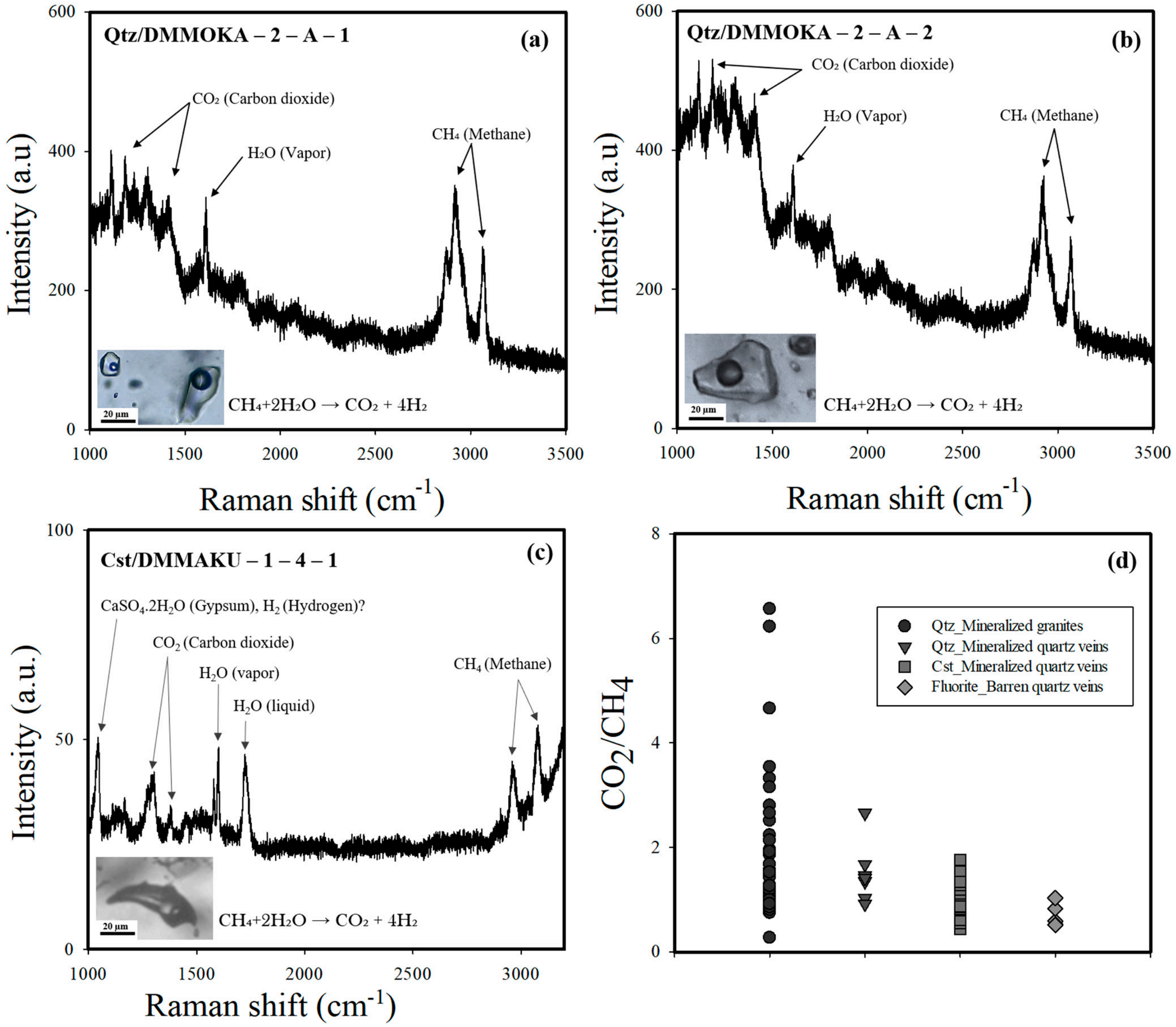

**Figure 13.** Laser Raman spectroscopy on bubble parts of the FIs: (**a**,**b**) FIs hosted in quartz in mineralized granites from the Mokama site; (**c**) FIs hosted in cassiterite in mineralized quartz veins from the Makunju site; (**d**) Ratios of $CO_2/CH_4$ calculated from Raman peak height intensities of gas species in the FIs are compared between quartz hosted in the mineralized granites, quartz and cassiterite hosted in the mineralized quartz veins, and fluorite hosted in the barren quartz veins.

### 5.4. Sn-W Precipitation Processes

Here, we discuss the geochemical conditions and reactions required for Sn-W transportation and precipitation, which can be strongly controlled by (1) pH, (2) oxygen fugacity, and (3) temperature (or pressure).

*Sn precipitation reaction*: $Sn\ (II)Cl_2\ (aq) + 2H_2O\ (aq) \leftrightarrow Sn\ (IV)O_2 + 2HCl\ (aq) + H_2\ (gas)$ (***Rx. 3***). (3)

The precipitation of cassiterite [15] requires (1) oxidation, (2) increasing pH, and (3) cooling. The redox change during the cassiterite precipitation in the KIB can be reflected by its (a) Ce-anomaly value fluctuations in the micro-textured cassiterites (Figure 10c,d), (b) variation of the $CO_2/CH_4$ ratios in the FIs (Figure 13d), and (c) large variations and positive correlations of $T_h$ and salinities in the FIAs (Figure 12a–d). The shifting of the valence state of Sn from +2 in fluids to +4 in cassiterite is required. These geochemical and FIs features strongly suggest a redox fluctuation in the Sn-forming hydrothermal fluids in the KIB (Figures 10c,d and 14e) [128,129,160,164]. The redox variation can be influenced by fluid mixing between hot, high saline magmatic water and cooler, low saline meteoric water. This fluid-fluid mixing and interaction process could cool as well as oxidize the Sn-bearing magmatic-derived fluids to promote selective cassiterite precipitation [16,19], forming high-grade Sn in the KIB.

*W precipitation reaction*: $H_2WO_4\ (aq) + Fe\ (or\ Mn)\ Cl_2\ (aq) \leftrightarrow Fe\ (or\ Mn)\ WO_4\ (s) + 2HCl\ (aq)$ (***Rx. 4***). (4)

The precipitation of wolframite requires (1) fluid cooling, (2) a pH increase, and (3) the presence of Fe (or Mn) in the fluids [32]. Fluid cooling and pH increase can be achieved with fluid mixing and feldspar-destructive hydrothermal alteration (e.g., muscovite). Since no wolframite precipitation is observed in the quartz vein hosted in the granite, the magmatic-derived fluid in the KIB might be poor in terms of its Fe or Mn contents. Potential remobilization of $FeCl_2$ and $MnCl_2$ from host metasedimentary rocks is required [14,102], which might explain the selective wolframite precipitation in the quartz veins hosted in the metasedimentary rocks.

## 6. Conclusions

Important findings from the Sn granite and the Sn-W quartz vein from the KIB are summarized as follows: (1) Micro-textures of cassiterite, selective trace element distributions, including Ce anomaly values, variable $CO_2/CH_4$ ratios in the fluid inclusions, and wide ranges and positively correlating salinities and $T_h$ strongly suggest mixing of fluids between magmatic-derived (reduced, hot, and high saline) and meteoric (cooler and low saline) water during cassiterite precipitation in the granite and the quartz veins in the KIB. (2) Alteration of the rock (greisenization) and ore mineral (replacement textures) consistently supports the idea of massive precipitation of the high-grade cassiterite ores that require hydrothermal alteration and mixing of fluids. (3) Wolframite precipitated in the quartz veins hosted in the metasedimentary rocks might be promoted by the remobilization of Fe or Mn through pervasive alteration reactions. The occurrences of alteration and fluid mixing may be key geological processes that form high-grade cassiterite and wolframite in the KIB granites and quartz veins.

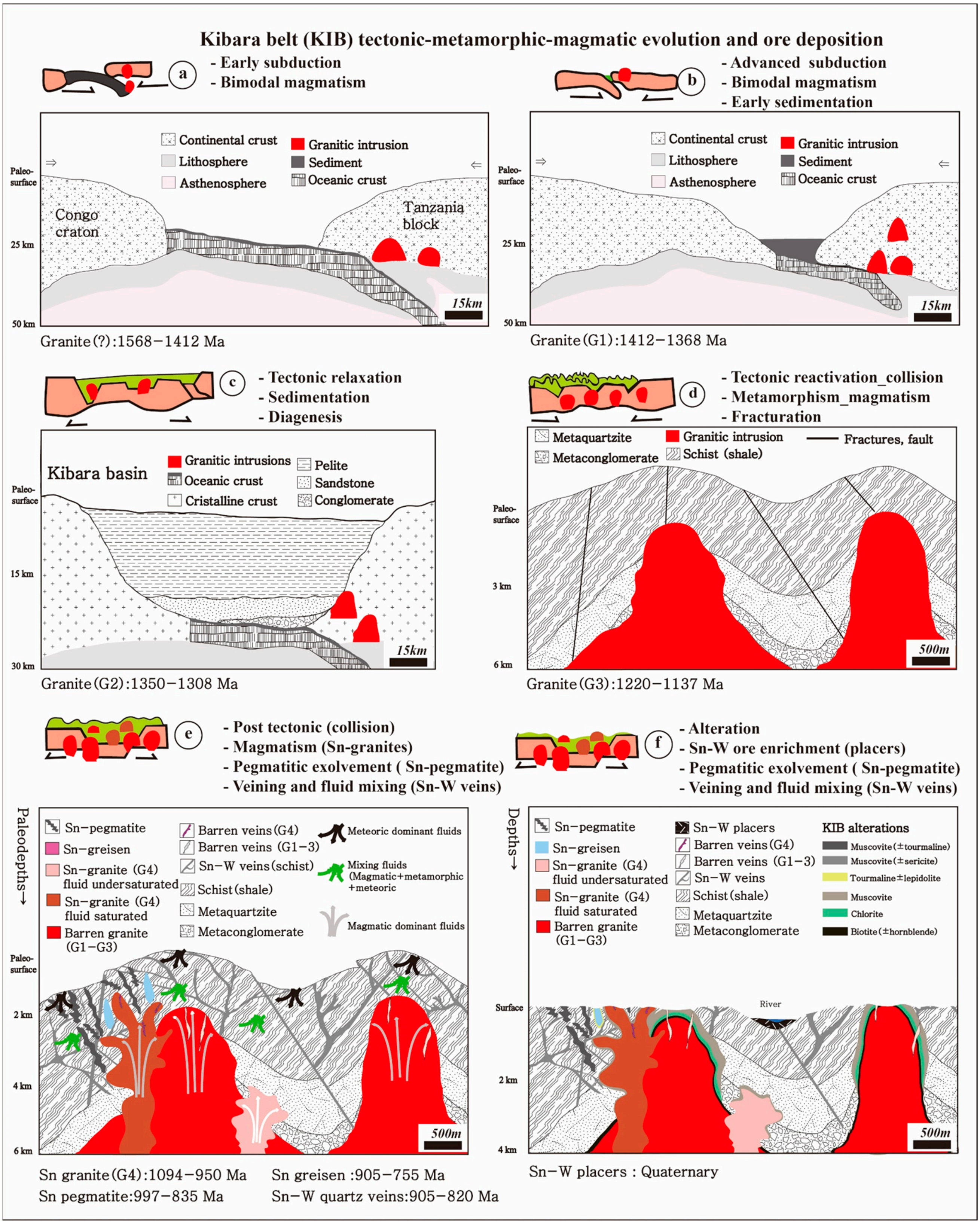

**Figure 14.** Tectono-magmatic and geochemically reconstructed model of the KIB Sn granites and Sn-W quartz veins: (**a**–**d**) Sketches illustrating the evolution from subduction towards sedimentation, regional metamorphism, syn-tectonic magmatism, and fracturation and collision; (**e**,**f**) Sketches depicting the evolution of veining, post-tectonic (post-collision) magmatism, fluid mixing, alteration, ore deposition, and finally mechanical weathering.

**Table 5.** Microthermometric data of fluid inclusion assemblages (FIAs) hosted in quartz, cassiterite, and fluorite in mineralized and barren granites and mineralized and barren quartz veins from the Kibara belt (KIB) in the DRC.

| FIAs | Host/Rock | Type | Bubble | Tm_Avg. | Tm_Std. | S_Avg. | S_Std. | Th_Avg. | Th_Std. | P_Avg. | P_Std. | Density |
|---|---|---|---|---|---|---|---|---|---|---|---|---|
| | | | *Vol.%* | *Degree* (°C) | | *Wt.% NaCl equiv.* | | *Degree* (°C) | | *Bar* | | g/cm$^3$ |
| DMMOKA-2-A-1 | Qz/M. granite | L-rich | 30 | −8.8 | 0.0 | 12.6 | 0.0 | 293.2 | 0.0 | 72.4 | 0.0 | 0.8577 |
| DMMOKA-2-A-2 | Qz/M. granite | ID | 40 | −9.9 | 0.6 | 13.8 | 0.6 | 362.1 | 15.9 | 173.2 | 13.0 | 0.7666 |
| DMMOKA-2-A-5 | Qz/M. granite | L-rich | 30 | −10.3 | 0.2 | 14.2 | 0.3 | 408.2 | 9.5 | 280.1 | 35.6 | 0.6929 |
| DMMOKA-2-B-1 | Qz/M. granite | L-rich | 20 | −5.2 | 0.1 | 8.2 | 0.2 | 197.4 | 1.2 | 13.9 | 0.9 | 0.9320 |
| DMMOKA-2-B-4 | Qz/M. granite | L-rich | 30 | −7.5 | 0.9 | 11.0 | 1.1 | 187.8 | 16.4 | 11.0 | 2.9 | 0.9646 |
| DMMOKA-2-C-1 | Qz/M. granite | L-rich | 30 | −5.5 | 0.2 | 8.5 | 0.3 | 220.2 | 4.7 | 22.0 | 0.6 | 0.9111 |
| DMMOKA-2-C-4 | Qz/M. granite | ID | 40 | −5.5 | 0.1 | 8.5 | 0.1 | 298.3 | 1.9 | 80.0 | 0.5 | 0.8106 |
| DMMOKA-2-C-6 | Qz/M. granite | L-rich | 30 | −9.7 | 0.2 | 13.6 | 0.2 | 286.3 | 43.5 | 65.0 | 5.0 | 0.8762 |
| DMMOKA-2-7-1-1 | Qz/B. vein | L-rich | 30 | −2.0 | 0.2 | 3.3 | 0.3 | 201.8 | 6.8 | 15.8 | 0.7 | 0.8899 |
| DMMOKA-2-7-3-1 | Qz/B. vein | L-rich | 20 | −1.7 | 0.0 | 2.9 | 0.0 | 265.8 | 0.0 | 50.7 | 2.9 | 0.8036 |
| DMMOGA-1-1-1 | Qz/M. peg. | L-rich | 20 | −6.3 | 0.2 | 9.6 | 0.3 | 228.5 | 47.2 | 25.6 | 14.5 | 0.9106 |
| DMMOGA-1-1-4 | Qz/M. peg. | L-rich | 20 | −7.1 | 0.2 | 10.7 | 0.2 | 326.5 | 20.6 | 115.6 | 27.9 | 0.7883 |
| DMMOGA-1-1-6 | Qz/M. peg. | L-rich | 20 | −8.5 | 1.7 | 12.2 | 2.0 | 179.3 | 6.0 | 9.0 | 0.3 | 0.9817 |
| DMMOKA-2-8-2-1 | Fl/B. vein | L-rich | 30 | −17.8 | 1.1 | 20.8 | 0.8 | 128.6 | 23.1 | 2.2 | 0.5 | 1.0900 |
| DMMOKA-2-8-2-6 | Fl/B. vein | L-rich | 30 | −17.1 | 0.2 | 20.3 | 0.2 | 156.4 | 30.3 | 4.7 | 0.8 | 1.0650 |
| DMMOKA-2-8-2-9 | Fl/B. vein | L-rich | 20 | −18.2 | 0.7 | 21.1 | 0.5 | 142.9 | 8.0 | 3.2 | 0.3 | 1.0820 |
| DMMOKA-2-8-6-1 | Fl/B. vein | L-rich | 20 | −17.1 | 0.1 | 20.3 | 0.1 | 137.4 | 2.8 | 2.8 | 0.1 | 1.0790 |
| DMMOKA-2-8-6-2 | Fl/B. vein | L-rich | 20 | −16.7 | 0.1 | 20.0 | 0.1 | 131.5 | 2.6 | 2.4 | 0.2 | 1.0810 |
| DMMOKA-2-8-6-4 | Fl/B. vein | L-rich | 20 | −15.4 | 0.3 | 19.0 | 0.3 | 124.9 | 3.6 | 2.0 | 0.5 | 1.0780 |
| DMMOKA-2-8-6-8 | Fl/B. vein | L-rich | 20 | −19.5 | 0.3 | 22.0 | 0.2 | 151.4 | 1.1 | 4.0 | 0.8 | 1.0830 |
| DMMOKA-2-8-4-1 | Qz/B. vein | L-rich | 30 | −15.7 | 0.1 | 19.2 | 0.1 | 170.7 | 1.3 | 6.8 | 0.1 | 1.0440 |
| DMMOKA-2-8-4-3 | Qz/B. vein | L-rich | 30 | −11.0 | 0.7 | 15.0 | 0.7 | 162.7 | 2.5 | 5.9 | 0.1 | 1.0170 |
| DMMOKA-2-8-4-5 | Qz/B. vein | L-rich | 10 | −20.9 | 0.3 | 22.9 | 0.2 | 134.4 | 3.8 | 2.5 | 0.2 | 1.1040 |
| DMMOKA-2-8-4-7 | Qz/B. vein | L-rich | 30 | −19.9 | 0.0 | 22.3 | 0.0 | 214.5 | 6.1 | 17.4 | 0.3 | 1.0320 |
| DMMOKA-2-8-4-9 | Qz/B. vein | L-rich | 30 | −15.5 | 0.7 | 19.1 | 0.6 | 211.1 | 20.9 | 16.8 | 1.1 | 1.0070 |
| DMMOKA-2-6-1-1 | Qz/M. granite | L-rich | 20 | −16.4 | 0.3 | 19.7 | 0.2 | 270.4 | 16.8 | 48.4 | 0.8 | 0.9519 |
| DMMOKA-2-6-1-2 | Qz/M. granite | L-rich | 30 | −19.6 | 0.3 | 22.1 | 0.2 | 273.1 | 4.4 | 49.4 | 1.7 | 0.9704 |
| DMMOKA-2-6-2-1 | Qz/M. granite | ID | 40 | −8.1 | 0.7 | 11.8 | 0.9 | 317.1 | 18.2 | 101.4 | 12.4 | 0.8156 |
| DMMOKA-2-6-2-4 | Qz/M. granite | ID | 40 | −10.3 | 0.6 | 14.2 | 0.6 | 302.4 | 23.3 | 81.6 | 8.4 | 0.8610 |
| DMMOKA-2-6-2-6 | Qz/M. granite | ID | 40 | −2.3 | 0.0 | 3.8 | 0.1 | 237.7 | 7.6 | 31.4 | 5.6 | 0.8512 |
| DMYUB-1-6-1 | Qz/M. vein | L-rich | 30 | −9.4 | 0.3 | 13.3 | 0.3 | 205.9 | 6.1 | 16.0 | 3.7 | 0.9645 |
| DMYUB-1-6-4 | Qz/M. vein | L-rich | 20 | −6.8 | 0.6 | 10.2 | 0.7 | 183.4 | 9.8 | 10.1 | 4.9 | 0.9620 |
| DMYUB-1-4-1 | Qz/M. vein | L-rich | 30 | −19.4 | 0.8 | 21.9 | 0.5 | 224.7 | 10.5 | 21.3 | 2.5 | 1.0190 |
| DMNAKE-1-3-1 | Qz/M. greisen | ID | 40 | −9.3 | 0.3 | 13.1 | 0.3 | 348.4 | 11.8 | 148.8 | 15.8 | 0.7815 |
| DMNAKE-1-3-2 | Qz/M. greisen | L-rich | 20 | −5.9 | 0.2 | 9.0 | 0.2 | 269.0 | 16.0 | 51.4 | 3.7 | 0.8569 |
| DMNAKE-1-5-1 | Qz/M. greisen | L-rich | 30 | −5.9 | 0.6 | 9.1 | 0.8 | 262.1 | 7.6 | 46.1 | 4.0 | 0.8659 |
| DMBALE-1-1-1 | Qz/B. granite | ID | 40 | −11.6 | 0.4 | 15.5 | 0.3 | 349.9 | 0.3 | 148.6 | 16.4 | 0.8059 |
| DMBALE-1-1-2 | Qz/B. granite | ID | 40 | −13.0 | 1.0 | 16.8 | 0.9 | 368.9 | 18.0 | 181.7 | 18.2 | 0.7915 |
| DMBALE-1-4-1 | Qz/B. granite | L-rich | 20 | −11.2 | 0.8 | 15.1 | 0.8 | 327.9 | 17.7 | 113.9 | 13.1 | 0.8345 |
| DMBALE-1-4-5 | Qz/B. granite | L-rich | 20 | −10.4 | 0.3 | 14.3 | 0.3 | 315.3 | 17.6 | 97.2 | 7.6 | 0.8442 |
| DMMOKA-2-4-3-1 | Qz/M. granite | L-rich | 30 | −10.8 | 0.1 | 14.7 | 0.0 | 185.3 | 4.8 | 10.1 | 0.8 | 0.9959 |
| DMMOKA-2-4-3-2 | Qz/M. granite | L-rich | 20 | −10.3 | 0.3 | 14.2 | 0.4 | 227.2 | 14.5 | 24.1 | 1.8 | 0.9508 |
| DMMOKA-2-4-3-3 | Qz/M. granite | L-rich | 10 | −19.8 | 0.4 | 22.2 | 0.3 | 295.2 | 5.0 | 68.8 | 6.9 | 0.9465 |
| DMMOKA-2-4-3-5 | Qz/M. granite | L-rich | 30 | −12.5 | 0.2 | 16.5 | 0.2 | 228.0 | 7.7 | 24.0 | 3.4 | 0.9683 |
| DMMOKA-2-4-3-10 | Qz/M. granite | L-rich | 20 | −4.4 | 0.2 | 7.0 | 0.2 | 306.9 | 1.3 | 91.1 | 10.2 | 0.7814 |
| DMMOKA-2-4-3-14 | Qz/M. granite | L-rich | 30 | −20.0 | 0.1 | 22.4 | 0.1 | 433.3 | 12.5 | 329.3 | 34.5 | 0.7654 |
| DMMOKA-2-4-3-16 | Qz/M. granite | L-rich | 10 | −4.1 | 0.2 | 6.6 | 0.3 | 256.1 | 3.6 | 42.4 | 8.9 | 0.8514 |
| DMMOKA-2-4-3-21 | Qz/M. granite | L-rich | 30 | −4.2 | 0.2 | 6.7 | 0.2 | 279.9 | 1.8 | 61.8 | 11.1 | 0.8200 |
| DMMOKA-2-7-7-1 | Qz/B. vein | L-rich | 20 | −0.7 | 0.1 | 1.2 | 0.2 | 238.5 | 6.6 | 32.4 | 3.2 | 0.8268 |
| DMMOKA-2-7-7-3 | Qz/M. granite | L-rich | 20 | −12.7 | 0.9 | 16.6 | 0.8 | 265.2 | 10.9 | 45.8 | 6.1 | 0.9294 |
| DMMOKA-2-2-5-1 | Qz/M. granite | ID | 50 | −20.5 | 0.3 | 22.7 | 0.2 | 524.2 | 9.3 | 651.6 | 48.6 | 0.6872 |
| DMMOKA-2-2-5-3 | Qz/M. granite | ID | 40 | −20.0 | 0.2 | 22.4 | 0.1 | 506.0 | 2.8 | 587.2 | 39.1 | 0.6964 |
| DMMOKA-2-2-1-1 | Qz/M. granite | L-rich | 30 | −21.0 | 0.0 | 23.1 | 0.0 | 416.6 | 8.1 | 280.2 | 22.1 | 0.7953 |
| DMMOKA-2-2-1-4 | Qz/M. granite | ID | 30 | −21.0 | 0.0 | 23.1 | 0.0 | 548.4 | 0.0 | 736.9 | 50.8 | 0.6751 |
| DMMOKA-2-2-1-5 | Qz/M. granite | L-rich | 20 | −15.4 | 0.0 | 19.0 | 0.0 | 328.8 | 0.0 | 111.7 | 11.8 | 0.8721 |
| DMMOKA-2-2-2-1 | Qz/M. granite | ID | 60 | −21.0 | 0.0 | 23.1 | 0.0 | 539.8 | 0.0 | 706.3 | 42.4 | 0.6807 |
| DMMOKA-2-2-2-2 | Qz/M. granite | ID | 40 | −20.0 | 0.4 | 22.4 | 0.3 | 468.9 | 15.7 | 452.3 | 32.6 | 0.7279 |
| DMBAR-1-4-1 | Qz/B. granite | L-rich | 30 | −18.6 | 0.8 | 21.4 | 0.6 | 307.1 | 9.4 | 82.1 | 8.8 | 0.9242 |
| DMBAR-1-4-3 | Qz/B. granite | L-rich | 30 | −20.5 | 0.6 | 22.7 | 0.4 | 365.5 | 4.9 | 165.8 | 12.3 | 0.8615 |
| DMBAR-1-4-6 | Qz/B. granite | L-rich | 40 | −5.3 | 0.2 | 8.2 | 0.2 | 204.3 | 4.2 | 16.1 | 2.6 | 0.9260 |
| DMKAILO-1-2-1 | Qz/B. granite | L-rich | 30 | −12.7 | 0.5 | 16.6 | 0.4 | 347.9 | 2.3 | 143.9 | 9.9 | 0.8204 |
| DMKAILO-1-2-3 | Qz/B. granite | L-rich | 20 | −18.5 | 0.9 | 21.3 | 0.6 | 342.7 | 26.9 | 129.8 | 10.2 | 0.8778 |
| DMKAILO-1-3-1 | Qz/B. granite | L-rich | 30 | −19.2 | 0.2 | 21.8 | 0.2 | 345.7 | 14.6 | 133.8 | 10.9 | 0.8789 |
| DMKAILO-1-3-4 | Qz/B. granite | L-rich | 30 | −20.3 | 0.4 | 22.6 | 0.2 | 354.4 | 4.4 | 146.9 | 13.3 | 0.8752 |
| DMKAILO-1-3-5 | Qz/B. granite | L-rich | 30 | −19.9 | 0.3 | 22.3 | 0.2 | 337.0 | 3.8 | 120.0 | 12.0 | 0.8955 |
| DMNAKE-1-3-1 | Qz/M. greisen | L-rich | 10 | −14.2 | 0.4 | 17.9 | 0.3 | 356.3 | 10.6 | 156.7 | 13.9 | 0.8226 |
| DMNAKE-1-3-2 | Qz/M. greisen | ID | 40 | −15.1 | 0.4 | 18.7 | 0.3 | 425.1 | 4.5 | 315.3 | 10.8 | 0.7292 |
| DMNAKE-1-6-1 | Qz/M. greisen | ID | 60 | −15.3 | 0.2 | 18.8 | 0.1 | 500.8 | 19.6 | 578.1 | 22.8 | 0.6536 |
| DMNAKE-1-4-1 | Qz/M. greisen | L-rich | 20 | −7.7 | 0.1 | 11.5 | 0.2 | 269.8 | 12.6 | 51.3 | 3.9 | 0.8765 |
| DMNAKE-1-4-3 | Qz/M. greisen | L-rich | 20 | −8.1 | 0.0 | 11.8 | 0.1 | 276.3 | 13.9 | 56.6 | 4.1 | 0.8725 |
| DMNAKE-1-4-5 | Qz/M. greisen | L-rich | 20 | −7.7 | 0.5 | 11.3 | 0.6 | 259.6 | 1.3 | 43.5 | 2.0 | 0.8892 |
| DMMOKA-2-8-17-1 | Qz/M. granite | L-rich | 30 | −13.7 | 0.2 | 17.5 | 0.2 | 367.7 | 9.5 | 178.4 | 7.4 | 0.8006 |
| DMMOKA-2-8-17-2 | Qz/M. granite | ID | 40 | −14.7 | 0.2 | 18.3 | 0.1 | 353.8 | 9.1 | 151.7 | 9.0 | 0.8309 |
| DMMOKA-2-8-17-4 | Qz/M. granite | L-rich | 30 | −19.4 | 0.4 | 22.0 | 0.3 | 329.0 | 23.6 | 109.0 | 8.1 | 0.9023 |
| DMMOKA-2-8-13-1 | Qz/M. granite | L-rich | 20 | −8.5 | 0.2 | 12.3 | 0.3 | 271.4 | 9.5 | 52.3 | 2.2 | 0.8829 |
| DMMOKA-2-8-13-4 | Qz/M. granite | L-rich | 30 | −10.9 | 0.2 | 14.8 | 0.2 | 216.5 | 6.1 | 19.5 | 0.8 | 0.9669 |
| DMMOKA-2-8-13-6 | Qz/M. granite | L-rich | 20 | −18.0 | 0.4 | 20.9 | 0.3 | 305.9 | 4.3 | 81.0 | 13.2 | 0.9215 |
| DMMOKA-2-8-13-8 | Qz/M. granite | L-rich | 30 | −20.3 | 0.3 | 22.6 | 0.2 | 214.3 | 4.9 | 20.0 | 2.3 | 1.0270 |
| DMYUB-1-9-1 | Qz/M. vein | L-rich | 30 | −13.9 | 0.3 | 17.7 | 0.3 | 214.1 | 8.3 | 18.1 | 0.9 | 0.9929 |
| DMYUB-1-9-3 | Qz/M. vein | L-rich | 30 | −19.4 | 0.2 | 22.0 | 0.1 | 239.4 | 0.8 | 28.0 | 3.1 | 1.0050 |
| DMYUB-1-9-5 | Qz/M. vein | L-rich | 20 | −15.3 | 0.7 | 18.9 | 0.6 | 349.8 | 10.6 | 144.2 | 11.8 | 0.8421 |
| DMYUB-1-10-3 | Qz/M. vein | L-rich | 30 | −20.5 | 0.3 | 22.7 | 0.2 | 305.2 | 15.2 | 78.9 | 5.5 | 0.9393 |
| DMYUB-1-10-5 | Qz/M. vein | L-rich | 30 | −10.6 | 0.1 | 14.6 | 0.1 | 201.0 | 8.9 | 14.3 | 2.7 | 0.9796 |
| DMYUB-1-10-8 | Qz/M. vein | L-rich | 20 | −20.0 | 0.1 | 22.4 | 0.1 | 228.1 | 7.6 | 22.6 | 2.7 | 1.0190 |
| DMYUB-1-8-1 | Qz/M. vein | L-rich | 30 | −16.4 | 1.0 | 19.8 | 0.8 | 173.7 | 9.7 | 7.3 | 0.5 | 1.0460 |
| DMYUB-1-8-3 | Qz/M. vein | L-rich | 20 | −17.9 | 0.3 | 20.9 | 0.2 | 249.2 | 0.9 | 33.7 | 11.0 | 0.9851 |
| DMBAT-1-2-1 | Qz/M. vein | L-rich | 30 | −9.4 | 0.2 | 13.3 | 0.2 | 290.4 | 8.1 | 69.2 | 15.1 | 0.8678 |
| DMBAT-1-2-2 | Qz/M. vein | L-rich | 30 | −10.3 | 0.3 | 14.3 | 0.3 | 305.2 | 4.0 | 84.8 | 12.6 | 0.8572 |
| DMBAT-1-1-1 | Qz/M. vein | L-rich | 20 | −9.3 | 0.4 | 13.1 | 0.4 | 306.8 | 8.6 | 87.4 | 14.5 | 0.8444 |
| DMBAT-1-1-2 | Qz/M. vein | L-rich | 30 | −4.4 | 0.4 | 7.0 | 0.6 | 189.0 | 1.5 | 11.7 | 1.9 | 0.9318 |
| DMBAT-1-3-1 | Qz/M. vein | L-rich | 35 | −10.6 | 0.5 | 14.5 | 0.6 | 347.4 | 34.1 | 145.5 | 10.5 | 0.7987 |
| DMBAT-1-5-1 | Qz/M. vein | L-rich | 35 | −5.2 | 0.2 | 8.1 | 0.2 | 205.7 | 4.9 | 16.6 | 4.3 | 0.9234 |
| DMBAT-1-5-3 | Qz/M. vein | L-rich | 35 | −6.7 | 0.2 | 10.1 | 0.2 | 273.0 | 18.6 | 54.4 | 4.6 | 0.8611 |
| DMBAT-1-5-5 | Qz/M. vein | L-rich | 35 | −6.2 | 0.2 | 9.5 | 0.3 | 235.4 | 6.2 | 29.1 | 3.3 | 0.9017 |
| DMBAT-1-6-1 | Qz/M. vein | L-rich | 20 | −6.7 | 0.1 | 10.1 | 0.2 | 253.6 | 15.9 | 39.8 | 5.9 | 0.8857 |
| DMBAT-1-6-3 | Qz/M. vein | L-rich | 20 | −10.1 | 0.2 | 14.0 | 0.3 | 301.3 | 0.4 | 80.5 | 13.0 | 0.8604 |
| DMMOKA-2-E-1 | Qz/M. granite | L-rich | 30 | −5.4 | 0.2 | 8.4 | 0.3 | 280.5 | 10.4 | 61.7 | 11.1 | 0.8351 |

**Table 5.** *Cont.*

| FIAs | Host/Rock | Type | Bubble | Tm_Avg. | Tm_Std. | S_Avg. | S_Std. | Th_Avg. | Th_Std. | P_Avg. | P_Std. | Density |
|---|---|---|---|---|---|---|---|---|---|---|---|---|
| | | | *Vol.%* | *Degree* (°C) | | *Wt.% NaCl equiv.* | | *Degree* (°C) | | *Bar* | | g/cm$^3$ |
| DMMOKA-2-E-3 | Qz/M. granite | L-rich | 30 | −9.0 | 0.2 | 12.8 | 0.2 | 311.1 | 9.7 | 92.9 | 11.9 | 0.8350 |
| DMMOKA-2-E-5 | Qz/M. granite | L-rich | 30 | −5.5 | 0.2 | 8.5 | 0.2 | 271.1 | 4.7 | 53.4 | 10.1 | 0.8493 |
| DMMOKA-2-E-8 | Qz/M. granite | L-rich | 30 | −10.3 | 0.1 | 14.3 | 0.1 | 356.4 | 4.1 | 161.9 | 23.9 | 0.7809 |
| DMMOKA-2-F-1 | Qz/M. granite | L-rich | 30 | −18.3 | 0.1 | 21.2 | 0.1 | 240.9 | 17.0 | 29.0 | 6.3 | 0.9963 |
| DMMOKA-2-F-2 | Qz/M. granite | L-rich | 30 | −15.2 | 0.4 | 18.8 | 0.4 | 217.5 | 6.3 | 19.1 | 6.9 | 0.9989 |
| DMMOKA-2-F-6 | Qz/M. granite | L-rich | 30 | −13.4 | 0.3 | 17.3 | 0.2 | 232.6 | 12.6 | 25.9 | 5.2 | 0.9706 |
| DMMOKA-2-G-1 | Qz/M. granite | ID | 40 | −6.9 | 0.3 | 10.4 | 0.4 | 349.5 | 19.0 | 154.0 | 15.6 | 0.7466 |
| DMMOKA-2-G-3 | Qz/M. granite | L-rich | 30 | −4.1 | 0.2 | 6.5 | 0.4 | 247.8 | 8.7 | 36.9 | 7.7 | 0.8621 |
| DMMOKA-2-G-6 | Qz/M. granite | L-rich | 30 | −9.4 | 0.3 | 13.2 | 0.3 | 285.3 | 4.8 | 64.2 | 9.9 | 0.8745 |
| DMMOKA-2-H-1 | Qz/M. granite | ID | 40 | −5.9 | 0.7 | 9.0 | 0.9 | 335.7 | 7.2 | 131.3 | 19.0 | 0.7556 |
| DMMOKA-2-I-1 | Qz/M. granite | ID | 40 | −5.7 | 1.1 | 8.7 | 1.4 | 272.1 | 19.9 | 54.1 | 8.7 | 0.8504 |
| DMMOKA-2-I-2 | Qz/M. granite | ID | 40 | −5.2 | 0.2 | 8.1 | 0.2 | 345.7 | 14.2 | 149.4 | 11.3 | 0.7259 |
| DMMOKA-2-I-3 | Qz/M. granite | ID | 60 | −5.8 | 0.0 | 9.0 | 0.0 | 400.1 | 0.0 | 269.9 | 30.4 | 0.6267 |
| DMMOKA-2-M-1 | Qz/M. granite | ID | 50 | −2.7 | 0.2 | 4.5 | 0.3 | 291.0 | 4.6 | 73.8 | 14.2 | 0.7805 |
| DMMOKA-2-M-2 | Qz/M. granite | L-rich | 30 | −5.6 | 0.1 | 8.7 | 0.1 | 272.0 | 8.3 | 54.1 | 10.2 | 0.8493 |
| DMMOKA-2-M-3 | Qz/M. granite | L-rich | 30 | −2.7 | 0.2 | 4.4 | 0.2 | 215.1 | 4.8 | 20.5 | 2.1 | 0.8838 |
| DMMOKA-2-M-4 | Qz/M. granite | L-rich | 30 | −17.4 | 0.3 | 20.5 | 0.2 | 225.7 | 15.2 | 22.0 | 3.6 | 1.0060 |
| DMMOKA-2-M-8 | Qz/M. granite | ID | 40 | −8.1 | 0.1 | 11.8 | 0.1 | 305.2 | 5.0 | 86.3 | 13.2 | 0.8331 |
| DMKAILO-1-12-1 | Qz/B. granite | ID | 40 | −11.5 | 0.5 | 15.4 | 0.4 | 331.6 | 4.7 | 119.1 | 15.6 | 0.8322 |
| DMKAILO-1-8-1 | Qz/B. granite | L-rich | 30 | −10.7 | 0.1 | 14.7 | 0.1 | 342.4 | 2.3 | 136.9 | 11.3 | 0.8075 |
| DMKAILO-1-8-3 | Qz/B. granite | ID | 30 | −12.3 | 0.2 | 16.2 | 0.1 | 367.8 | 2.6 | 180.6 | 14.0 | 0.7857 |
| DMKAILO-1-11-1 | Qz/B. granite | L-rich | 20 | −8.2 | 0.3 | 11.9 | 0.3 | 249.2 | 16.3 | 36.4 | 2.8 | 0.9067 |
| DMBAR-1-5-1 | Qz/B. granite | L-rich | 40 | −11.4 | 0.4 | 15.4 | 0.4 | 137.7 | 2.7 | 3.0 | 0.1 | 1.0400 |
| DMBAR-1-5-2 | Qz/B. granite | L-rich | 20 | −2.1 | 0.1 | 3.6 | 0.2 | 123.0 | 2.4 | 2.1 | 0.3 | 0.9653 |
| DMBAR-1-5-4 | Qz/B. granite | L-rich | 30 | −1.6 | 0.1 | 2.7 | 0.2 | 145.5 | 5.0 | 4.1 | 1.5 | 0.9408 |
| DMBAR-1-5-6 | Qz/B. granite | L-rich | 30 | −3.3 | 0.3 | 5.4 | 0.5 | 127.9 | 2.3 | 2.4 | 0.4 | 0.9745 |
| DMBAR-1-5-7 | Qz/B. granite | L-rich | 30 | −8.4 | 0.3 | 12.1 | 0.3 | 123.0 | 2.4 | 2.0 | 0.7 | 1.0270 |
| DMBAR-1-5-11 | Qz/B. granite | L-rich | 30 | −2.5 | 0.1 | 4.2 | 0.2 | 178.1 | 7.7 | 9.3 | 1.1 | 0.9209 |
| DMBAR-1-5-12 | Qz/B. granite | L-rich | 30 | −2.5 | 0.3 | 4.1 | 0.4 | 145.2 | 5.0 | 4.1 | 1.3 | 0.9514 |
| DMBALE-1-8-1 | Qz/B. granite | L-rich | 20 | −16.1 | 0.1 | 19.5 | 0.0 | 349.8 | 4.4 | 143.4 | 14.3 | 0.8490 |
| DMBALE-1-8-3 | Qz/B. granite | L-rich | 20 | −10.6 | 0.1 | 14.5 | 0.2 | 304.8 | 3.4 | 84.2 | 10.2 | 0.8608 |
| DMMOGA-1-2-1 | Qz/M. peg. | L-rich | 30 | −4.7 | 0.2 | 7.4 | 0.2 | 295.3 | 4.8 | 77.2 | 9.2 | 0.8041 |
| DMMOGA-1-2-3 | Qz/M. peg. | L-rich | 20 | −4.1 | 0.1 | 6.6 | 0.1 | 200.2 | 0.2 | 15.0 | 3.4 | 0.9170 |
| DMMOGA-1-2-4 | Qz/M. peg. | L-rich | 20 | −7.2 | 0.2 | 10.7 | 0.2 | 215.2 | 3.2 | 19.7 | 5.0 | 0.9343 |
| DMMOGA-1-3-1 | Qz/M. peg. | L-rich | 30 | −5.2 | 0.2 | 8.1 | 0.2 | 206.9 | 5.1 | 17.0 | 5.1 | 0.9222 |
| DMMOGA-1-4-1 | Qz/M. peg. | L-rich | 20 | −5.4 | 0.2 | 8.3 | 0.2 | 207.5 | 6.1 | 17.2 | 3.1 | 0.9237 |
| DMMOGA-1-4-2 | Qz/M. peg. | ID | 40 | −6.4 | 0.1 | 9.7 | 0.1 | 311.0 | 2.6 | 94.8 | 14.2 | 0.8033 |
| DMBAT-1-16-1 | Qz/M. vein | L-rich | 30 | −10.4 | 0.3 | 14.3 | 0.3 | 333.1 | 11.3 | 122.4 | 10.8 | 0.8183 |
| DMBAT-1-18-1 | Qz/M. vein | L-rich | 30 | −13.2 | 0.2 | 17.1 | 0.2 | 344.7 | 3.7 | 138.0 | 13.8 | 0.8301 |
| DMBAT-1-18-2 | Qz/M. vein | L-rich | 30 | −11.5 | 0.2 | 15.4 | 0.2 | 308.4 | 6.1 | 87.8 | 6.8 | 0.8648 |
| DMBAT-1-18-4 | Qz/M. vein | L-rich | 35 | −5.5 | 0.3 | 8.5 | 0.4 | 289.2 | 7.4 | 70.2 | 8.8 | 0.8240 |
| DMBAT-1-15-1 | Qz/M. vein | L-rich | 30 | −16.6 | 0.0 | 19.9 | 0.0 | 329.7 | 0.0 | 112.1 | 8.9 | 0.8806 |
| DMBAT-1-15-2 | Qz/M. vein | L-rich | 20 | −7.5 | 0.3 | 11.1 | 0.4 | 272.5 | 7.7 | 53.6 | 11.4 | 0.8708 |
| DMBAT-1-15-4 | Qz/M. vein | L-rich | 30 | −6.2 | 0.4 | 9.5 | 0.5 | 234.8 | 7.3 | 28.8 | 4.3 | 0.9024 |
| DMYUB-1-2-1 | Qz/M. vein | L-rich | 30 | −16.1 | 0.1 | 19.5 | 0.1 | 316.8 | 11.3 | 95.1 | 7.6 | 0.8936 |
| DMYUB-1-2-2 | Qz/M. vein | L-rich | 30 | −15.4 | 0.4 | 19.0 | 0.3 | 235.6 | 3.1 | 27.0 | 6.3 | 0.9822 |
| DMNAKE-1-1 | Cst/M. greisen | L-rich | 30 | −1.8 | 0.5 | 3.0 | 0.8 | 271.0 | 19.0 | 56.8 | 17.2 | 0.7960 |
| DMNAKE-1-2 | Cst/M. greisen | L-rich | 30 | −1.6 | 0.3 | 2.7 | 0.4 | 262.5 | 29.8 | 52.1 | 20.2 | 0.8035 |
| DMNAKE-1-3 | Cst/M. greisen | ID | 40 | −5.8 | 0.3 | 8.9 | 0.4 | 326.2 | 17.4 | 118.7 | 27.7 | 0.7687 |
| DMNAKE-1-4 | Cst/M. greisen | L-rich | 20 | −1.2 | 0.1 | 2.1 | 0.2 | 233.2 | 4.0 | 29.3 | 2.1 | 0.8414 |
| DMNAKE-1-5 | Cst/M. greisen | L-rich | 20 | −1.4 | 0.2 | 2.3 | 0.3 | 237.9 | 8.3 | 32.1 | 4.8 | 0.8373 |
| DMNAKE-1-6 | Cst/M. greisen | L-rich | 30 | −2.3 | 0.3 | 3.9 | 0.5 | 216.3 | 6.2 | 21.2 | 2.5 | 0.8772 |
| DMNAKE-1-7 | Cst/M. greisen | L-rich | 30 | −1.2 | 0.2 | 2.1 | 0.3 | 243.8 | 10.9 | 35.8 | 6.8 | 0.8275 |
| DMNAKE-1-8 | Cst/M. greisen | L-rich | 20 | −2.0 | 0.4 | 3.3 | 0.6 | 235.2 | 28.6 | 33.5 | 19.2 | 0.8469 |
| DMMAKU-1-4-9 | Cst/M. vein | L-rich | 30 | −3.2 | 0.2 | 5.2 | 0.3 | 271.2 | 33.1 | 60.6 | 35.6 | 0.8143 |
| DMMAKU-1-4-10 | Cst/M. vein | L-rich | 20 | −6.8 | 0.5 | 10.2 | 0.6 | 339.1 | 20.6 | 138.8 | 32.4 | 0.7622 |
| DMMAKU-1-4-11 | Cst/M. vein | L-rich | 30 | −3.4 | 0.2 | 5.6 | 0.3 | 247.1 | 26.1 | 39.6 | 19.3 | 0.8522 |
| DMBAT-1-2-12 | Cst/M. vein | L-rich | 30 | −3.0 | 0.2 | 5.0 | 0.3 | 254.1 | 22.2 | 43.6 | 15.0 | 0.8380 |
| DMYUB-1B-13 | Cst/M. vein | ID | 40 | −4.4 | 0.3 | 6.9 | 0.5 | 330.0 | 14.8 | 125.3 | 23.4 | 0.7399 |
| DMYUB-1B-14 | Cst/M. vein | L-rich | 30 | −2.5 | 0.4 | 4.2 | 0.6 | 263.1 | 21.9 | 50.4 | 16.5 | 0.8190 |
| DMYUB-1B-15 | Cst/M. vein | L-rich | 20 | −2.0 | 0.1 | 3.4 | 0.2 | 254.4 | 14.7 | 43.0 | 10.6 | 0.8240 |
| DMYUB-1B-16 | Cst/M. vein | ID | 50 | −1.9 | 0.2 | 3.2 | 0.3 | 279.3 | 18.7 | 64.3 | 17.5 | 0.7849 |
| DMYUB-1C-17 | Cst/M. vein | L-rich | 40 | −6.1 | 0.4 | 9.3 | 0.5 | 313.5 | 10.8 | 99.1 | 14.4 | 0.7921 |
| DMNAKE-1-2-18 | Cst/M. greisen | ID | 40 | −2.4 | 0.1 | 4.0 | 0.2 | 292.3 | 9.2 | 75.9 | 10.0 | 0.7731 |
| DMNAKE-1-2-19 | Cst/M. greisen | L-rich | 30 | −2.3 | 0.3 | 3.8 | 0.5 | 265.2 | 14.7 | 51.0 | 10.7 | 0.8128 |
| DMNAKE-1-2-20 | Cst/M. greisen | L-rich | 30 | −2.3 | 0.2 | 3.8 | 0.3 | 234.0 | 23.4 | 31.4 | 12.1 | 0.8541 |
| DMNAKE-1-2-21 | Cst/M. greisen | ID | 50 | −4.2 | 0.6 | 6.7 | 0.6 | 325 | 26.3 | 122.8 | 28.5 | 0.7398 |
| DMNAKE-1-2-22 | Cst/M. greisen | ID | 40 | −5.7 | 0.3 | 8.8 | 0.3 | 320.7 | 15.9 | 116.3 | 38.5 | 0.7688 |
| DMNAKE-1-2-23 | Cst/M. greisen | L-rich | 30 | −2.3 | 0.4 | 3.9 | 0.5 | 241 | 12.4 | 33.5 | 18.5 | 0.8543 |

Notes: S = Apparent salinity in wt.% NaCl equivalent; Tm = Temperature of the last ice melting in Celsius; Th (v) = Homogenization temperature in Celsius; P = Pressure in bar; FIA = Fluid inclusion assemblage; Avg = Average; Std = Standard deviation; ID = Intermediate density fluid inclusion; L-rich = Liquid-rich fluid inclusion; Qz = Quartz; Fl = Fluorite; Cassiterite = Cst; M. = Mineralized; B. = Barren.

**Author Contributions:** Conception of the project, D.K.M. and J.H.S.; field works and sampling, D.K.M., A.T.O. and F.M.M.; petrographic and geochemical analyses (EPMA, LA-ICPMS, Raman spectroscopy, SEM-EDS, SEM-CL, and fluid inclusion microthermometry), D.K.M., J.H.S., J.O. and P.K.; data validation and curation, J.H.S. and I.L.; writing—original draft preparation, D.K.M.; writing—review, editing, D.K.M. and J.H.S.; supervision, J.H.S. and I.L.; funding acquisition, D.K.M. and J.H.S. All authors have read and agreed to the published version of the manuscript.

**Funding:** The present study is part of the first author's Ph.D. and received financial support from the National Institute for International Education and Development (NIIED-2020, grant number NIIED-200807-0012) in the Republic of Korea (D.K.M.). The National Research Foundation (NRF) of Korea Grant is funded by the Korean government (MSIT) (No. 2022R1A2C4001512) (J.H.S.).

**Data Availability Statement:** Not applicable.

**Acknowledgments:** We kindly acknowledge Gerhard Bringmann, Mudogo Virima, and Karine Ndjoko Ioset through the BEBUC program and the Kroëner Foundation for sample transportation costs. Thanks to Haemyeong Jung, Jung-Woo Park, Makutu Ma-Ngwayaya Adalbert, Kanika Mayena Thomas, and Kabonwa Janvier for constructive discussions, advice, and fruitful remarks on the achievements of this study. Thanks to Junhee Lee, TongHa Lee, Yevgeniya Kim, Yuri Choi, Hahyeon Park, Yechan Jeon, Ivan Bongwe, and Dedel Milikwini for the material and sample preparations.

**Conflicts of Interest:** The authors declare no conflict of interest.

## References

1. Cacho, A.; Melgarejo, J.C.; Camprubi, A.; Torro, L.; Castillo-Oliver, M.; Torres, B.; Artiaga, D.; Tauler, E.; Martinez, A.; Campeny, M.; et al. Mineralogy and Distribution of Critical Elements in the Sn-W-Pb-Ag-Zn Huanuni Deposit, Bolivia. *Minerals* **2019**, *9*, 753. [CrossRef]
2. Černý, P.; Ercit, T.S. The classification of granitic pegmatites revisited. *Can. Mineral.* **2005**, *43*, 2005–2026. [CrossRef]
3. Černý, P.; Ercit, T.S. Some recent advances in the mineralogy and geochemistry of Nb and Ta in rare-element granitic pegmatites. *Bull. Minéralogie* **1985**, *108*, 499–532. [CrossRef]
4. Che, X.D.; Linnen, R.L.; Wang, R.C.; Aseri, A.; Thibault, Y. Tungsten solubility in evolved granitic melts: An evaluation of magmatic wolframite. *Geochim. Cosmochim. Acta* **2013**, *106*, 84–98. [CrossRef]
5. Dill, H.G. Pegmatites and aplites: Their genetic and applied ore geology. *Ore Geol. Rev.* **2015**, *69*, 417–561. [CrossRef]
6. Hulsbosch, N. Nb-Ta-Sn-W Distribution in Granite-related Ore Systems: Fractionation mechanisms and examples from the Karagwe-Ankole Belt of Central Africa. In *Ore Deposits*; Geophysical Monograph Series; John Wiley and Sons: Hoboken, NJ, USA, 2019; Volume 242, pp. 75–107.
7. Tchunte, P.M.F.; Tchameni, R.; André-Mayer, A.S.; Dakoure, H.S.; Turlin, F.; Poujol, M.; Nomo, E.N.; Fouotsa, A.N.S.; Rouer, O. Evidence for Nb-Ta Occurrences in the Syn-Tectonic Pan-African Mayo Salah Leucogranite (Northern Cameroon): Constraints from Nb-Ta Oxide Mineralogy, Geochemistry and U-Pb LA-ICP-MS Geochronology on Columbite and Monazite. *Minerals* **2018**, *8*, 188. [CrossRef]
8. Varlamoff, N. Central and West African Rare-Metal Granitic Pegmatites, related aplites, quartz veins and mineral deposits. *Miner. Depos.* **1972**, *7*, 202–216. [CrossRef]
9. Chen, Y.; Song, S.; Niu, Y.; Wei, C. Melting of continental crust during subduction initiation: A case study from the Chaidanuo peraluminous granite in the North Qilian suture zone. *Geochim. Cosmochim. Acta* **2014**, *132*, 311–336. [CrossRef]
10. Debruyne, D.; Hulsbosch, N.; Wilderode, J.V.; Balcaen, L.; Vanhaecke, F.A.; Muchez, P. Regional geodynamic context for the Mesoproterozoic Kibara Belt (KIB) and the Karagwe-Ankole Belt: Evidence from geochemistry and isotopes in the KIB. *Precambrian Res.* **2015**, *264*, 82–97. [CrossRef]
11. Kemp, A.I.S.; Hawkesworth, C.J.; Foster, G.L.; Paterson, B.A.; Woodhead, J.D.; Hergt, J.M.; Gray, C.M.; Whitehouse, M.J. Magmatic and Crustal Differentiation History of Granitic Rocks from Hf-O Isotopes in Zircon. *Am. Assoc. Adv. Sci.* **2007**, *315*, 980–983. [CrossRef]
12. Sylvester, P.J. Post-collisional strongly peraluminous granites. *Lithos* **1998**, *45*, 29–44. [CrossRef]
13. Clemens, J.; Watkins, J. The fluid regime of high-temperature metamorphism during granitoid magma genesis. *Contrib. Mineral. Petrol.* **2001**, *140*, 600–606. [CrossRef]
14. Van Daele, J.; Hulsbosch, N.; Dewaele, S.; Boiron, M.C.; Piessens, K.; Boyce, A.; Muchez, P. Mixing of magmatic-hydrothermal and metamorphic fluids and the origin of peribatholitic Sn vein-type deposits in Rwanda. *Ore Geol. Rev.* **2018**, *101*, 481–501. [CrossRef]
15. Heinrich, C.A. The chemistry of hydrothermal tin (-tungsten) ore deposition. *Econ. Geol.* **1990**, *90*, 705–729. [CrossRef]
16. Audetat, A.; Gunther, D.; Heinrich, C.A. Formation of a magmatic-hydrothermal ore deposit: Insights with LA-ICP-MS analysis of fluid inclusions. *Science* **1998**, *279*, 2091–2094. [CrossRef] [PubMed]
17. Chen, Y.J.; Pirajno, F.; Qi, J.P. Origin of Gold Metallogeny and Sources of Ore-Forming Fluids, Jiaodong Province, Eastern China. *Int. Geol. Rev.* **2005**, *47*, 530–549. [CrossRef]
18. Baker, T.; Pollard, P.J.; Mustard, R.; Mark, G.; Graham, J. A comparison of granite-related tin, tungsten, and gold-bismuth deposits: Implications for exploration. *SEG Discov.* **2005**, *61*, 5–17. [CrossRef]
19. Audetat, A.A.; Edmonds, M. Magmatic-Hydrothermal Fluids. *Elements* **2020**, *16*, 401–406. [CrossRef]
20. Lerouge, C.; Gloaguen, E.; Wille, G.; Bailly, L. Distribution of In and other rare metals in cassiterite and associated minerals in Sn ± W ore deposits of the western Variscan Belt. *Eur. J. Mineral.* **2017**, *29*, 739–753. [CrossRef]
21. Serranti, S.; Ferrini, V.; Masi, U.; Cabri, L.J. Trace element distribution in cassiterite and sulfides from rubane and massive ores of the corvo deposit, Portugal. *Can. Mineral.* **2002**, *40*, 815–835. [CrossRef]
22. Zhang, D.H.; Audetat, A. Magmatic-Hydrothermal Evolution of the Barren Huangshan Pluton, Anhui Province, China: A Melt and Fluid Inclusion Study. *Econ. Geol.* **2018**, *113*, 803–824. [CrossRef]
23. Zhang, Q.; Zhang, R.-Q.; Gao, J.-F.; Lu, J.-J.; Wu, J.-W. In-situ LA-ICP-MS trace element analyses of scheelite and wolframite: Constraints on the genesis of veinlet-disseminated and vein-type tungsten deposits, South China. *Ore Geol. Rev.* **2018**, *99*, 166–179. [CrossRef]

24. Wille, G.; Lerouge, C.; Schmidt, U. A multimodal microcharacterisation of trace-element zonation and crystallographic orientation in natural cassiterite by combining cathodoluminescence, EBSD, EPMA and contribution of confocal Raman-in-SEM imaging. *J. Microsc.* **2018**, *270*, 309–317. [CrossRef] [PubMed]
25. Bennett, J.M.; Hagemann, S.; Fiorentini, M.; Roberts, M.P. Sn-W-Critical Metals & Associated Magmatic Systems, the chemical variability of cassiterite microstructures. In Proceedings of the International Geological Conference, Tinaroo, QLD, Australia, 24–28 June 2019; pp. 1–121.
26. Cheng, Y.; Spandler, C.; Kemp, A.; Mao, J.; Rusk, B.; Hu, Y.; Blake, K. Controls on cassiterite ($SnO_2$) crystallization: Evidence from cathodoluminescence, trace-element chemistry, and geochronology at the Gejiu Tin District. *Am. Mineral.* **2019**, *104*, 118–129. [CrossRef]
27. Farmer, C.B.; Searl, A.; Halls, C. Cathodoluminescence and growth of cassiterite the composite lodes at South Crofty Mine, Cornwall, England. *Mineral. Soc.* **1991**, *55*, 447–458. [CrossRef]
28. Nambaje, C.; Eggins, S.M.; Yaxley, G.M.; Sajeev, K. Micro-characterisation of cassiterite by geology, texture and zonation: A case study of the Karagwe Ankole Belt, Rwanda. *Ore Geol. Rev.* **2020**, *124*, 103609. [CrossRef]
29. Lecumberri-Sanchez, P.; Steele-MacInnis, M.; Bodnar, R.J. Synthetic fluid inclusions XIX: Experimental determination of the vapor-saturated liquidus of the system $H_2O$-NaCl-$FeCl_2$. *Geochim. Cosmochim. Acta* **2015**, *148*, 34–49. [CrossRef]
30. Lecumberri-Sanchez, P.; Steele-MacInnis, M.; Weis, P.; Driesner, T.; Bodnar, R.J. Salt precipitation in magmatic-hydrothermal systems associated with upper crustal plutons. *Geology* **2015**, *43*, 1063–1066. [CrossRef]
31. Seo, J.H.; Kim, Y.; Lee, T.; Guillong, M. Periodically Released Magmatic Fluids Create a Texture of Unidirectional Solidification (UST) in Ore-Forming Granite: A Fluid and Melt Inclusion Study of W-Mo Forming Sannae-Eonyang Granite, Korea. *Minerals* **2021**, *11*, 888. [CrossRef]
32. Seo, J.H.; Yoo, B.C.; Villa, I.M.; Lee, J.H.; Lee, T.; Kim, C.; Moon, K.J. Magmatic–hydrothermal processes in Sangdong W–Mo deposit, Korea: Study of fluid inclusions and 39Ar–40Ar geochronology. *Ore Geol. Rev.* **2017**, *91*, 316–334. [CrossRef]
33. Frezzotti, M.L.; Tecce, F.; Casagli, A. Raman spectroscopy for fluid inclusion analysis. *J. Geochem. Explor.* **2012**, *112*, 1–20. [CrossRef]
34. Bakker, R.J.a.; Diamond, L.W. Determination of the composition and molar volume of $H_2O$-$CO_2$ fluid inclusions by microthermometry. *Geochim. Cosmochim. Acta* **2000**, *64*, 1753–1764. [CrossRef]
35. Diamond, L.W. Stability of $CO_2$ clathrate hydrate + $CO_2$, liquid + $CO_2$ vapour + aqueous KCl-NaCl solutions: Experimental determination and application to salinity estimates of fluid inclusions. *Geochim. Cosmochim. Acta* **1992**, *56*, 273–280. [CrossRef]
36. Diamond, L.W. Review of the systematics of $CO_2$–$H_2O$ fluid inclusions. *Lithos* **2001**, *55*, 69–99. [CrossRef]
37. Audetat, A. Quantitative analysis of melt and fluid inclusions by LA-ICP-MS: Practical aspects and selected results. *Acta Petrol. Sin.* **2000**, *16*, 715.
38. Audétat, A. The Metal Content of Magmatic-Hydrothermal Fluids and Its Relationship to Mineralization Potential. *Econ. Geol.* **2019**, *114*, 1033–1056. [CrossRef]
39. Audetat, A.; Gunther, D.; Heinrich, C.A. Causes for large-scale metal zonation around mineralized plutons: Fluid inclusion LA-ICP-MS evidence from the Mole Granite, Australia. *Econ. Geol. Bull. Soc.* **2000**, *95*, 1563–1581. [CrossRef]
40. Heinrich, C.A.; Gunther, D.; Audetat, A.; Ulrich, T.; Frischknecht, R. Metal fractionation between magmatic brine and vapor, determined by microanalysis of fluid inclusions. *Geology* **1999**, *27*, 755–758. [CrossRef]
41. Heinrich, C.A.; Pettke, T.; Halter, W.E.; Aigner-Torres, M.; Audetat, A.; Gunther, D.; Hattendorf, B.; Bleiner, D.; Guillong, M.; Horn, I. Quantitative multi-element analysis of minerals, fluid and melt inclusions by laser-ablation inductively-coupled-plasma mass-spectrometry. *Geochim. Cosmochim. Acta* **2003**, *67*, 3473–3497. [CrossRef]
42. Lecumberri-Sanchez, P.; Romer, R.L.; Luders, V.; Bodnar, R.J. Genetic relationship between silver-lead-zinc mineralization in the Wutong deposit, Guangxi Province and Mesozoic granitic magmatism in the Nanling belt, southeast China. *Miner. Depos.* **2014**, *49*, 353–369. [CrossRef]
43. Lerchbaumer, L.; Audetat, A. Partitioning of Cu between vapor and brine—An experimental study based on LA-ICP-MS analysis of synthetic fluid inclusions. *Geochim. Cosmochim. Acta* **2009**, *73*, 743–744.
44. Melcher, F.; Graupner, T.; Gabler, H.E.; Sitnikova, M.; Henjes-Kunst, F.; Oberthur, T.; Gerdes, A.; Dewaele, S. Tantalum-(niobium-tin) mineralisation in African pegmatites and rare metal granites: Constraints from Ta-Nb oxide mineralogy, geochemistry and U-Pb geochronology. *Ore Geol. Rev.* **2015**, *64*, 667–719. [CrossRef]
45. Dewaele, S.; De Clercq, F.; Hulsbosch, N.; Piessens, K.; Boyce, A.; Burgess, R.; Muchez, P. Genesis of the vein-type tungsten mineralization at Nyakabingo (Rwanda) in the Karagwe-Ankole belt, Central Africa. *Miner. Depos.* **2016**, *51*, 283–307. [CrossRef]
46. Dewaele, S.; DeClerq, F.; Muchez, P.; Schneider, J.; Burgess, R.; Boyce, A.; Fernandez-Alonso, M. Geology of the cassiterite mineralisation in the Rutongo area, Rwanda (Central Africa): Current state of knowledge. *Geol. Belg.* **2010**, *13*, 91–112.
47. Dewaele, S.; Goethal, H.; Thys, T. Mineralogical characterization of cassiterite concentrates from quartz vein and pegmatite mineralization of the Karagwe-Ankole and Kibara Belts, Central Africa. *Geol. Belg.* **2013**, *16*, 66–75.
48. Dewaele, S.; Henjes-Kunst, F.; Melcher, F.; Sitnikova, M.; Burgess, R.; Gerdes, A.; Fernandez, M.A.; Clercq, F.D.; Muchez, P.A.; Lehmann, B. Late Neoproterozoic overprinting of the cassiterite and columbite-tantalite bearing pegmatites of the Gatumba area, Rwanda (Central Africa). *J. Afr. Earth Sci.* **2011**, *61*, 10–26. [CrossRef]

49. Dewaele, S.; Hulsbosch, N.; Cryns, Y.; Boyce, A.; Burgess, R.A.; Muchez, P. Geological setting and timing of the world-class Sn, Nb-Ta and Li mineralization of Manono-Kitotolo (Katanga, Democratic Republic of Congo). *Ore Geol. Rev.* **2016**, *72*, 373–390. [CrossRef]
50. Dewaele, S.; Muchez, P.; Burgess, R.A.; Boyce, A. Geological setting and timing of the cassiterite vein type mineralization of the Kalima area (Maniema, Democratic Republic of Congo). *J. Afr. Earth Sci.* **2015**, *112*, 199–212. [CrossRef]
51. Pohl, W.; Biryabarema, M.a.; Lehmann, B. Early Neoproterozoic rare metal (Sn, Ta, W) and gold metallogeny of the Central Africa Region: A review. *Appl. Earth Sci.* **2013**, *122*, 66–82. [CrossRef]
52. Pohl, W. The origin of Kibaran (late Mid-Proterozoic) tin, tungsten and gold quartz vein deposits in Central Africa: A fluid inclusions study. *Miner. Depos.* **1991**, *26*, 51–59. [CrossRef]
53. Wouters, S.; Hulsbosch, N.; Kaskes, P.; Claeys, P.; Dewaele, S.; Melcher, F.; Onuk, P.; Muchez, P. Late orogenic gold mineralization in the western domain of the Karagwe-Ankole Belt (Central Africa): Auriferous quartz veins from the Byumba deposit (Rwanda). *Ore Geol. Rev.* **2020**, *125*, 103666. [CrossRef]
54. Fernandez-Alonso, M.; Mupande, J.-F.; Badosa, T.; Baudet, D.; Dewaele, S.; Kalenga, H.; Kampata, D.; Kanda, N.V.; Lahmouch, M.; Lahogue, P.; et al. *New 1/2,5 Million Scale Geologic and Mineral Occurrences Maps of the Democratic Republic of Congo*; Royal Museum for Central Africa: Tervuren, Belgium, 2016.
55. RMCA. *Geological Map of the Democratic Republic of Congo, Scale of 1/25 000000*; Royal Museum for Central Africa: Tervuren, Belgium, 2006.
56. Fernandez-Alonso, M.; Cutten, H.; De Waele, B.; Tack, L.; Tahon, A.; Baudet, D.; Barritt, S.D. The Mesoproterozoic Karagwe-Ankole Belt (formerly the NE Kibara Belt): The result of prolonged extensional intracratonic basin development punctuated by two short-lived far-field compressional events. *Precambrian Res.* **2012**, *216*, 63–86. [CrossRef]
57. Kampunzu, A.B. The Mesoproterozoic Kibaran belt system in Africa: A key for the reconstruction of Rodinia Supercontinent. *Gondwana Res.* **1998**, *1*, 412–414. [CrossRef]
58. Kampunzu, A.B.; Cailteux, J. Tectonic evolution of the Lufilian Arc (Central Africa Copper belt) during the neoproterozoic Pan-African orogenesis. *Gondwana Res.* **1997**, *1*, 149. [CrossRef]
59. De Waele, B.; Johnson, S.P.; Pisarevsky, S.A. Palaeoproterozoic to Neoproterozoic growth and evolution of the eastern Congo Craton: Its role in the Rodinia puzzle. *Precambrian Res.* **2008**, *160*, 127–141. [CrossRef]
60. Johnson, S.P.; Rivers, T.; De Waele, B. A review of the Mesoproterozoic to early Palaeozoic magmatic and tectonothermal history of south–central Africa: Implications for Rodinia and Gondwana. *J. Geol. Soc.* **2005**, *162*, 433–450. [CrossRef]
61. Lehmann, B.; Halder, S.; Ruzindana Munana, J.; de la Paix Ngizimana, J.; Biryabarema, M. The geochemical signature of rare-metal pegmatites in Central Africa: Magmatic rocks in the Gatumba tin–tantalum mining district, Rwanda. *J. Geochem. Explor.* **2014**, *144*, 528–538. [CrossRef]
62. Tack, L.; Bowden, P. Post-collisional granite magmatism in the central Damaran (Pan-African) Orogenic Belt, western Namibia. *J. Afr. Earth Sci.* **1999**, *28*, 653–674. [CrossRef]
63. Tack, L.; Wingate, M.T.D.; De Waele, B.; Meert, J.; Belousova, E.; Griffin, B.; Tahon, A.; Fernandez-Alonso, M. The 1375Ma "Kibaran event" in Central Africa: Prominent emplacement of bimodal magmatism under extensional regime. *Precambrian Res.* **2010**, *180*, 63–84. [CrossRef]
64. Buurman, I. An Assessment of Sn-W-Nb-Ta Oxide Minerals from the Bugesera District of Rwanda and Geological Context. Ph.D. Thesis, University of Witwatersrand, Johannesburg, South Africa, 2018.
65. Buyse, F.; Dewaele, S.; Decrée, S.; Mees, F. Mineralogical and geochemical study of the rare earth element mineralization at Gakara (Burundi). *Ore Geol. Rev.* **2020**, *124*, 103659. [CrossRef]
66. De Clercq, F. Metallogenis of Tin and Tungsten Vein-Type Deposit in the Karagwe-Ankole Belt (Rwanda). Ph.D. Thesis, Katholieke Universiteit Leuven, Leuven, Belgium, 2012.
67. Villeneuve, M.; Gärtner, A.; Kalikone, C.; Wazi, N.; Hofmann, M.; Linnemann, U. U-Pb ages and provenance of detrital zircon from metasedimentary rocks of the Nya-Ngezie and Bugarama groups (D.R. Congo): A key for the evolution of the Mesoproterozoic Kibaran-Burundian Orogen in Central Africa. *Precambrian Res.* **2019**, *328*, 81–98. [CrossRef]
68. Key, R.; Kampunzu, A.B. IGCP 418 "Evolution of the Kibaran belt system in southwestern Africa: Comparison with equatorial and southern Africa". *J. Afr. Earth Sci.* **1997**, *24*, R9–R10. [CrossRef]
69. Kokonyangi, J. Geological fieldwork in the Kibaran-type region, Mitwaba district, Congo (former Zaire), central Africa. *Gondwana Res.* **2001**, *4*, 255–259. [CrossRef]
70. Kokonyangi, J.; Armstrong, R.; Kampunzu, A.B.; Yoshida, M.; Okudaira, T. U-Pb zircon geochronology and petrology of granitoids from Mitwaba (Katanga, Congo): Implications for the evolution of the Mesoproterozoic Kibaran belt. *Precambrian Res.* **2004**, *132*, 79–106. [CrossRef]
71. Kokonyangi, J.; Kampunzu, A.B.; Poujol, M.; Okudaira, T.; Yoshida, M.; Shabeer, K.P. Petrology and geochronology of Mesoproterozoic mafic-intermediate plutonic rocks from Mitwaba (D. R. Congo): Implications for the evolution of the Kibaran belt in central Africa. *Geol. Mag.* **2005**, *142*, 109–130. [CrossRef]
72. Kokonyangi, J.; Kampunzu, A.B.; Yoshida, M. Lithostratigraphy and structural evolution of the Kalima-Moga tin district, Kibaran belt (Maniema, Congo). *Gondwana Res.* **2000**, *3*, 257–259. [CrossRef]
73. Kokonyangi, J.W.; Kampunzu, A.B.; Armstrong, R.; Yoshida, M.; Okudaira, T.; Arima, M.; Ngulube, D.A. The Mesoproterozoic Kibaride belt (Katanga, SE DR Congo). *J. Afr. Earth Sci.* **2006**, *46*, 1–35. [CrossRef]

74. Tack, L.; Liegeois, J.P.; Deblond, A.; Duchesne, J.C. Kibaran-a-Type Granitoids and Mafic Rocks Generated by 2 Mantle Sources in a Late Orogenic Setting (Burundi). *Precambrian Res.* **1994**, *68*, 323–356. [CrossRef]
75. Kadima, E.; Delvaux, D.; Sebagenzi, S.N.; Tack, L.a.; Kabeya, S.M. Structure and geological history of the Congo Basin: An integrated interpretation of gravity, magnetic and reflection seismic data. *Basin. Res.* **2011**, *23*, 499–527. [CrossRef]
76. Melcher, F.; Graupner, T.; Gäbler, H.-E.; Sitnikova, M.; Oberthür, T.; Gerdes, A.; Badanina, E.; Chudy, T. Mineralogical and chemical evolution of tantalum–(niobium–tin) mineralisation in pegmatites and granites. Part 2: Worldwide examples (excluding Africa) and an overview of global metallogenetic patterns. *Ore Geol. Rev.* **2017**, *89*, 946–987. [CrossRef]
77. Van Daele, J.; Hulsbosch, N.; Dewaele, S.A.; Muchez, P. Metamorphic and metasomatic evolution of Western Domain of the Karagwe-Ankole Belt (Central Africa). *J. Afr. Earth Sci.* **2020**, *165*, 103783. [CrossRef]
78. Maier, W.D.; Barnes, S.J.; Bandyayera, D.; Livesey, T.; Li, C.; Ripley, E. Early Kibaran rift-related mafic–ultramafic magmatism in western Tanzania and Burundi: Petrogenesis and ore potential of the Kapalagulu and Musongati layered intrusions. *Lithos* **2008**, *101*, 24–53. [CrossRef]
79. De Clercq, F.; Muchez, P.; Dewaele, S.; Fernandez-Alonso, M.; Boyce, A.A.; Piessens, K. The evolution of W vein-type deposits in Rwanda: A fluid inclusion and stable isotope study. *Geol. Belg.* **2008**, *11*, 251–258.
80. De Clercq, S.; Chew, D.; O'Sullivan, G.; De Putter, T.; De Grave, J.; Dewaele, S. Characterisation and geodynamic setting of the 1 Ga granitoids of the Karagwe-Ankole belt (KAB), Rwanda. *Precambrian Res.* **2021**, *356*, 106124. [CrossRef]
81. Hulsbosch, N.; Van Daele, J.; Reinders, N.; Dewaele, S.; Jacques, D.; Muchez, P. Structural control on the emplacement of contemporaneous Sn-Ta-Nb mineralized LCT pegmatites and Sn bearing quartz veins: Insights from the Musha and Ntunga deposits of the Karagwe-Ankole Belt, Rwanda. *J. Afr. Earth Sci.* **2017**, *134*, 24–32. [CrossRef]
82. Muchez, P.; Hulsbosch, N.; Dewaele, S. Geological Mapping and Implications for Nb-Ta, Sn and W Prospection in Rwanda. *Bull. Séanc. Acad. R. Sci. Outre-Mer* **2014**, *60*, 515–530.
83. Cahen, L.; Ledent, D. Précision sur l'âge, la pétrogenèse et la position stratigraphique des granites a étain de l'Est de l'Afrique centrale. *Bull. Soc. Belg. Géologie* **1979**, *88*, 33–49.
84. Cailteux, J.; Binda, P.L.; Katekesha, W.M.; Kampunzu, A.B.; Intiomale, M.M.; Kapenda, D.; Kaunda, C.; Ngongo, K.; Tshiauka, T.a.; Wendorff, M. Lithostratigraphical Correlation of the Neoproterozoic Roan Supergroup from Shaba (Zaire) and Zambia, in the Central African Copper-Cobalt Metallogenic Province. *J. Afr. Earth Sci.* **1994**, *19*, 265–278. [CrossRef]
85. Cailteux, J.L.H.; Kampunzu, A.B.; Lerouge, C.; Kaputo, A.K.; Milesi, J.P. Genesis of sediment-hosted stratiform copper-cobalt deposits, central African Copperbelt. *J. Afr. Earth Sci.* **2005**, *42*, 134–158. [CrossRef]
86. Cailteux, J.L.H.; Muchez, P.; De Cuyper, J.; Dewaele, S.; De Putter, T. Origin of the megabreccias in the Katanga Copperbelt (D.R.Congo). *J. Afr. Earth Sci.* **2018**, *140*, 76–93. [CrossRef]
87. Dewaele, S.; Muchez, P.; Vets, J.; Fernandez-Alonzo, M.; Tack, L. Multiphase origin of the Cu-Co ore deposits in the western part of the Lufilian fold-and-thrust belt, Katanga (Democratic Republic of Congo). *J. Afr. Earth Sci.* **2006**, *46*, 455–469. [CrossRef]
88. Johnson, J.E.; Webb, S.M.; Ma, C.; Fischer, W.W. Manganese mineralogy and diagenesis in the sedimentary rock record. *Geochim. Cosmochim. Acta* **2016**, *173*, 210–231. [CrossRef]
89. Kampunzu, A.B.; Cailteux, J.L.H.; Kamona, A.F.; Intiomale, M.M.; Melcher, F. Sediment-hosted Zn-Pb-Cu deposits in the Central African Copperbelt. *Ore Geol. Rev.* **2009**, *35*, 263–297. [CrossRef]
90. Kampunzu, A.B.; Kanika, M.; Kapenda, D.; Tshimanga, K. Geochemistry and Geotectonic Setting of Late Proterozoic Katangan Basic Rocks from Kibambale in Central Shaba (Zaire). *Geol. Rundsch.* **1993**, *82*, 619–630. [CrossRef]
91. Lerouge, C.; Cailteux, J.; Kampunzu, A.B.; Milesi, J.P.; Flehoc, C. Sulphur isotope constraints on formation conditions of the Luiswishi ore deposit, Democratic Republic of Congo (DRC). *J. Afr. Earth Sci.* **2005**, *42*, 173–182. [CrossRef]
92. Mambwe, P.; Delpomdor, F.; Lavoie, S.; Mukonki, P.; Batumike, J.; Muchez, P. Sedimentary evolution and stratigraphy of the similar to 765-740 Ma Kansuki-Mwashya platform succession in the Tenke-Fungurume Mining District, Democratic Republic of the Congo. *Geol. Belg.* **2020**, *23*, 69–85. [CrossRef]
93. Mambwe, P.; Kipata, L.; Chabu, M.; Muchez, P.; Lubala, T.; Jebrak, M.; Delvaux, D. Sedimentology of the Shangoluwe breccias and timing of the Cu mineralisation (Katanga Supergroup, D.R. of Congo). *J. Afr. Earth Sci.* **2017**, *132*, 1–15. [CrossRef]
94. Mambwe, P.; Milan, L.; Batumike, J.; Lavoie, S.; Jebrak, M.; Kipata, L.; Chabu, M.; Mulongo, S.; Lubala, T.; Delvaux, D.; et al. Lithology, petrography and Cu occurrence of the Neoproterozoic glacial Mwale Formation at the Shanika syncline (Tenke Fungurume, Congo Copperbelt; Democratic Republic of Congo). *J. Afr. Earth Sci.* **2017**, *129*, 898–909. [CrossRef]
95. Hulsbosch, N.; Hertogen, J.; Dewaele, S.; Andre, L.; Muchez, P. Petrographic and mineralogical characterisation of fractionated pegmatites culminating in the Nb-Ta-Sn pegmatites of the Gatumba area (western Rwanda). *Geol. Belg.* **2013**, *16*, 105–117.
96. Büttner, S.H.; Reid, W.; Glodny, J.; Wiedenbeck, M.; Chuwa, G.; Moloto, T.; Gucsik, A. Fluid sources in the Twangiza–Namoya Gold Belt (Democratic Republic of Congo): Evidence from tourmaline and fluid compositions, and from boron and Rb–Sr isotope systematics. *Precambrian Res.* **2016**, *280*, 161–178. [CrossRef]
97. Hulsbosch, N.; Boiron, M.C.; Dewaele, S.; Muchez, P. Fluid fractionation of tungsten during granite-pegmatite differentiation and the metal source of peribatholitic W quartz veins: Evidence from the Karagwe-Ankole Belt (Rwanda). *Geochim. Cosmochim. Acta* **2016**, *175*, 299–318. [CrossRef]
98. Linnen, R.L.; Keppler, H. Columbite solubility in granitic melts: Consequences for the enrichment and fractionation of Nb and Ta in the Earth's crust. *Contrib. Miner. Petrol.* **1997**, *128*, 213–227. [CrossRef]

99. Linnen, R.L.; Keppler, H. Melt composition control of Zr/Hf fractionation in magmatic processes. *Geochim. Cosmochim. Acta* **2002**, *66*, 3293–3301. [CrossRef]
100. Gagnon, J.E.; Samson, I.M.; Fryer, B.J.; Williams-Jones, A.E. The Composition and Origin of Hydrothermal Fluids in a Nyf-Type Granitic Pegmatite, South Platte District, Colorado: Evidence from La Icp Ms Analysis of Fluorite-and Quartz-Hosted Fluid Inclusions. *Can. Mineral.* **2004**, *42*, 1331–1355. [CrossRef]
101. Hatert, F.; Lefèvre, P.; Fransolet, A.-M.; Spirlet, M.-R.; Rebbouh, L.; Fontan, F.; Keller, P. Ferrorosemaryite, $NaFe_2+Fe_3+Al(PO_4)_3$, a new phosphate mineral from the Rubindi pegmatite, Rwanda. *Eur. J. Mineral.* **2005**, *17*, 749–759. [CrossRef]
102. Goldmann, S. Mineralogical-Geochemical Characterisation of Cassiterite and Wolframite Ores for an Analytical Fingerprint: Focus on Trace Element Analysis by LA-ICP-MS. Ph.D. Thesis, Faculty of Natural Sciences, Leibniz University Hannover, Hannover, Germany, 2016; pp. 1–288.
103. Goldmann, S.; Melcher, F.; Gabler, H.E.; Dewaele, S.; De Clercq, F.; Muchez, P. Mineralogy and Trace Element Chemistry of Ferberite/Reinite from Tungsten Deposits in Central Rwanda. *Minerals* **2013**, *3*, 121–144. [CrossRef]
104. Roedder, E. Fluid inclusions. *Rev. Mineral.* **1984**, *12*, 646.
105. Chou, I.M.; Wang, A. Application of laser Raman micro-analyses to Earth and planetary materials. *J. Asian Earth Sci.* **2017**, *145*, 309–333. [CrossRef]
106. Chi, G.; Diamond, L.W.; Lu, H.; Lai, J.; Chu, H. Common Problems and Pitfalls in Fluid Inclusion Study: A Review and Discussion. *Minerals* **2020**, *11*, 7. [CrossRef]
107. Randive, K.R.; Hari, K.R.; Dora, M.L.; Malpe, D.B.; Bhondwe, A.A. Study of Fluid Inclusions: Methods, Techniques and Applications. *Gondwana Geol. Mag.* **2014**, *29*, 19–28.
108. Bodnar, R.J.; Vityk, M.O. Interpretation of microthermometric data for $H_2O$-NaCl fluid inclusions. In *Fluid Inclusions in Minerals: Methods and Application*; De Vivo, B., Frezzotti, M.L., Eds.; Short Course IMA: Pontignano-Siena, Italy, 1994; pp. 117–130.
109. Driesner, T.; Heinrich, C.A. The system $H_2O$–NaCl. Part I: Correlation formulae for phase relations in temperature–pressure–composition space from 0 to 1000 °C, 0 to 5000 bar, and 0 to 1 XNaCl. *Geochim. Cosmochim. Acta* **2007**, *71*, 4880–4901. [CrossRef]
110. Lecumberri-Sanchez, P.; Luo, M.C.; Steele-MacInnis, M.; Runyon, S.E.; Sublett, D.M.; Klyukin, Y.I.; Bodnar, R.J. Synthetic fluid inclusions XXII: Properties of $H_2O$-NaCl ± KCl fluid inclusions trapped under vapor- and salt-saturated conditions with emphasis on the effect of KCl on phase equilibria. *Geochim. Cosmochim. Acta* **2020**, *272*, 78–92. [CrossRef]
111. Lecumberri-Sanchez, P.; Steele-MacInnis, M.; Bodnar, R.J. A numerical model to estimate trapping conditions of fluid inclusions that homogenize by halite disappearance. *Geochim. Cosmochim. Acta* **2012**, *92*, 14–22. [CrossRef]
112. Murciego, A.; Sanchez, A.G.; Dusausoy, Y.; Pozas, J.M.M.; Ruck, R. Geochemistry and EPR of cassiterites from the Iberian Hercynian Massif. *Miner. Mag.* **1997**, *61*, 357–365. [CrossRef]
113. Giuliani, G. La Cassitérite Zonée du Gisement De Sokhret Allal (Granite des Zaer; Maroc Central): Composition chimique et phases fluides associées. *Miner. Depos.* **1987**, *22*, 253–261. [CrossRef]
114. Guo, C.; Chen, Y.; Zeng, Z.; Lou, F. Petrogenesis of the Xihuashan granites in southeastern China: Constraints from geochemistry and in-situ analyses of zircon UPbHfO isotopes. *Lithos* **2012**, *148*, 209–227. [CrossRef]
115. Haskin, L.A.; Wang, A.; Rockow, K.M.; Jolliff, B.L.; Korotev, R.L.a.; Viskupic, K.M. Raman spectroscopy for mineral identification and quantification for in situ planetary surface analysis: A point count method. *J. Geophys. Res.* **1997**, *102*, 19293–19306. [CrossRef]
116. Izoret, L.; Marnier, G.a.; Dusausoy, Y. Caratérisation cristallochimique de la cassitérite des gisements d'étain et de tungsten de Galice, Espagne. *Can. Miner.* **1985**, *23*, 221–231.
117. Möller, P.; Černý, P.; Saupé, F. *Lanthanides, Tantalum, and Niobium: Mineralogy, Geochemistry, Characteristics of Primary ore Deposits, Prospecting, Processing, and Applications: Proceedings of a Workshop in Berlin, November 1986*; Springer: Berlin, Germany; New York, NY, USA, 1989.
118. Remond, G. Exemples d'identification et de localisation des éléments en traces dans des minéraux luminescents (cassitérites) à l'aide de l'analyseur ionique. *Bull. Société Française Minéralogie Cristallogr.* **1973**, *96*, 183–198. [CrossRef]
119. Remond, G.; Cesbron, F.; Chapoulie, R.; Ohnenstetter, D.; Roques-Carmes, C.; Schvoerer, M. Cathodoluminescence Applied to the Microcharacterization of Mineral Materials: A Present Status in Experimentation and Interpretation. *Scanning Microsc.* **1992**, *6*, 23–68.
120. Li, Y.; Liu, Z.; Shao, Y.; Chen, K.; Zhang, J.; Zhang, Y.; Zhang, T. Genesis of the Huanggangliang Fe-Sn polymetallic deposit in the southern Da Hinggan Range, NE China: Constraints from geochronology and cassiterite trace element geochemistry. *Ore Geol. Rev.* **2022**, *151*, 105226. [CrossRef]
121. Chen, Y.-K.; Ni, P.; Pan, J.-Y.; Cui, J.-M.; Li, W.-S.; Fang, G.-J.; Zhao, Z.-H.; Xu, Y.-M.; Ding, J.-Y.; Han, L. Fluid evolution and metallogenic mechanism of the Xianghualing skarn-type Sn deposit, South China: Evidence from petrography, fluid inclusions and trace-element composition of cassiterite. *Ore Geol. Rev.* **2023**, *154*, 105351. [CrossRef]
122. Audetat, A.; Zhang, D.H. Abundances of S, Ga, Ge, Cd, In, Tl and 32 other major to trace elements in high-temperature (350–700 degrees C) magmatic-hydrothermal fluids. *Ore Geol. Rev.* **2019**, *109*, 630–642. [CrossRef]
123. Raith, J.G.; Melcher, F.; Lichtervelde, M.V. Rare-element pegmatites; from natural systems to the experimental lab. *Mitt. Österr. Miner. Ges.* **2014**, *160*, 11–57.
124. Bellot, N.; Boyet, M.; Doucelance, R.; Bonnand, P.; Savov, I.P.; Plank, T.A.; Elliott, T. Origin of negative cerium anomalies in subduction-related volcanic samples: Constraints from Ce and Nd isotopes. *Chem. Geol.* **2018**, *500*, 46–63. [CrossRef]

125. Braun, J.J.; Pagel, M.; Muller, J.P.; Bilong, P.; Michard, A.A.; Guillet, B. Cerium anomalies in lateritic profiles. *Geochim. Cosmochim. Acta* **1990**, *54*, 771–795. [CrossRef]
126. Dai, S.; Graham, I.T.; Ward, C.R. A review of anomalous rare earth elements and yttrium in coal. *Int. J. Coal Geol.* **2016**, *159*, 82–95. [CrossRef]
127. De Baar, H.; Faure, G. On cerium anomalies in the Sargasso Sea. *Geochim. Cosmochim. Acta* **1991**, *55*, 2981–2983. [CrossRef]
128. Kölling, M. Comparison of different methods for redox potential determination in natural waters. In *Redox*; Springer: Berlin/Heidelberg, Germany, 2000; pp. 42–54.
129. Kraemer, D.; Tepe, N.; Pourret, O.; Bau, M. Negative cerium anomalies in manganese (hydr)oxide precipitates due to cerium oxidation in the presence of dissolved siderophores. *Geochim. Cosmochim. Acta* **2017**, *196*, 197–208. [CrossRef]
130. Möller, P.; Muecke, G.K. Significance of Europium anomalies in silicate melts and crystal-melt equilibria: A re-evaluation. *Contrib. Miner. Petr.* **1984**, *87*, 242–250. [CrossRef]
131. Tostevin, R.; Shields, G.A.; Tarbuck, G.M.; He, T.; Clarkson, M.O.; Wood, R.A. Effective use of cerium anomalies as a redox proxy in carbonate-dominated marine settings. *Chem. Geol.* **2016**, *438*, 146–162. [CrossRef]
132. Carocci, E.; Truche, L.; Cathelineau, M.; Caumon, M.-C.; Bazarkina, E.F. Tungsten (VI) speciation in hydrothermal solutions up to 400°C as revealed by in-situ Raman spectroscopy. *Geochim. Cosmochim. Acta* **2022**, *317*, 306–324. [CrossRef]
133. Vonopartis, L.; Nex, P.; Kinnaird, J.; Robb, L. Evaluating the Changes from Endogranitic Magmatic to Magmatic-Hydrothermal Mineralization: The Zaaiplaats Tin Granites, Bushveld Igneous Complex, South Africa. *Minerals* **2020**, *10*, 379. [CrossRef]
134. McDonough, W.F.; Sun, S.S. The composition of the Earth. *Chem. Geol.* **1995**, *120*, 223–253. [CrossRef]
135. McLennan, S.M.; Hemming, S.R.; Taylor, S.R.; Ericksson, K.A. Early Proterozoic crustal evolution: Geochemical and Nd-Pb isotopic evidence from metasedimentary rocks, southwestern North America. *Geochim. Cosmochim. Acta* **1995**, *59*, 1153–1177. [CrossRef]
136. Turimumahoro, D.; Hulsbosch, N.; Nahimana, L.; Dewaele, S.; Muchez, P. Geochemical signature of muscovites as pathfinder for fractionation of pegmatites in the Kabarore-Mparamirundi area (northwestern Burundi, Central Africa). *Geol. Belg.* **2020**, *23*, 53–67. [CrossRef]
137. Hulsbosch, N.; Boiron, M.C.; Thomas, R.; Van Daele, J.; Dewaele, S.; Muchez, P. Evaluation of the petrogenetic significance of melt inclusions in pegmatitic schorl-dravite from graphic tourmaline-quartz assemblages: Application of LA-ICP-QMS analyses and volume ratio calculations. *Geochim. Cosmochim. Acta* **2019**, *244*, 308–335. [CrossRef]
138. Hulsbosch, N.; Muchez, P. Tracing fluid saturation during pegmatite differentiation by studying the fluid inclusion evolution and multiphase cassiterite mineralisation of the Gatumba pegmatite dyke system (NW Rwanda). *Lithos* **2020**, *354–355*, 105285. [CrossRef]
139. Audetat, A.; Gunther, D.; Heinrich, C.A. Magmatic-hydrothermal evolution in a fractionating granite: A microchemical study of the Sn-W-F-mineralized Mole Granite (Australia). *Geochim. Cosmochim. Acta* **2000**, *64*, 3373–3393. [CrossRef]
140. Linnen, R.L.; Pichavant, M.; Holtz, F. The combined effects of $fO_2$ and melt composition on $SnO_2$ solubility and tin diffusivity in haplogranitic melts. *Geochim. Cosmochim. Acta* **1996**, *60*, 4965–4976. [CrossRef]
141. Zhang, S.; Zhang, R.; Lu, J.; Ma, D.; Ding, T.; Gao, S.; Zhang, Q. Neoproterozoic tin mineralization in South China: Geology and cassiterite U–Pb age of the Baotan tin deposit in northern Guangxi. *Miner. Depos.* **2019**, *54*, 1125–1142. [CrossRef]
142. Bodnar, R.J.; Lecumberri-Sanchez, P.; Moncada, D.; Steele-MacInnis, M. Fluid Inclusions in Hydrothermal Ore Deposits. In *Treatise on Geochemistry*; Elsevier: Amsterdam, The Netherlands, 2014; pp. 119–142.
143. Elongo, V.; Lecumberri-Sanchez, P.; Legros, H.; Falck, H.; Adlakha, E.; Roy-Garand, A. Paragenetic constraints on the Cantung, Mactung and Lened tungsten skarn deposits, Canada: Implications for grade distribution. *Ore Geol. Rev.* **2020**, *125*, 103677. [CrossRef]
144. Korges, M.; Weis, P.; Lüders, V.; Laurent, O. Depressurization and boiling of a single magmatic fluid as a mechanism for tin-tungsten deposit formation. *Geology* **2018**, *46*, 75–78. [CrossRef]
145. Legros, H.; Lecumberri-Sanchez, P.; Elongo, V.; Laurent, O.; Falck, H.; Adlakha, E.; Chelle-Michou, C. Fluid evolution of the Cantung tungsten skarn, Northwest Territories, Canada: Differentiation and fluid-rock interaction. *Ore Geol. Rev.* **2020**, *127*, 103866. [CrossRef]
146. Legros, H.; Marignac, C.; Tabary, T.; Mercadier, J.; Richard, A.; Cuney, M.; Wang, R.-C.; Charles, N.; Lespinasse, M.-Y. The ore-forming magmatic-hydrothermal system of the Piaotang W-Sn deposit (Jiangxi, China) as seen from Li-mica geochemistry. *Am. Mineral.* **2018**, *103*, 39–54. [CrossRef]
147. Legros, H.; Richard, A.; Tarantola, A.; Kouzmanov, K.; Mercadier, J.; Vennemann, T.; Marignac, C.; Cuney, M.; Wang, R.-C.; Charles, N. Multiple fluids involved in granite-related W-Sn deposits from the world-class Jiangxi province (China). *Chem. Geol.* **2019**, *508*, 92–115. [CrossRef]
148. Scholten, L.; Schmidt, C.; Lecumberri-Sanchez, P.; Newville, M.; Lanzirotti, A.; Sirbescu, M.L.C.; Steele-MacInnis, M. Solubility and speciation of iron in hydrothermal fluids. *Geochim. Cosmochim. Acta* **2019**, *252*, 126–143. [CrossRef]
149. Wade, J.; Wood, B.J.; Norris, C.A. The oxidation state of tungsten in silicate melt at high pressures and temperatures. *Chem. Geol.* **2013**, *335*, 189–193. [CrossRef]
150. Duc-Tin, Q.; Audetat, A.; Keppler, H. Solubility of tin in (Cl, F)-bearing aqueous fluids at 700 degrees C, 140 MPa: A LA-ICP-MS study on synthetic fluid inclusions. *Geochim. Cosmochim. Acta* **2007**, *71*, 3323–3335. [CrossRef]

151. Jiang, H.; Jiang, S.-Y.; Li, W.-Q.; Peng, N.-J.; Zhao, K.-D. Fluid inclusion and isotopic (C, H, O, S and Pb) constraints on the origin of late Mesozoic vein-type W mineralization in northern Guangdong, South China. *Ore Geol. Rev.* **2019**, *112*, 103007. [CrossRef]
152. Lecumberri-Sanchez, P.; Vieira, R.; Heinrich, C.A.; Pinto, F.; Walle, M. Fluid-rock interaction is decisive for the formation of tungsten deposits. *Geology* **2017**, *45*, 579–582. [CrossRef]
153. Bali, E.; Audetat, A.; Keppler, H. Mobility of U and Th in subduction zone fluids—A synthetic fluid inclusion study. *Geochim. Cosmochim. Acta* **2009**, *73*, 54–80.
154. Bali, E.; Audetat, A.A.; Keppler, H. The mobility of U and Th in subduction zone fluids: An indicator of oxygen fugacity and fluid salinity. *Contrib. Miner. Petr.* **2011**, *161*, 597–613. [CrossRef]
155. Heinrich, C.A. From fluid inclusion microanalysis to large-scale hydrothermal mass transfer in the Earth's interior. *J. Mineral. Petrol. Sci.* **2006**, *101*, 110–117. [CrossRef]
156. Heinrich, C.A.; Candela, P.A. Fluids and Ore Formation in the Earth's Crust. In *Treatise on Geochemistry*; Elsevier: Amsterdam, The Netherlands, 2014; pp. 1–28.
157. Li, X.; Wang, G.; Mao, W.; Wang, C.; Xiao, R.; Wang, M. Fluid inclusions, muscovite Ar–Ar age, and fluorite trace elements at the Baiyanghe volcanic Be–U–Mo deposit, Xinjiang, northwest China: Implication for its genesis. *Ore Geol. Rev.* **2015**, *64*, 387–399. [CrossRef]
158. Seward, T.M.; Williams-Jones, A.E.; Migdisov, A.A. The Chemistry of Metal Transport and Deposition by Ore-Forming Hydrothermal Fluids. In *Treatise on Geochemistry*; Elsevier: Amsterdam, The Netherlands, 2014; Volume 2, pp. 29–57.
159. Steele-MacInnis, M.; Manning, C.E. Hydrothermal Properties of Geologic Fluids. *Elements* **2020**, *16*, 375–380. [CrossRef]
160. Gherardi, F.; Droghieri, E.; Magro, G. Hydrothermal Processes at Aluto-Langano (Ethiopia): Insights from the Stable Carbon Isotope Composition of Fluid Inclusions. *GRC Trans.* **2014**, *38*, 439–444.
161. Green, D. The role of oxidation-reduction and CHO fluids in determining melting conditions and magma compositions in the upper mantle. *Proc. Indian Acad. Sci. Earth Planet. Sci.* **1990**, *99*, 153–165. [CrossRef]
162. Mark, M.F.; Maier, W.F. $CO_2$-reforming of methane on supported Rh and Ir catalysts. *J. Catal.* **1996**, *164*, 122–130. [CrossRef]
163. Steele-MacInnis, M.; Lecumberri-Sanchez, P.; Bodnar, R.J. Hokieflincs_$H_2O$-NaCl: A Microsoft Excel spreadsheet for interpreting microthermometric data from fluid inclusions based on the PVTX properties of $H_2O$-NaCl. *Comput. Geosci. UK* **2012**, *49*, 334–337. [CrossRef]
164. Zhong, S.; Seltmann, R.; Qu, H.; Song, Y. Characterization of the Zircon Ce anomaly for estimation of oxidation state of magmas: A revised Ce/Ce* method. *Miner. Petrol.* **2019**, *113*, 755–763. [CrossRef]